Developing a model for studying the role of Amyloid-beta in Nothobranchius furzeri (Actinopteri; Cypriniformes) neurodegeneration

Mihaljević, Mihaela

University of Zagreb
Faculty of Science
Department of Biology

Mihaela Mihaljević

Developing a model for studying the role of Amyloid-beta in *Nothobranchius furzeri* (Actinopteri; Cyprinodontiformes) neurodegeneration

Master thesis

Zagreb, 2022.

This master thesis was created in the Max Planck Institute for Biology of Ageing in Cologne (Germany) under the supervision of Professor Dario Riccardo Valenzano and co-supervision of Professor Petra Korać. The thesis was submitted for evaluation to the Department of Biology at the Faculty of Science, University of Zagreb to acquire the academic title of the Master of Molecular Biology.

First and foremost, I would like to thank Prof. Dario Riccardo Valenzano for the opportunity to do an internship and my master thesis work in his group. I am thankful for his great kindness as well as extensive support throughout my whole internship. I will forever remain grateful for everything you have done for me. I would also like to thank my mentor Dr. Dennis de Bakker, who selflessly helped me in many ways, taught me to be focused and meticulous, cheered me up and encouraged me when I needed it the most and always gave me enough space and freedom to do things at my own pace. Thank you for helping me realise who I am as a scientist and teaching me that science is like a marathon, not a sprint. I would also like to thank Dr. David Willemsen, with whom I worked on my other project and who was always attentive and ready to help, even when it had nothing to do with his project. I am also thankful to Assoc. Prof. Petra Korać for her kind support, advice and assistance with my thesis, as well as other courses where she always strived for the best. Thank you for everything.

I would also like to thank all other Valenzano lab members, especially Gabriele and Rozalina for being my first and best friends in Cologne. I want to thank Gabriele for showing me around the lab and sharing his wisdom with me. I want to also thank Rozalina for numerous chats, laughs and strolls around the city which made my life in Cologne so much brighter. I would like to thank Sam for many conversations that we had, both about science and life, Hilal for very nice summer adventures, Jens and Ola for always being kind, helpful, and reaching out to check in on me even when they were not around. I would like to thank the animal care takers Christina and Mattias, because they were always very accommodating and took great care of my fish. To everyone else from the group, Daniel, Emmanuel, Erik, Kathrin, Lisa, Martin, Melike, Miriam, Nicole, Peter, Quinn, Sara, and Silvia, I have to thank you as well, because you made my stay in the Valenzano group special. I would to thank many people from the MPI, but this section is unfortunately too short to thank everyone. However, I want to thank the whole FACS & Imaging Core Facility, especially Christian, Alexandra and Marcel for your extensive help with the cryosectioning and imaging. Moreover, I must thank Prof. Adam Antebi for the opportunity to continue my work as a guest in his group when my group moved to another institute. Big thanks to the rest of the Antebi group, not to name you all, for accepting me into the group, inviting me to your social events and helping me with any scientific obstacle I encountered. I would also like to thank Andrea Veith and Michael Heinrichs for finding a solution to a problem of my prolonged stay in Cologne. Moreover, thanks to everyone else, all other research groups, IT, HR, administration team and scientific coordinators, for your kindness and help during my master thesis.

Finally, enormous thanks to my family and friends – for your selfless love and joy you have brought to my life. Thanks to my "vile", Barbara, Marija and Una, for numerous hours spent chatting and laughing. Thank you for sharing your opinions and thoughts, for being both my uni colleagues and dear friends and for encouraging me to say what I think. Thanks to Višnja, Fran, Irena, and everyone else from my university who helped me in any way they could. Huge thanks to Jelena for being my dearest friend and my travel buddy, for her consolidation, cheerfulness, shared opinions and being an amazing human being. Moreover, thanks to my PMF girls Vanja and Laura Ana, for sharing so much with me and being one of my dearest friends. Thanks to my sister Ivana, for being who you are, visiting me in Cologne and giving me your undivided support and attention. Thanks to Ana, who selflessly shared her laptop with me so I could do the analysis for this thesis, for being one of my oldest friends. Dora, Dujla and Domagoj, thank you so much for constantly putting effort into our friendships, for making me laugh and for loving me throughout the years. I would like to thank my whole high school group of "Idemo dalje" – you have been in my life for 10 years now. Thank you for making those awkward teenage years enjoyable, giving me freedom to be who I was back then, but also loving me for who I have become. Thanks to Kristina and Matea for everything we went through.

Thanks to my love, the most loving, caring, and supportive person I have ever met – Lukas. You have walked by my side throughout the whole thesis, you heard a story about it countless of times, you consoled me when my fish died and my samples almost got lost, you celebrated my every success like it was yours and you proofread it, even though biology is not your thing. I am beyond grateful and thrilled to share my life with you. Looking forward to our next chapter together.

I would like to dedicate this thesis to the most important person in my life – my mother. Thank you for your unlimited love and support, for remembering every little detail about me since I was born, for caring about me, my needs, and my general wellbeing as well as my schoolwork, which brought me to where I am today. Thank you for giving me the freedom to be who I was meant to be.

BASIC DOCUMENTATION CARD

University of Zagreb
Faculty of Science
Department of Biology

Master thesis

Developing a model for studying the role of Amyloid-beta in *Nothobranchius furzeri* (Actinopteri; Cyprinodontiformes) neurodegeneration

Mihaela Mihaljević

Rooseveltov trg 6, 10000 Zagreb, Croatia

The Alzheimer's disease (AD) is the most prevalent form of dementia, majorly affecting elderly population. Despite extensive research related to the AD, the lack of knowledge about exact causes imposes an obstacle in the development of effective treatments of the disease. One of the main hallmarks of AD is the accumulation of amyloid-β peptides in the brain, but the mechanism underlying it is unknown. The African turquoise killifish (*Nothobranchius furzeri*) has been used to study several hallmarks of neurodegeneration, such as general cognitive decline, neuronal degeneration, neuroinflammation, ongoing oxidative stress and accumulation of α-synuclein in the brain. This study aimed to investigate accumulation of amyloid-β in the aging turquoise killifish brain, as well as detect differences in age-dependent brain degeneration between turquoise killifish and zebrafish (*Danio rerio*). Fluorescent immunohistochemistry was utilized on the cross-sections of brain tissue. The results show that turquoise killifish displays age-dependent accumulation of amyloid-β in the brain. Moreover, turquoise killifish undergoes brain atrophy, astrogliosis and loss of neuronal density, while zebrafish shows lower extent of age-related brain pathologies. This study aimed to create CRISPR/Cas9-mediated mutants of *amyloid-β precursor protein* for further studying of AD. The research resulted in a successful mutation of one out of two paralogue genes in the turquoise killifish.

Keywords: APP, astrogliosis, neuronal loss, CRISPR/Cas9 mutants
(74 pages, 16 figures, 7 tables, 155 references, original in: English)
Thesis is deposited in Central Biological Library.

Mentor: Prof. Dario Riccardo Valenzano
Co-mentor: Assoc. Prof. Petra Korać

Reviewers:
Assoc. Prof. Petra Korać
Prof. Biljana Balen
Assoc. Prof. Inga Urlić
Thesis accepted: 8.9.2022

TEMELJNA DOKUMENTACIJSKA KARTICA

Sveučilište u Zagrebu

Prirodoslovno-matematički fakultet

Biološki odsjek Diplomski rad

Razvoj modela za analizu uloge proteina amiloid-beta u procesu neurodegeneracije u vrste *Nothobranchius furzeri* (Actinopteri; Cyprinodontiformes)

Mihaela Mihaljević

Rooseveltov trg 6, 10000 Zagreb, Hrvatska

Alzheimerova bolest najzastupljeniji je oblik demencije koji većinom pogađa stariju populaciju. Unatoč opsežnim istraživanjima same bolesti, točni uzroci nastanka i dalje su nepoznati, što dodatno otežava razvoj učinkovitih terapija. Jedno od glavnih obilježnja Alzheimerove bolesti je nakupljanje peptida amiloid-β u mozgu, no mehanizam nastanka nije poznat. U zadnje vrijeme, riba vrste *Nothobranchius furzeri* uvelike se koristi za istraživanje nekoliko obilježja procesa neurodegeneracije mozga, poput smanjenja kognitivnih sposobnosti, degeneracije neurona, upalnih procesa u mozgu, oksidativnog stresa te nakupljanja proteina α-sinuklein u tkivu mozga. Cilj ovog istraživanja bio je istražiti nakupljanje peptida amiloid-β u procesu starenja mozga *N. furzeri*, kao i uočiti razlike između mozga *N. furzeri* i zebrice (*Danio rerio*). Za istraživanje je korištena fluorescentna imunohistokemija na presjecima moždanog tkiva. Rezultati pokazuju da u mozgu *N. furzeri* dolazi do nakupljanja peptida amiloid-β tijekom starenja. Također, mozak *N. furzeri* atrofira, prolazi kroz proces astroglioze te pokazuje smanjenu gustoću neurona, dok zebrica tijekom starenja pokazuje blažu patologiju mozga. Nadalje, cilj istraživanja bio je pomoću platforme CRISPR/Cas9 mutirati gen za prekursor proteina amiloid-β, koji će poslužiti za daljnje istraživanje Alzheimerove bolesti. Istraživanje je rezultiralo utišavanjem jednog od dva paraloga ovog gena u *N. furzeri*.

Ključne riječi: APP, astroglioza, gubitak neurona, mutant CRISPR/Cas9
(74 stranica, 16 slika, 7 tablica, 155 literaturnih navoda, jezik izvornika: engleski)
Rad je pohranjen u Središnjoj biološkoj knjižnici

Mentor: Prof. dr. sc. Dario Riccardo Valenzano
Komentor: Izv. prof. dr. sc. Petra Korać

Ocjenitelji:
izv. prof. dr. sc. Petra Korać
prof. dr. sc. Biljana Balen
izv. prof. dr. sc. Inga Urlić
Rad prihvaćen: 8.9.2022

LIST OF ABBREVIATIONS

AD – Alzheimer's Disease

Aβ – Amyloid-beta Peptide

APLP1 – Amyloid-like Protein 1

APLP2 – Amyloid-like Protein 2

APP – Amyloid-beta Precursor Protein

hAPP – Human APP

AR – Anterior Rhomboencephalon

BACE1 – β-Secretase

BBB – Blood Brain Barrier

CB – Cerebellum

CRISPR/Cas9 – Clustered Regularly Interspaced Short Palindromic Repeats and CRISPR-associated protein 9

HIL – Hypothalamus Inferior Lobe

HSL – Hypothalamus Superior Lobe

IHC - Immunohistochemistry

NFT – Neurofibrillary Tangle

OT – Optic Tectum

PD – Parkinson's disease

PR – Posterior Rhomboencephalon

pTau – Phosphorylated Tau

TC - Telencephalon

Table of contents

1. INTRODUCTION

1.1. Neurodegeneration in humans

Aging is defined as a functional loss of fitness over time which leads to disease and death in most organisms later in life (Rose, 2009; López-Otín *et al.*, 2013). Main cellular and molecular hallmarks linked to aging include depletion of stem cells, changes in intracellular communication and nutrient-sensing, genomic instability, telomere attrition, epigenetic changes, loss of proteostasis, dysfunctional mitochondria and cellular senescence (López-Otín *et al.*, 2013). Neurodegenerative diseases take place as one of the most common diseases among older people, with hallmarks of aging linked to their pathology (Hou *et al.*, 2019; Azam *et al.*, 2021). Neurodegenerative diseases display changes in neuronal structure and function, leading to impaired movement or cognitive decline (*Hallmarks of Neurodegeneration*, 2022).

Worldwide, more than 55 million people suffer from dementia, with around 10 million new patients being diagnosed every year. Currently, dementia holds the 7th place among leading causes of death and causes a severe decrease in quality of life in patients that have to live with the disease (*Dementia*, 2021). Counting in estimated life expectancy, impact of disease and mortality rates, it is predicted that the number of dementia cases in the UK alone will increase by as much as 57% by 2040, with more than 1.2 million patients (Ahmadi-Abhari *et al.*, 2017). In the US, predictions state that by 2060, the number of dementia cases will rise from 6.08 million in 2017 to 15 million in 2060 (Brookmeyer *et al.*, 2018).

Studies performed on cognitively normal aging individuals observed some form of neurodegenerative pathology in the majority of participants, despite them being cognitively fit for their age (Davis *et al.*, 1999; Bennett *et al.*, 2012). For example, brain tissue isolated from cognitively normal individuals above 50 years of age shows elevated levels of aggregating proteins, such as amyloid-β, hyperphosphorylated tau and α-synuclein (Elobeid *et al.*, 2016). Formation of protein aggregates poses a risk of certain neurodegenerative diseases, such as amyloid-β (Aβ) and hyperphosphorylated tau in Alzheimer's disease (AD) and α-synuclein in Parkinson's disease (PD) (Nussbaum and Ellis, 2003). Even though it is challenging to estimate how many people suffer from AD, it is considered that 60-70% of all dementia patients can be associated with AD. (*Dementia*, 2021). Patients suffering from AD experience difficulties with learning and memory, disorientation, and changes in behaviour and mood, leading to an inability to perform everyday tasks (*Alzheimer's disease - Symptoms and causes*, 2022). Due to the symptoms of AD, patients are an enormous burden to their families and caretakers, as well as society in general. Since there has been an increase in life expectancy of populations across the world, prevention or delay of the onset of AD symptoms is crucial, yet still not accessible (Rasmussen and Langerman, 2019).

1.2. Clinical diagnosis of Alzheimer's disease

Alzheimer's disease (AD) is the most prevalent neurodegenerative disease, with around 50 million AD patients worldwide (*Alzheimer's disease - Symptoms and causes*, 2022). AD can be divided into familial AD (FAD) with early onset of symptoms and sporadic AD with late onset of symptoms.

The early onset of AD has been linked to different mutations in the genes coding for Amyloid-β precursor protein (APP), Presenilin 1 (PSEN1) and Presenilin 2 (PSEN2). 1-5 % of all AD patients carry autosomal dominant mutations in one of the genes coding for these three proteins (Azam *et al.*, 2021). APP belongs to a group of large type-1 integral membrane glycoproteins important for cell signalling and adhesion, axonal transport, homeostasis of neurons, normal development and functioning of synapses as well as learning and memory (Duce *et al.*, 2010; Deyts, *et al.*, 2016; Chen *et al.*, 2017). PSEN1 and PSEN2 are important subunits of an enzyme complex called γ-secretase, which cuts multiple substrates, including APP, consequently increasing levels of Aβ in the brain (Loy *et al.*, 2014; Ledo *et al.*, 2021; Xiao *et al.*, 2021).

The late onset of AD seems to be linked to a myriad of different factors, such as accumulation of proteins, cholinergic or mitochondrial dysfunction, DNA damage, and inflammation (Hou *et al.*, 2019). Moreover, mutations in gene coding for apolipoprotein E (APOE*ε4), that is mainly expressed by the astrocytes in the brain, have been recognised to play an important role in the late onset of AD (Liu *et al.*, 2013).

1.3. Amyloid-β precursor protein and Amyloid-β peptide

APP contains a long extracellular N-terminus carrying many glycosylated modifications, a short intracellular C-terminus and a transmembrane domain (Chen *et al.*, 2017). The long extracellular part of the protein consists of sequences E1, E2 and Kunitz protease inhibitor (KPI) domain. The KPI domain inhibits serine proteases (mainly trypsin), and takes part in forming protein-protein interactions between APP isoforms containing KPI, as well as with other proteins (Hall and Roberson, 2012). Expression and alternative splicing of exons 7 and 8 in *App* produces three different molecules of APP consisting of 695, 751 or 770 amino acids (called isoforms APP695, APP751, APP770). The isoform APP695, which is the only form of APP lacking the KPI domain, is the most common form of APP found almost exclusively in neuronal cells. The isoforms APP751 and APP770 are expressed by platelets in blood vessels and other peripheral cells (Chen *et al.*, 2017). APP belongs to a multi-gene super-family, together with Amyloid-like protein 1 (APLP1) and Amyloid-like protein 2 (APLP2). APLP1 and APLP2 share primary amino acid sequences, structures and several domains with the APP, but lack the Aβ sequence as well as the extension domain at the end of the extracellular E1 domain (Deyts *et al.*, 2016).

APP in humans can undergo two different pathways, called the nonamyloidogenic and amyloidogenic pathways. The nonamyloidogenic pathway is likely to be activated by electrical impulses coming from

active acetylcholine receptors on neuronal cells. The nonamyloidogenic pathways involves enzyme α-secretase, which cuts APP, resulting in an extracellular sAPPα and 83-amino-acid-long fragment hanging on the C-terminus. The enzyme γ-secretase then cleaves the remaining APP fragment, releasing a 3 kDA P3 peptide (Sun *et al.*, 2015).

In the amyloidogenic pathway, APP undergoes several cleavage reactions by enzymes β- and γ-secretases at the N-terminus and C-terminus, respectively (Figure 1). First, β-secretase cuts the C-terminus of APP, resulting in a 99-amino-acid-long fragment. Furthermore, γ-secretase cuts the fragment at different cutting sites, resulting in 36-53 amino acids long Aβ peptide. These pre-Aβ peptides are further processed until 40-amino-acid-long $A\beta_{40}$ or 42-amino-acid-long $A\beta_{42}$ is reached. The peptide left in the cell is called APP intracellular domain (AICD), which can act as a regulator of gene expression in the nucleus, possibly inducing apoptosis. Amyloid-β peptides (both $A\beta_{40}$ and $A\beta_{42}$) are considered to be extremely important for the AD-pathology (Chen *et al.*, 2017; Ledo *et al.*, 2021).

Additionally, $A\beta_{40}$ and $A\beta_{42}$ peptides can be post-translationally modified. Common modifications include the truncation of the N-terminus of Aβ, the addition of pyroglutamate modification at the 3rd or 11th amino acid residue on the truncated N-terminus ($A\beta_{pE3}$, $A\beta_{pE11}$) and the phosphorylation of serine as 8th or 26th amino acid residue (pSer8Aβ, pSer26Aβ) (Thal *et al.*, 2015). The modified forms of Aβ sometimes co-localise with tau proteins inside neurons, contributing to the disruption of synapse function and overall progression of neurodegeneration (Takahashi *et al.*, 2010). Modified forms of Aβ carrying pyroglutamate or phosphorylated serine are widely present in human AD as well as brains of APP transgenic mice (Thal *et al.*, 2015), but not in normal aging brains (Dong *et al.*, 2012). In the first case, primarily exopeptidases or alternatively endopeptidases cut N-terminus, leaving the 3rd or 11th glutamate in the sequence available for the enzyme glutaminyl cyclase to add a lactam ring, resulting in pyroglutamate at the N-terminus (Thal *et al.*, 2015). Due to the increase in the hydrophobicity, $A\beta_{pE3}$ more efficiently forms oligomers and fibrils compared to the non-modified Aβ (Schlenzig *et al.*, 2009). Moreover, Aβ peptides carrying pyroglutamate proved to be more resistant against proteolytic degradation (via amino- or endopeptidase) and other mechanisms of protein clearance in the brain (Thal *et al.*, 2015).

Extracellular monomers of Aβ can aggregate and form several different oligomers, protofibrils and amyloid fibrils (Figure 1). Aβ oligomers can vary in size (from dimers to dodecamers), remain soluble and transported across the brain. Extracellular soluble Aβ interacts with receptors on the cell membrane, which activates cascades of caspases and the production of reactive oxygen species (ROS), as well as the hyperphosphorylation of tau protein (Chen *et al.*, 2017). Oligomeric forms of Aβ increase permeability of the cell membrane, thereby increasing the levels of calcium and mitochondrial permeability, causing excitotoxicity, and resulting in neuronal death and synapse degeneration. Protein depositions also induce oxidative stress, unfolded protein response and synaptic loss (Fricker *et al.*, 2018). Interestingly, synaptic loss imposes as more risky to lead to cognitive decline associated with

AD, compared to neuronal loss (Fricker *et al.*, 2018). In response to inflammation in the brain, neurons undergo apoptosis and die, leading to the onset of AD (Chen *et al.*, 2017).

Intracellular Aβ was first reported inside of normal brains as well as brains displaying AD-like pathology (Grundke-Iqbal *et al.*, 1989). However, the same study observed intracellular Aβ in the neurons containing neurofibrillary tangles (NFTs), suggesting that these two hallmarks could be linked. The majority of intraneuronal Aβ is a 42-amino-acid long residue (Gouras *et al.*, 2000), localised in multivesicular bodies and linked to synaptic impairment (Takahashi *et al.*, 2002). Intraneuronal Aβ is presumed to facilitate hyperphosphorylation of tau, impairments in normal functioning of synapses, proteasome and mitochondria as well as increase in calcium influx and production of ROS (LaFerla *et al.*, 2007).

In summary, the homeostasis of Aβ in the brain, as well as the production of different Aβ forms, are determined by APP cleavage into Aβ, Aβ oligomerization, Aβ aggregation, proteolytic degradation as well as clearance of both fibrillar and soluble Aβ forms from the brain by other cells (for example astrocytes, Figure 1) (Tanzi *et al.*, 2004).

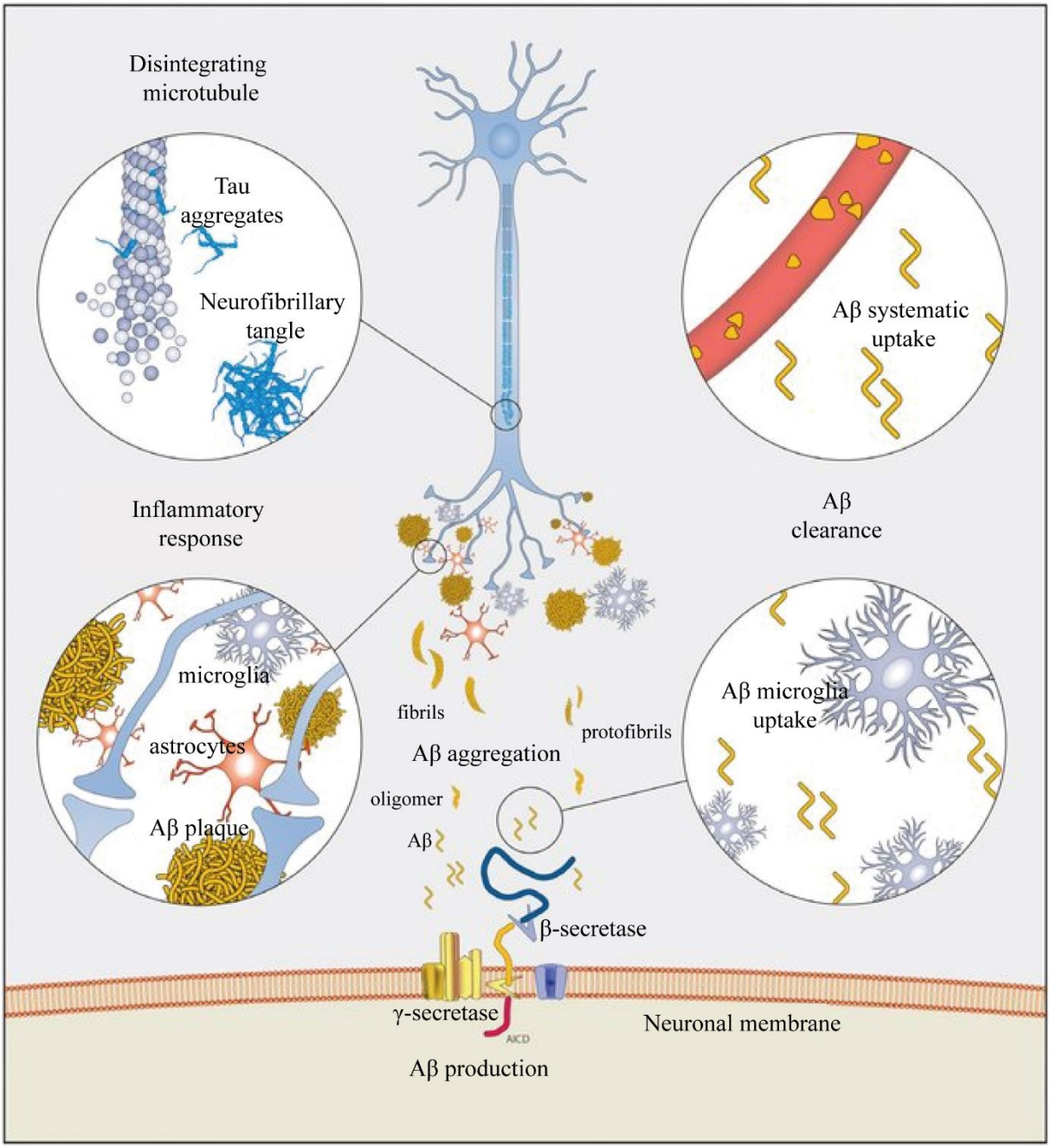

Figure 1. Schematic representation of Aβ cascade in Alzheimer's disease. The production of Aβ peptide is part of the amyloidogenic pathway of APP in humans. APP undergoes cleavage reactions by enzymes β- and γ-secretases at the N-terminus and C-terminus, respectively. The homeostasis of Aβ in the brain is determined by APP cleavage into Aβ, Aβ oligomerization, Aβ aggregation, proteolytic degradation as well as clearance of both fibrillar and soluble Aβ forms from the brain by other cells (for example astrocytes or microglia). Another hallmark of Alzheimer's disease is aggregation of phosphorylated tau in a form of intracellular neurofibrillary tangle (NFT). Source: Panza *et al.* (2019).

AD-like pathology in humans develops in 5 phases, following a certain pattern. Amyloid plaques first form in the neocortex and their formation represents Phase 1. Phase 2 involves the expansion of amyloids into the allocortex (e.g., hippocampus, cingulate gyrus, and entorhinal cortex). Phase 3 is characterised by the expansion of amyloid plaques to the basal forebrain, thalamus, hypothalamus and striatum. In Phase 4 expansion continues to the medulla oblongata and midbrain, and in Phase 5 to the pons and cerebellum (Thal *et al.*, 2002). Phases 1, 2, and 3 are present in both AD and early AD patients, while Phases 4 and 5 are characteristic for AD patients (Thal *et al.*, 2015). Transition from early AD to AD is linked to changes in the structure of Aβ plaques, as well as their further expansion in the brain. $A\beta_{40}$ is the first form of Aβ that forms aggregates inside of the human brain. Accumulation of $A\beta_{42}$ is the next step in progression of AD pathology. In the more advanced stages of AD, modified forms $A\beta_{pE3}$ and $A\beta_{pE11}$ can be detected in plaques of both early AD and AD patients. Phosphorylated serines are almost exclusively linked to patients that show symptoms of AD. Therefore, Aβ undergo sequential processing from a full length Aβ, to a truncated Aβ carrying pyroglutamate and a Aβ containing phosphorylated amino acids (Rijal Upadhaya *et al.*, 2014).

Tissue showing AD-pathology is frequently processed and analysed using different amyloid-staining dyes. One of the first and major qualitative method applied for detecting amyloidosis is Congo red dye, which preferably binds to cross-β structures forming Aβ fibrils, as well as native proteins such as elastin and collagen (Yakupova *et al.*, 2019). Several other dyes used to qualitatively analyse amyloids include thioflavin T or S, iodine-sulfuric acid, chrysamine G, curcumin, nanocurcumin, Nile red and many others (Chen *et al.*, 2017). Researchers also employ immunohistochemistry to visualise and localise Aβ aggregates. There are many monoclonal antibodies that target either APP, other Aβ precursor peptides or directly Aβ (Yakupova *et al.*, 2019). Usually only amyloid plaques and amyloid depositions on cerebral veins are detectable by immunohistochemistry with readily available Anti-Aβ antibodies (Thal *et al.*, 2015). Using Anti-Aβ antibodies, it has been shown that different types of Aβ plaques are correlated with AD-like pathology, including neuritic plaques, diffused and cored plaques, presubicular lake-like amyloids, subpial band-like amyloids, fleecy amyloids as well as arteries with depositions of Aβ in the walls and capillary stainings of Aβ (Thal *et al.*, 2000, 2015). Neuritic plaques are formed by the deposition of Aβ, which cause malformations of neurons, such as a dystrophic expansion of axons and dendrites, an accumulation of organelles as well as signaling and cytoskeletal proteins inside of the cell (Thal *et al.*, 2015; Shi *et al.*, 2020). Screening for neuritic plaques is one of the main biomarkers used for diagnosis of AD via autopsy (Mirra *et al.*, 1991; Hyman *et al.*, 2012).

1.4. Hallmarks of Alzheimer's disease

The dementia associated with AD is characterised by neurodegeneration, caused by synaptic injury and neuronal loss. Protein aggregation, brain atrophy, microgliosis and astrogliosis also pose as important hallmarks of AD (Crews and Masliah, 2010). Additionally, impaired blood-brain barrier (BBB), demyelination, altered cell signalling, epigenetics and metabolism as well as acquiring cell death and senescence are associated with developing AD (*Hallmarks of Neurodegeneration*, 2022).

One of the main hallmarks of AD is aforementioned aggregation of Aβ in a form of extracellular neuritic plaques and aggregation of phosphorylated tau in a form of intracellular NFTs (Figure 1) (Nasrabady *et al.*, 2018; Hou *et al.*, 2019). The "amyloid cascade hypothesis" was formed more than 30 years ago, proposing that Aβ aggregates forming plaques are the main cause of dementia and neurotoxicity, common symptoms of AD-like pathology (Glenner and Wong, 1984; Haass and Selkoe, 1993). Later studies show that amyloid plaques do not always cause AD-like pathology (Chen *et al.*, 2017).

Brain atrophy is one of the main hallmarks of AD, characterised by a degeneration of neurons detected in different brain regions of AD patients (Pini *et al.*, 2016). In patients, brain atrophy can be detected *in vivo* using magnetic resonance imaging (MRI) and has been establish as a valuable hallmark of AD, alongside histological analysis performed on brain tissue post mortem (Whitwell *et al.*, 2012). High resolution MRI holds a power to visualise and distinguish structures up to a millimetre and is frequently used to assess the loss in brain volume, change in brain morphology and decrease in subcortical thickness (Pini *et al.*, 2016). In AD patients, reported annual rates in the whole brain atrophy range between 1 % and 4 %. On the contrary, people of similar age, who do not suffer from AD, show annual atrophy rates ranging between 0.3 % and 0.7 % (Frisoni *et al.*, 1999; Marino *et al.*, 2019).

The AD is characterised by the loss of neurons (in number and density) caused by impaired neurogenesis, damages in the synapses and increased neuronal death (Mukhin *et al.*, 2017). Postnatal neurogenesis is restricted to a small region in the brain and number of neurons remain stable throughout adult life (Pakkenberg, 2003; Mukhin *et al.*, 2017). Normal middle aged human brain contains between 85 and 200 billion neuronal cells, with 15-20 billion neuronal cells in the telencephalon, 70-130 billion in the cerebellum and less than a billion in the brainstem and spinal cord (Williams and Herrup, 1988; Vereecken *et al.*, 1994; Simić *et al.*, 1997; Azevedo *et al.*, 2009; Mukhin *et al.*, 2017). During developing AD, different neuronal cell types are differently susceptible to cell degeneration, with excitatory neurons being the most vulnerable cell type (Leng *et al.*, 2021)

Reactive gliosis, which involves activation of macrophages, microglia, oligodendrocytes and astrocytes has been shown as one of the most prominent mechanisms in AD-like pathology (Figure 2) (Nichols *et al.*, 2019; De Sousa, 2022). Accumulation of the Aβ is both causing and stimulating additional reactive gliosis (Osborn *et al.*, 2016; De Sousa, 2022). Astrocytes are the most common type of glial cells in the CNS, defined as star-shaped, non-neuronal cells, important for brain development and maintenance of

the brain homeostasis, maintenance of the BBB and regulation of metabolites and neurotransmitters (Osborn *et al.*, 2016; Matias *et al.*, 2019). Astrocytes are important component of processing circuits in the brain because of their sensitivity to the calcium influx and capability to modulate synapses in response to neuronal signals (Osborn *et al.*, 2016). In the AD-like pathology, astrocytes become activated and form inflammatory responses, followed by various functional, cellular and molecular changes (Figure 1, Figure 2). In a neuroprotective response to the AD, activated astrocytes release cytokines, chemokines and growth factors, stimulate axon growth, synaptic formation and maturation as well as promote viability of neurons and biogenesis of mitochondria (Monterey *et al.*, 2021). In a destructive response to the AD, activated microglia release cytokines that activate astrocytes, especially their β- and γ-secretases, enzymes which cleave APP and supplement neuronal Aβ formation (Monterey *et al.*, 2021). Reactive astrocytes are present in Aβ plaques and NFTs, contributing to impaired homeostasis and cognitive decline (Jurga *et al.*, 2021).

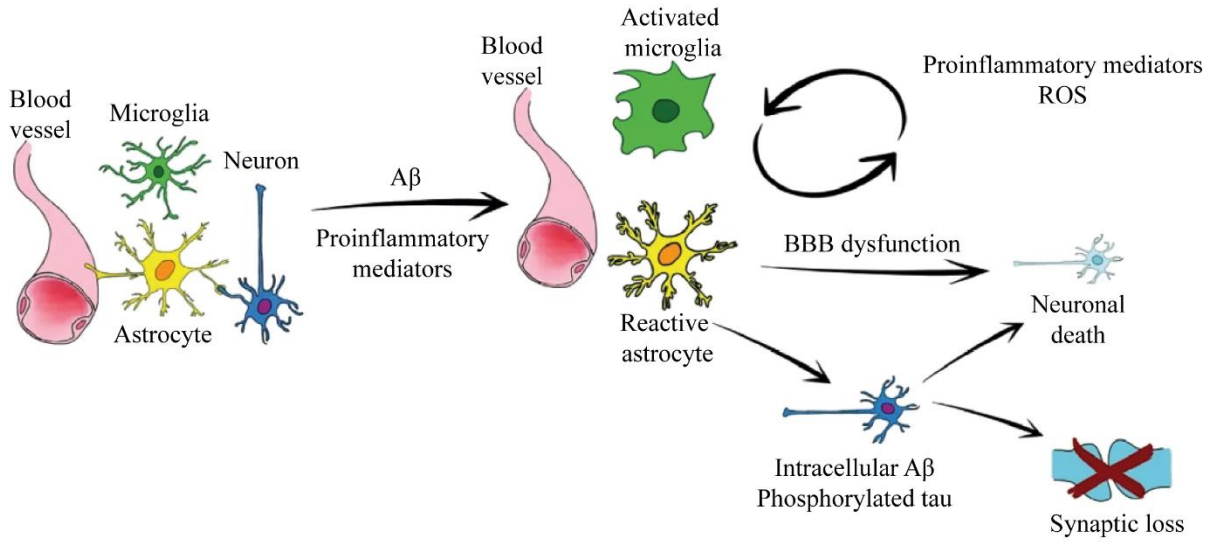

Figure 2. Schematic representation of glial activation in Alzheimer's disease. Upon brain trauma or accumulation of Aβ and neurofibrillary tangles of phosphorylated tau, microglia and astrocytes are activated and lose their physiological functions. The glial activation results in the phenotypic changes, which include enlargement of microglia cell body and branching of astrocytes as well as loss of three-dimensional network. In reactive gliosis, microglia and astrocytes produce various proinflammatory mediators, which cause chronic inflammation, impaired BBB, neuronal death, synaptic loss, and further neurodegeneration. Aβ (amyloid-β), ROS (reactive oxygen species), BBB (blood-brain barrier). Source: Bronzuoli *et al.* (2016).

Upregulation and rearrangement of the intermediate filaments increases in many pathological conditions, including ischemia, brain injury and neurodegenerative diseases, such as AD (Hol and Pekny, 2015). The activation of astrocyte, known as astrogliosis, is marked by an elevated expression of structural marker glial fibrillary acidic protein (GFAP), which is expressed in the normal brain aging as well, albeit to a much lower extent (Munger *et al.*, 2019). GFAP composes the majority of intermediate filament type III in the cytoskeleton of astrocytes, mechanically supporting astrocytes and the BBB (Zhang *et al.*, 2019; Jurga *et al.*, 2021). Several different isoforms of GFAP have been observed

in the human brain (α-, γ-, δ/ε- and κ-GFAP) and one additional in rodents (β-GFAP), with isoform α-GFAP being the most abundant form of GFAP (Jurga *et al.*, 2021). GFAP is expressed mainly in the white matter astrocytes, substantially by cell branches and slightly by their cell body. GFAP is differently expressed by the astrocytes depending on the brain region, with regional density, morphology and proliferation rates of astrocytes significantly varying across the brain (Jurga *et al.*, 2021). Protoplasmic astrocytes that are predominantly localised in the grey matter and connect to the neighbouring neuronal cells and blood vessels, show low levels of expressed GFAP. Contrary to the protoplasmic astrocytes, fibrous astrocytes are located in white matter where they obtain structural function, show high levels of expressed GFAP (Jurga *et al.*, 2021). Other astrocyte cells are radial astrocytes (supporting migrating neurons and neuroblast survival in the developing brain, while in adult brain they localize in the retina as Muller cells), Bergmann astroglia (contacting up to several thousand synapses of Purkinje neurons in the cerebellum), velate astrocytes (expressing water channels and protecting granule neurons in the cerebellum), varicose projection astrocytes and interlaminar astrocytes (both found only in primates), alongside many other astrocytes.

In a healthy brain, microglia (i.e. the resident macrophages of the central nervous system) are in the dormant state and maintain homeostasis by constantly inspecting the surrounding tissue, while peripheral macrophages cannot be found anywhere in the brain (DePaula-Silva *et al.*, 2019). Microglia respond to brain infection, trauma, neurodegeneration and other inflammatory responses (Figure 2) (Gregersen *et al.*, 2000; Zhang *et al.*, 2021). In the AD-like pathology, microglia play two opposite roles. In the neuroprotective scenario, binding of Aβ to pattern recognition receptors on the surface of the microglia moderately activate microglia cells and promote clearance of Aβ from the brain. In the destructive scenario, accumulation of Aβ causes uncontrolled activity of microglia, leading to chronic neuroinflammation, synaptic and neuronal loss and overall cognitive decline (Zhang *et al.*, 2021)

The pathology of AD is usually linked to the brain's grey matter, where neuronal cell bodies responsible for neuronal processing and normal cognitive function are located. However, structural abnormalities in white matter, especially demyelination, have been linked to increased risk and progression of AD (Nasrabady *et al.*, 2018). Myelin loss, caused by impaired function of oligodendrocytes or their precursor cells, is considered to be one of the hallmarks of AD (Nasrabady *et al.*, 2018). Even though oligodendrocytes primarily produce myelin, they also support and regulate neurons, mostly by stabilising neuronal communication (Nasrabady *et al.*, 2018). Several studies show that Aβ induces oxidative stress that damages oligodendrocytes, while damaged oligodendrocytes release iron that promotes Aβ oligomerisation and Aβ accumulation in the grey matter (Nasrabady *et al.*, 2018).

The BBB is the endothelial membrane that protects neurons from potentially damaging factors circulating in the systemic blood (Sweeney *et al.*, 2018). The cells that compose the BBB display tight cell-to-cell contacts, maintaining high electrical resistance and low permeability (Sweeney *et al.*, 2018). Damages in the BBB result in increased permeability, reduced cerebral blood flow and impaired brain

homeostasis. Due to increased permeability of the BBB, toxic molecules, cells and microbes can enter the CNS from the systemic blood, triggering an inflammatory response, which can contribute to the development of neurodegenerative diseases, such as AD.

1.5. Treatments of Alzheimer's disease

Several treatments have been approved for AD and can be divided into two groups. The first group are inhibitors of enzyme acetylcholinesterase, such as donepezil (Aricept) (Bryson and Benfield, 1997), galantamine (Razadyne), and rivastigmine (Exelon), which are prescribed to early- to middle-stage patients and only treat symptoms of the disease (*Alzheimer's Disease (AD) | DrugBank Online*, no date). The second group consists of only one member, named memantine (Namenda), which is prescribed to middle- to severe-stage patients. Memantine targets *N*-methyl-*D*-aspartate (NMDA) channels, inhibits the extra synaptic influx of Ca^{2+} ions and reduces the activity of the neurotransmitter glutamate, thereby improving learning and memory.

However, these treatments are not able to treat the cause or completely stop the progression of AD (*Alzheimer's disease - Treatment*, 2018). In the last few decades, researchers tried to develop different therapeutic strategies for AD, focusing on reducing levels of Aβ oligomers in the brain. For example, strategies can involve overexpressing enzymes that proteolytically degrade Aβ, using antibodies that neutralise oligomers and prevent Aβ aggregation (DeMattos *et al.*, 2001; Wang *et al.*, 2010; Jia *et al.*, 2014) as well as designing catalytic antibodies to hydrolyse aggregates of Aβ and break β-sheets (Nishiyama *et al.*, 2014). Targeting via antibodies would reduce cellular toxicity and inflammation caused by Aβ deposition. Moreover, a focus has been put on possible inhibitory mechanisms, involving small inhibitors of oligomerisation and fibrilization (Felice *et al.*, 2004), β- and γ-secretase inhibitors or blockers of amyloid channels as well as targeting tau protein. Another possible strategy for treatment of AD could be targeting proteases NEP (Huang *et al.*, 2006; Hafez *et al.*, 2011), plasmin (Van Nostrand and Porter, 1999; Tucker *et al.*, 2002), ECE1/2 (Eckman *et al.*, 2001; Eckman *et al.*, 2003) or BACE1/2 (Lee *et al.*, 2005), enzymes that degrade and regulate levels of Aβ (Chen *et al.*, 2017). Monoclonal antibodies inhibit aggregation and plaque formation or clear out existing Aβ plaques by binding to specific parts of Aβ protein sequences and recruiting the immune system (*What new Alzheimer's treatments are on the horizon?*, 2022). In 2021, a monoclonal antibody aducanumab that targets a specific epitope on Aβ peptide was approved by the FDA for the treatment of AD patients in the USA (*Aduhelm | ALZFORUM*, 2022; *What new Alzheimer's treatments are on the horizon?*, 2022).

Research involving animal models and clinical trials have significantly improved the general knowledge about the pathology of AD (Frozza *et al.*, 2018). However, approved and currently tested drugs are still not successful in reversing, delaying or preventing progression of AD. Clinical trials mainly focus on the "amyloid cascade hypothesis" and try to target amyloid peptides. The results may be disappointing

due to the gap in knowledge about other mechanisms underlying complex AD pathology (Frozza *et al.*, 2018).

1.6. Models for studying Alzheimer's disease

The perfect AD model would develop all clinical and pathological biomarkers of AD patients, such as neuronal loss, loss of synapses, cognitive decline, changes in behaviour, brain inflammation and ongoing gliosis, as well as accumulation of Aβ, formation of Aβ plaques and NFTs (Hall and Roberson, 2012). Although no perfect model exists, several different model organisms and model systems have been used as platforms for studying Alzheimer's disease, mainly mice, rats, zebrafish (*Danio rerio*), nematode *Caenorhabditis elegans*, fly *Drosophila melanogaster* and human induced pluripotent stem cells (iPSCs) (Hou *et al.*, 2019). Transgenic mouse models represent the most abundant group, with mice expressing different variants of APP, Aβ, APOE, PSEN1, PSEN2, tau or any combination of mentioned variants. In *C. elegans* and *D. melanogaster*, models were designed to carry knockout mutations in genes coding for APP, overexpress endogenous genes coding for paralogues of human APP, or carry and express human transgenes (Hou *et al.*, 2019). The existing animal models do not display novel mechanisms which have been linked to sporadic AD pathology in human patients.

1.6.1. Mouse models of Alzheimer's disease

Currently, more than 170 mouse models of AD are in use and it is important to note that not a single available model offers an opportunity to investigate the full AD pathology (Hall and Roberson, 2012). Therefore, researchers must bear their specific research questions in mind when making decisions upon which model to choose.

An important factor to take into consideration is a background strain, because the genetic background significantly changes the AD phenotype of the mouse model. For example, some strains have higher levels of anxiety and different activity patterns, while others tend to develop impaired vision and hearing loss, which affects the results of behavioural tests performed on AD mouse models. Moreover, some strains have higher rates of inflammatory and neurodegenerative processes, as well as different learning and memory capacity. Performing experiments on different strains showing AD pathology is preferable and more trustworthy (Neuner *et al.*, 2019).

The first and most frequently used mouse model includes transgenic mice that express human APP (hAPP), carrying different mutations linked to mutations in patients showing AD pathology (Harvey, 2003; Hall and Roberson, 2012). Transgenic AD mouse models oftentimes carry cDNA of human transgene, expressing only one isoform. Several other models express multiple isoforms, synthetised from a whole hAPP transgene or a hybrid minigene containing introns before exon 7 and after exon 8 to allow for alternative splicing. Overexpression of hAPP751 in mice results in more severe AD-like pathology and cognitive decline compared to mouse models with overexpressed hAPP695, probably

due to the fact that hAPP isoforms containing KPI domain undergo amyloidogenic pathway (Hall and Roberson, 2012).

One of the first mouse models of AD is the PDAPP mouse model, carrying the Indiana (V717F) mutation. Mice show cognitive decline and impaired memory before the formation of plaques (around 6 months of age), plaque formation between 6 and 9 months, and expression of dystrophic neurites, gliosis, synapse loss and loss in dendritic density in the hippocampus (Games *et al.*, 1995; Hall and Roberson, 2012). Another widely used mouse model expressing transgenic hAPP is called J20. This mouse model carries both the Indiana and Swedish (K595N/M596L) mutation, expressed in the whole brain. J20 mice accumulate Aβ and form the first plaques between 5 and 7 months of age, with plaques spreading throughout the brain by 10 months of age. Aging mice show elevated gliosis, impaired spatial memory and learning abilities. Another group of transgenic mouse models are mice expressing Aβ and other forms of biologically active APP forms. Several mouse models express Aβ without overexpressing APP (Hall and Roberson, 2012).

Recently, scientists developed a mouse model more precisely recapitulating late-onset AD, with wild-type human Aβ expression controlled by the mouse *App* (Baglietto-Vargas *et al.*, 2021). They changed three amino acids in the mouse Aβ sequence to match hAβ sequence and the results showed cognitive decline with age, loss in synapses, brain shrinkage, changes in inflammation as well as some other features of AD-like pathology. However, despite the increase in soluble $A\beta_{40/42}$, these mice do not form aggregates. In the study, scientists propose several different explanations, including dramatically elevated levels of Aβ required for mice to develop AD-like pathology, a longer asymptomatic period that is necessary for soluble Aβ to aggregate, a stable ratio of $A\beta_{40}$ and $A\beta_{42}$ ameliorating toxic influence of $A\beta_{42}$, impaired protein clearance being prerequisite for Aβ plaque formation, or a combination of various risk factors not present in mice that are required to develop AD-like pathology. This suggests that membership to a different species also influences the onset of AD, and humans might be more prone to develop the disease.

Mouse models are used for studying separate mechanisms underlying AD and some call them "reductionist tools" used to elucidate functions of certain genes and gene products important for development of AD, and potentially figuring out how to prevent that from happening (Hall and Roberson, 2012). Mouse models can form amyloid plaques, NFTs or undergo neurodegeneration, but they do not develop these characteristics spontaneously. Moreover, all of the characteristics develop in different time frames and cannot be observed in the same mouse (Jankowsky and Zheng, 2017). Most of the mouse models recapitulate familial forms of AD in their early- to middle-stage, while most patients suffer from sporadic forms of AD. Mouse models are used to identify and validate various drug targets as well as for preclinical testing of potential drugs (Geerts, 2009). Since most mouse models develop AD-like pathology early during their development, they rule out the influence of aging, which is the main risk factor for developing AD in humans (Baglietto-Vargas *et al.*, 2021).

In summary, mouse models are great for studying AD-like pathology primarily caused by mutations in different genes associated with familial form of the disease, which makes up for smaller percentage of patients. Less frequently, mouse models display sporadic and late-onset AD, more common form of the disease. However, the biggest limitation of all mouse models is that they do not display spontaneous nor age-dependent onset of AD-like pathology.

1.6.2. Zebrafish models for studying Alzheimer's disease

Zebrafish (*Danio rerio*) are small freshwater fish originating from the rivers of India but frequently displayed in aquariums around the world (Newman *et al.*, 2014). When zebrafish first emerged as a model organism, they were used to study vertebrate development. Over the last decade, zebrafish became a prominent model organism for studying many forms of human diseases. Some of the advantages of zebrafish include simple reproduction and maintenance, transparent embryos that develop rapidly and various molecular tools that have been developed to allow efficient genome manipulation. In the past, zebrafish alongside all other teleost fish experienced gene duplication, eventually losing some, but not all duplicated genes (Catchen *et al.*, 2011). Orthologs usually have similar and overlapping functions, which can be troublesome when the aim is to study gene function, since both genes need to be knocked out before a certain phenotype can be observed.

Zebrafish models of AD-like pathology involve APP and Aβ, as well as tau protein. One study generated homozygous *appb* mutants using the CRISPR (Clustered Regularly Interspaced Short Palindrome Repeats) associated with protein Cas9 (CRISPR/Cas9) tool and analysed morphological and behavioural changes (Banote *et al.*, 2020). They observed impaired adhesion of cells in the enveloping layer of the 128-cell stage embryo, resulting in death of severely affected individuals. Moreover, they observed higher levels of expressed *appa*. Mutant fish were smaller compared to the control fish in the early stages of life, with no behavioural changes in early developmental stages. In later stages, fish developed into morphologically normal, healthy and fertile adults. Likely, overexpression of Appa compensates for absent Appb in zebrafish (Banote *et al.*, 2020).

Considering the anatomy of the brain and neurochemical reactions, zebrafish proved to be similar to humans (Saleem and Kannan, 2018). The zebrafish brain can regenerate neurons along the rostro-caudal brain axis throughout the lifetime (Saleem and Kannan, 2018). In one study, researchers injected young and old zebrafish with Aβ peptides (Bhattarai *et al.*, 2017). They tracked the capability of neuronal cells and progenitor cells to undergo neurogenesis and proliferation after Aβ-induced neurodegeneration and observed that age does not influence the regeneration of neurons. Extensive neurogenesis is not typical for the human brain, thus zebrafish models are not the best representative of AD-like pathology, but could prove to be useful for studying mechanisms of regeneration (Saleem and Kannan, 2018).

1.7. African Turquoise Killifish

The African turquoise killifish (*Nothobranchius furzeri*, R. A. Jubb, 1971) has been shown to display several hallmarks associated with sporadic AD, therefore I will also utilise this model organism to study AD-like pathology.

The *Nothobranchius* genus consists of more than 40 described and several undescribed fish species found across continental Africa or on nearby islands (Genade *et al.*, 2005). In the wild, *Nothobranchius* fishes survive in extremely variable climates, with different durations of rainy and dry seasons. All fishes in this genus are annual fishes (fish specifically adapted to have adult life confined to one season), with short life spans and specifically evolved traits for surviving the dry season. Annual fishes show explosive growth, rapidly reach sexual maturity and reproduce and lay eggs that resist desiccation by going into diapause (Genade *et al.*, 2005). Diapause is characterised as a dormant state of the embryo, which protects the embryo from various environmental stressors (Figure 3). (Hu and Brunet, 2018). Diapause observed in laboratory conditions can be divided into three stages. In the first diapause, embryos reach the developmental stage of blastula and do not enter embryogenesis. Embryos can stay in this phase for several years under optimal laboratory conditions. In the second diapause, embryogenesis proceeds, but embryos do not undergo organogenesis. In the third diapause, fully developed fry is capable of hatching and waits for the optimal conditions in the habitat. The optimal housing conditions can result in *Nothobranchius* fishes reaching sexual maturity in less than a month (Genade *et al.*, 2005).

The African turquoise killifish is the shortest-lived vertebrate used for the scientific research (Valdesalici and Cellerino, 2003; Valenzano *et al.*, 2006). The turquoise killifish lives in ephemeral ponds across Zimbabwe and Mozambique, where short 4-month-long, rainy seasons represent the only time of the year when water is present in the habitat (Harel *et al.*, 2015). Like other annual fishes, turquoise killifish goes through a rapid life cycle, develops from a fertilised egg to a sexually mature adult in less than two months and produces eggs which can stay in the embryonic diapause for years (Figure 3). (Genade *et al.*, 2005; Kim *et al.*, 2016). When turquoise killifish was first proposed as a research organism in 2003, the lifespan in captivity was reported to be around 2 months (Valdesalici and Cellerino, 2003). In more recent work, after the establishment of standardized husbandry (Dodzian *et al.*, 2018) median lifespan of turquoise killifish ranges from 4 to 8 months (Valenzano *et al.*, 2015). The median lifespan also depends on the strain of turquoise killifish. Shorter-lived strains, such as the GRZ (collected in Gonarezhou National park in Zimbabwe) and MZM0403 or MZM0401 (collected in Mozambique in 2004), have been extensively used for a number of studies (Terzibasi *et al.*, 2009; Valenzano *et al.*, 2009, 2009; Bartáková *et al.*, 2013; Reichwald *et al.*, 2015). Longer-lived strains, such as ZMZ1001 and ZMZ1007, (collected in Mozambique and Zimbabwe in 2010) and MZM0703 and MZM0403 (collected in Mozambique in 2007) further expand given options when it comes to genetic

backgrounds of turquoise killifish, minimizing the strain-specific observations (Valenzano *et al.*, 2009; Hu and Brunet, 2018).

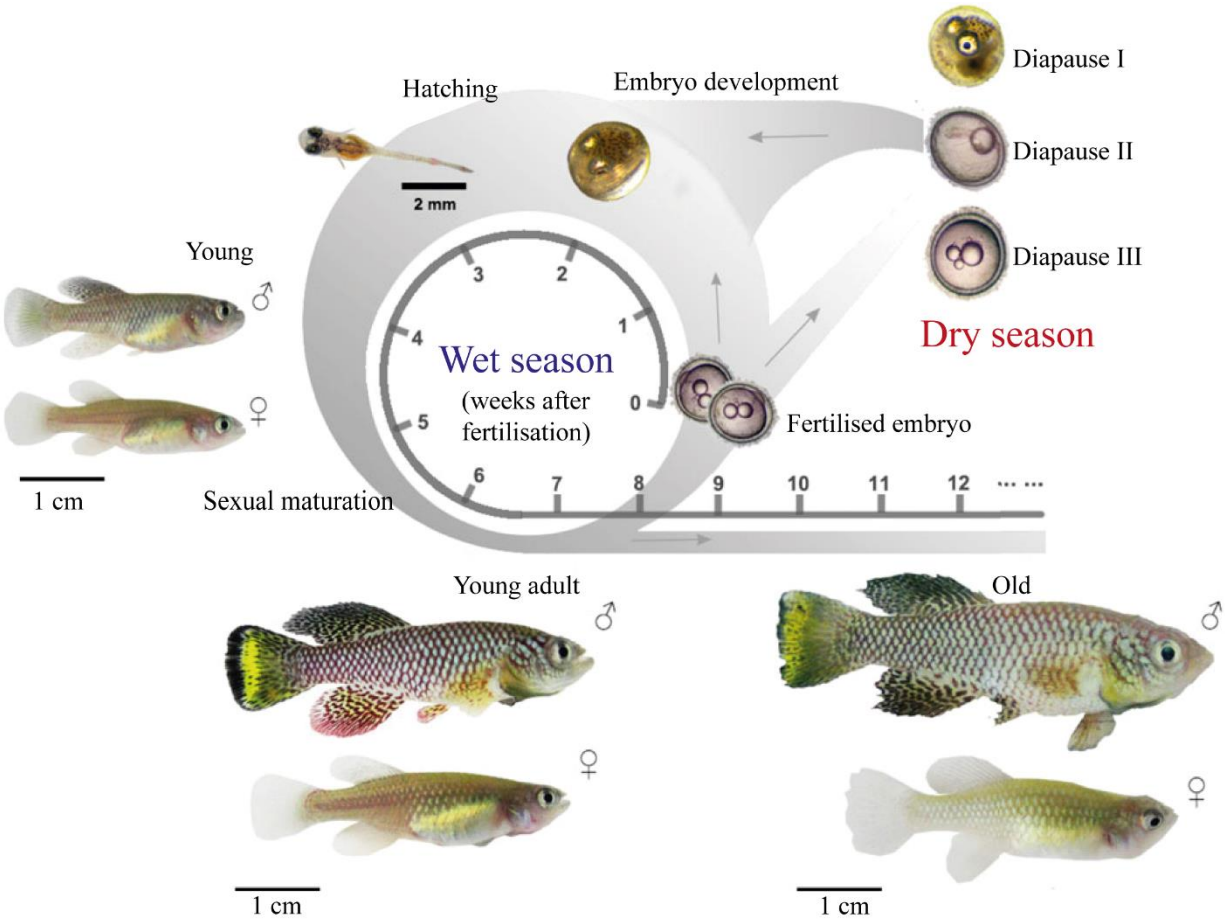

Figure 3. Life cycle of the African turquoise killifish. Turquoise killifish as an annual type of fish goes through a rapid life cycle, develops from a fertilised egg to a sexually mature adult in less than two months and produces eggs which enter embryonic diapause during the dry season. The diapause consists of diapause I, II and III, is characterised by an arrest in development and can last for months or even years. Fish hatch during the wet season in the wild or in laboratory conditions when exposed to the humic acid, and they reach sexual maturation in less than a month and a half. Male fish are larger than females and display fin and body coloration. Females are pale and partially transparent. Aging turquoise killifish display loss of skin pigmentation and spinal curvature. The age of the fish is indicated in weeks. Source: Kim *et al.* (2016).

The genome of turquoise killifish was sequenced, *de novo* assembled and annotated in 2015 by two independent research groups, one at Stanford University in Anne Brunet's laboratory (Valenzano *et al.*, 2015) and the other in Jena, Germany in Matthias Platzer's laboratory (Reichwald *et al.*, 2015). The size of the genome is around 1.53 Gb, with DNA spanning over 19 chromosomes and coding for 22 236 different proteins. 66% of the genome (1.003 Gb) contains repeated elements (Cui *et al.*, 2020). Moreover, telomeres of turquoise killifish are 6-8 kb long, which is similar to the length of human telomeres (Hartmann *et al.*, 2009). Telomeres display age-dependent shortening of their total length, which is also similar to human telomeres (Harel *et al.*, 2015). Unlike many other teleost fish, sexual

determination in turquoise killifish is the same as in humans, with female-specific X chromosome and male-specific Y chromosomes, which determine the sex of individual fish (Valenzano *et al.*, 2009). A key advantage of turquoise killifish as a model organism is a well-established set of techniques to manipulate the fish genome, such as Tol-2 based transgenesis (Valenzano *et al.*, 2011; Hartmann and Englert, 2012; Allard *et al.*, 2013) and RNA-guided CRISPR/Cas9 nuclease allowing for knock-out and knock-in mutations (Jinek *et al.*, 2012; Harel *et al.*, 2015; Harel, Valenzano and Brunet, 2016).

Aging of turquoise killifish recapitulates various characteristics of human aging, such as cognitive, motor and reproductive decline, neural and muscular degeneration, higher susceptibility to different forms of diseases and cancers, loss of skin pigmentation and spinal curvature (Terzibasi *et al.*, 2008; Di Cicco *et al.*, 2011; Baumgart *et al.*, 2015; Hu and Brunet, 2018; Cui *et al.*, 2020). Moreover, on a molecular basis, aging fish show a reduced number of mtDNA copies as well as telomere attrition (Hartmann *et al.*, 2009, 2011). Due to the naturally short lifespan recapitulating human aging and various established techniques, the turquoise killifish has been used to study lifespan, health, diapause, interplay between genetic background and environment, as well as the evolution of aging (Hu and Brunet, 2018). Gut microbiota have been shown to mediate lifespan in the turquoise killifish, with the microbiota transplantation from younger to older individuals resulting in a prolonged lifespan (Smith *et al.*, 2017).

Extensive work on characterising the aging process in turquoise killifish has resulted in several well established biomarkers, including lipofuscin, senescence-associated β-galactosidase and Fluro-Jade B (Kim, Nam and Valenzano, 2016). Elevated concentrations of the autofluorescent pigment lipofuscin, indicating aging organism, have been detected in the liver and brain of aging killifish (Terzibasi *et al.*, 2008). Senescence-associated β-galactosidase, indicating cellular senescence, has been shown to increase in the skin of aging fish (Terzibasi, Valenzano and Cellerino, 2007). Fluoro-Jade B, indicating specifically degenerating neurons, starts increasing in the turquoise killifish brain early on, around 2 months of age (Terzibasi *et al.*, 2007).

Studies on the turquoise killifish brain show how age-dependent impairment of dopaminergic and noradrenergic neurons (Matsui *et al.*, 2019; Vanhunsel *et al.*, 2021), accumulation of α-synuclein (Matsui *et al.*, 2019), age-dependent gliosis (Tozzini *et al.*, 2012) as well as neuroinflammation and low capability of neurogenesis result in tissue scarring (Van Houcke *et al.*, 2021). All these features are characteristic for human brain aging and brain degenerative pathologies, therefore turquoise killifish could emerge as a valuable model recapitulating different human pathologies related to age-dependent brain degeneration.

The cluster of dopaminergic neurons in the posterior tuberculum of teleost fish is corresponding to dopaminergic neurons in the substantia nigra in mammals (Matsui *et al.*, 2012; Matsui *et al.*, 2014), due to the similarity in cell composition, voluntary movement control and spontaneous swimming movements (Jay *et al.*, 2015; Matsui *et al.*, 2019). Matsui *et al.* (2019) showed that dopaminergic and

noradrenergic neurons of turquoise killifish degenerate with age and are associated with PD. Using immunohistochemistry, they first counted the number of tyrosine hydroxylase (TH+) positive neurons and then detected specific sub-types using *in situ* hybridization. They targeted dopamine transporters for dopaminergic neurons and noradrenaline transporter for noradrenergic neurons. Interestingly, they detected that anatomical distribution of these neurons resembles the situation in zebrafish and medaka fish. They calculated the 50% reduction in noradrenergic neurons between 1 and 3 months of age and observed low but statistically significant decrease in dopaminergic neurons. In their study, the number of serotonergic neurons remained relatively stable during aging (Matsui *et al.*, 2019).

Moreover, Matsui *et al.* (2019) detected expression of α-synuclein mRNA in forebrain, diencephalon and hindbrain of turquoise killifish. Again, they used immunohistochemistry and anti-α-synuclein antibody to visualise inclusion bodies containing α-synuclein. They showed that α-synuclein inclusion bodies localised in the medulla and spinal cord of 1-month-old turquoise killifish. In other brain regions levels of α-synuclein gradually increased in the of 3-month and 5-month-old turquoise killifish, progressing from the caudal to the rostral regions. The caudal to rostral α-synuclein progression correlates with earlier degeneration of noradrenergic neurons (localised in the locus ceruleus) compared to dopaminergic neurons (localised in the posterior tuberculum), because locus ceruleus is located more caudally compared to posterior tuberculum.

To explore α-synuclein pathology in more detail, Matsui *et al.* (2019) injected a 5-month-old brain lysate of turquoise killifish into the cerebrospinal fluid of zebrafish. It is important to note that the wild-type zebrafish does not show signs of endogenous α-synuclein (Milanese *et al.*, 2012), so they used a zebrafish strain which had overexpressed human α-synuclein. They detected inclusion bodies of human α-synuclein in zebrafish 1 month post injection, which was not detected in the control individuals of the same strain. The inclusion bodies containing human α-synuclein localised next to α-synuclein from turquoise killifish (detected using two different antibodies). Interestingly, the human α-synuclein was localised in neuronal cells, while the turquoise killifish α-synuclein was localised in astrocytes. The results suggest that injection of α-synuclein from turquoise killifish initiates formation of inclusion bodies of human α-synuclein.

In summary, Matsui *et al.* (2019) showed that turquoise killifish displays neuronal degeneration and formation of α-synuclein inclusion bodies which correlates to the pathology of PD in human patients.

Vanhunsel *et al.* (2021) characterised the visual system of turquoise killifish and disclosed several hallmarks of aging (oxidative stress, cellular senescence, reactive gliosis, neuroinflammation, stem cell exhaustion and changes in the phenotype) present in the retina and brain of turquoise killifish. First, they showed that a growth rate decreased with age in both turquoise killifish and zebrafish (though the fish remain growing throughout their life). Second, they focused on the aging of visual system solely in female turquoise killifish, with the retina and optic tectum being the centre of attention of the research.

Vanhunsel *et al.* (2021) utilised a typical marker of oxidative stress (4-hydroxynonenal, 4-HNE), which is also a by-product of lipid peroxidation (Shao *et al.*, 2006; Zhang *et al.*, 2016), quantified the signal using western blotting and showed that levels of 4-HNE in the retina elevate and in the optic tectum significantly increase with age. Moreover, they quantified a protective antioxidant (heme oxygenase 1, Ho-1) in the retina using immunohistochemistry and showed an increase in levels of the protein in aging individuals. The findings suggest that a visual system of female turquoise killifish experience oxidative stress with age.

The cellular senescence was characterised in the visual system of turquoise killifish using previously established markers, such as phosphorylated gamma H2A histone family member X (γH2AX) which indicates double-stranded DNA breaks (Vanhunsel *et al.*, 2021). The study showed age-dependent DNA damage in the retina and optic tectum of aging turquoise killifish. Furthermore, they analysed the expression of *p21* and *p27*, which are associated with the inhibition of cell cycle, and showed that elevated levels of expression are present in aging turquoise killifish. In the end, they focused on a well-established marker of cell senescence, lysosomal senescence-associated β-galactosidase (SA-βgal), for which they reported elevated levels of expression in both retina and optic tectum. The staining observed in the optic nerve is associated with the senescence of glial cells, since mainly neuronal axons and glia cells localise in that region.

Vanhunsel *et al.* (2021) analysed a protein vimentin, which belongs to the group of intermediate filaments expressed by radial glia in the brain. The study showed increased expression of vimentin in retinal Müller glia and brain radial glia with age, suggesting that the brain, more specifically the visual system, of turquoise killifish undergoes age-dependent reactive gliosis. Next, Vanhunsel et al. (2021) focused on pan-leukocyte marker L-plastin, one of the known markers of neuroinflammation in aging brain. The study presented age-dependent morphological changes in the resident microglia, changing from a branched shape to a more ameboid form. Moreover, they showed an increase in the area covered by resident microglia in the aging retina and optic tectum. The microglia in the brain of aging turquoise killifish show a decrease in the expression of *sirtuin 1, interleukin 10, 6* and *1-b* and an increase in the expression of *tumor necrosis factor* and *interleukin 8* in the retina and optic tectum, which was assess using real-time quantitative polymerase chain reaction (RT-qPCR) (Vanhunsel *et al.*, 2021). The findings suggest that the visual system of aging turquoise killifish undergoes neuroinflammation.

In the visual system of teleost fish, neural stem/progenitor cells (NSPCs) localise in small regions of the retina and the optic tectum (Vanhunsel *et al.*, 2021). The given study focused on the NSPCs in the mitotic niches using immunohistochemistry and double staining for proliferating cell nuclear antigen (Pcna) and sex-determining region Y-box 2 (Sox2). Vanhunsel *et al.* (2021) detected proliferating NSPCs in the retina and optic tectum of adult turquoise killifish. However, an area covered with NSPCs and the proliferation of NSPCs decreased with age, suggesting that the turquoise killifish displays age-dependent stem cell exhaustion.

Furthermore, Vanhunsel *et al.* (2021) performed a morphometrical analysis of the visual system in turquoise killifish, showing a decrease in the thickness of the inner retina as well as a decrease in the number of cells with age. The last thing Vanhunsel *et al.* (2021) focused on was behavioural alternations via optokinetic response tests. They report gradual decrease in fish' responsiveness with age, suggesting that aging impacts primary vision in the turquoise killifish.

As presented here, extensive research in turquoise killifish has demonstrated that this organism displays many hallmarks of aging which have also been associated to the pathology of AD. However, the turquoise killifish has not been utilised as a model organism for AD-like pathology. Brain degenerative pathology detected in the turquoise killifish is promising and further research could help elucidate the question whether this model organism could be suitable to study some other neurodegenerative disorders.

1.8. Aims

The aims of this research are to:

I. Analyze differences between neurodegenerative processes in *N. furzeri* and *D. rerio*.
II. Determine whether amyloid-β is detectable in the aging *N. furzeri* brain.
III. Produce a model to help study the role of amyloid-β in the brain of *N. furzeri*.

2. MATERIALS AND METHODS

2.1. Materials

For this study, I used the African turquoise killifish wild-type strain ZMZ1001 and the zebrafish derivatives of wild-type strain AB.

For the immunohistochemical analysis, I collected the brain tissue from the individuals of different age. For turquoise killifish, I collected the brain tissue from 1.5-month-old time point (6 individual fish), 3-month-old (5 fish), 6-month-old (5 fish), along with 9-month-old time point (7 fish). All killifish were housed in the fish room of the Max Planck Institute for Biology of Ageing until the tissue was collected. Regarding zebrafish, I collected the brain tissue for 3-month-old time point (5 individual fish), 6-month-old (6 fish), 10-month-old (4 fish), 2.5-year-old (5 fish) and 4.8-year-old (6 fish). The 3-month, 6-month and 2.5-year-old individual fish were obtained from the Bakkers' research group from the Hubrecht Institute (Utrecht, the Netherlands). The 10-month-old zebrafish were acquired from the fish room of the Cologne Cluster of Excellence (CECAD) at the University of Cologne (Germany). The 4.8-year-old individual fish were obtained from the Englert's research group from the Leibniz Institute on Aging (FLI) (Jena, Germany).

2.2. Fish husbandry and embryo maintenance

The turquoise killifish (ZMZ1001 strain) were housed in individual 2.8L tanks equipped with baffles, fry mesh and lids glass capillaries (Aquaneering, USA) connected to a system with circulating water. Fish received 12 hours of light and 12 hours of darkness per day. Water temperature was set to 28°C. Fish were fed with brine shrimp nauplii (*Artemia salina*) and blood worm larvae (*Chironomus spp.*) or food pellets twice a day during the week and once a day during the weekend.

Adult fish (6 weeks post hatching) were used for breeding purposes. One male and up to three females were housed in 9.5L breeding tanks equipped with baffles, fry mesh and lids glass capillaries (Aquaneering, USA). Since male African turquoise killifish can be dominant during mating, males similar in body size to females were chosen and tanks were observed in the first few days. The African turquoise killifish lay their eggs in the soil, therefore plastic containers (10x10x5 cm) filled with autoclaved sand up to 2-3cm were placed in the back of the breeding tank.

For fish strain maintenance, embryos were harvested once or twice a week. Embryos were harvested by sieving the sand from the box into the strainer with 0.9 mm strain size and rinsing with system water. The collected embryos were transferred to a 90 mm Petri dish (92x16mm, Sarstedt, USA) and covered with system water. The embryos were then inspected under the Stereo Microscope M80 (Leica, Germany) and damaged and dead embryos were discarded. To prevent contamination with microorganisms living in the system water, I bleached the embryos. Using a disposable 2mL Pasteur pipette (Carl Roth GmbH, Germany), I first discarded the remaining system water from the Petri dish,

then added 50 mL of freshly prepared H_2O_2 (1 µL of 33% H_2O_2 in 100 µL of autoclaved system water, Sigma-Aldrich,USA). I put embryos in H_2O_2 solution on the Orbital shaker 5000 (VWR, USA) for 5 min at a low speed. Using a disposable Pasteur pipette, I removed H_2O_2 solution and washed the embryos two times for 5 minutes with 50 mL Methylene blue concentrated solution (Carl Roth GmbH, Germany), prepared by mixing 35 µL of methylene blue stock solution to 1L of system water.

I transferred the embryos to a new Petri dish filled with 50 mL of methylene blue solution and incubated the embryos at 27-28°C in the incubator Heratherm™ Compact Microbiological Incubator IMC18 (ThermoFischer Scientific, USA). The methylene blue solution prevents parasite contamination and facilitates detection of any unfertilized eggs and dead embryos. Incubation at 27-28°C facilitates synchronous development of the embryos. I replaced old methylene blue solution daily with the fresh batch and discarded dead embryos daily. Since African turquoise killifish embryos can develop at the bottom of dried ponds in nature, it is possible to incubate developing embryos on a moist filter paper plate. 7-10 days post fertilization, embryos start showing visibly black eyes. I transferred any developed embryos to a new Petri dish with slightly damp Whatman paper (GE Healthcare Systems, USA) using a disposable Pasteur pipette. Undeveloped embryos were kept in the methylene blue solution until they developed black eyes. I placed embryos 5 mm apart in a 90 mm Petri dish. I sealed the Petri dish with parafilm M® Laboratory Film (Lab Logistics Group, Germany) and incubated embryos at 28°C for 2-3 weeks, or until fish developed eyes with golden irises. Development of golden irises indicates that embryos can be hatched.

Once the embryos are ready for hatching, they must be transferred to a hatching solution. The hatching solution was prepared by dissolving 1 g/L humic acid powder (Sigma-Aldrich, USA) in system water. The solution was autoclaved and stored at 4°C. Lower temperature of the solution improves hatching success. Developed embryos were carefully transferred to 5 mL of the hatching solution in a 50 mL Falcon tube (Sarstedt, USA) for 1-2 hours. After the first fish hatched, I added 15 mL of system water and fed the fish with brine shrimp nauplii. I kept diluting the hatching solution with system water up to 50 mL. The fish were then transferred to a plastic box used for hatching and incubated at 28°C in the Heratherm™ General Microbiological Incubator OGS180 (ThermoFischer Scientific, USA). Tubes providing air to the solution were a part of the construct. Fish were kept in the hatching solution for 5 days post hatching. The solution was diluted with autoclaved system water in proportion 1:1 daily, maintaining the initial volume. Fish were fed with fresh brine shrimp nauplii twice a day.

Five days post-hatching, I transferred the juvenile fish from the incubator to the water system in the fish room, 1-5 juvenile fish in one 0.8 L tank (with a 400 µm screen in the back). Up until 14 days post hatching, juvenile fish were fed with fresh brine shrimp nauplii. Once they reached 14 days, fish were separated and transferred to 2.8 L tanks (with an 850 µm screen in the back), one fish per tank. Every tank was labelled with specific ID (fish strain, identification number, gender, and hatch date). Screens were taken out from the back of the tank 3 weeks post hatching. Fish were fed with 2 mL of fresh brine

shrimp nauplii and 0.5 mL of blood worms (Poseidon Aquakultur, Germany). From 4 weeks post-hatching onwards, fish were fed with 2 mL of fresh brine shrimp and 1 mL of blood worms. Around 4-week-old fish start showing signs of sexual maturation – fins show coloration in males and abdomens become rounded and full of eggs in females. The fish were treated as adult fish, fed with blood worms or food pellets twice a day.

2.3. Brain isolation and preservation

I isolated brains used for later immunohistochemical analysis from 4-7 individual fish per time point. The turquoise killifish were of four different age representing four different time points, including 1.5-month, 3-month, 6-month and 9-month-old. Zebrafish were of five different ages representing five different time points, including 3-month, 6-month, 10-month, 2.5-year and 4.8-year-old. List of all samples used for this master thesis can be found in Supplementary Data (Supplementary Table 1). Fish were sacrificed over a span of little less than a year. Adult fish were euthanized following the rapid chilling protocol (ethically approved and frequently used in the lab). The fish euthanasia was performed by Dr. Dennis de Bakker. He transferred the fish from their original 2.8 L tank filled with warm system water into a tank filled with cold water (3-4°C). We waited 3 minutes to be sure that fish died, then transferred the fish to an empty Petri dish. Using a scalpel, we immediately cut off the head and transferred it to 1.8 mL of 4% paraformaldehyde (PFA) solution (Carl Roth GmbH, Germany). Since PFA is toxic, the solution must be pipetted into Eppendorf® Safe-Lock microcentrifuge 2.0 mL tubes (Sigma-Aldrich, USA) under the hood with circulating air. Fish heads in the PFA were stored in a dark box and left on a shaker over night at room temperature.

On the second day, we transferred one head at a time to a Petri dish filled with 4% sucrose solution (prepared from >=99.5% sucrose, Sigma-Aldrich, USA). We cut the skull open and carefully isolated the brain from the skull. We then transferred the brain to 1.8 mL of 4% sucrose and left it at room temperature for 5 minutes. The washing step in 4% sucrose was repeated one more time. We transferred the tissue to 1.8 mL of 30% sucrose and left it overnight in the fridge at 4°C.

On the third day, we transferred the tissue to a plastic Tissue-Tek Cryomold, 10mm x 10mm x 5mm (Sakura Finetek, USA). We pipetted any excess fluid out of the cryomold and dried it with paper. We used Tissue-Tek O.C.T. Compound (Sakura Finetek, USA) to cover the brain tissue and fill up the plastic mould. The brain tissue was positioned in the right orientation – ventral part of the brain facing the bottom of the mould, anterior and posterior part of the brain following the shape of the mould. We quickly froze the sample on dry ice, while keeping the mould in a flat position and in the box for several minutes before storing it at -80°C. Every sample was assigned a specific number, which corresponds to the number in the lab's tissue database.

2.4. Cryosectioning of the brain tissue

The brains embedded in the O.C.T. Compound (Sakura Finetek, USA) were kept at -80°C before sectioning. I transferred the blocks on dry ice to the FACS and Imaging Core Facility of the Max Planck Institute for Biology of Aging, where I sectioned the blocks using the Cryostat Cryo Star NX-70 machine (Epredia, USA), while following standard protocol for cryosectioning. I cut all brains into 10 µm thin sections and placed the tissue on Epredia Superfrost Plus glass slides (Thermo Fisher Scientific, USA). For each sample, I placed the tissue sections onto between 14 and 20 slides, depending on the brain size. Slides covered with tissue sections were stored at -80°C.

2.5. Immunohistochemistry

Immunohistochemistry (IHC) was performed following a previously established protocol in the lab. The slides with tissue sections were thawed at room temperature. For each round of immunohistochemical staining, I prepared fresh solutions, including PEM, PEMTx, NH_4Cl-PEMTx and Na-citrate solution. The PEM solution (pH 7.5) consisted of 80 mM 98.5+% PIPES (1,4-Piperazin-bis-(ethansulfonacid), Acros Organics, USA), 5 mM EGTA (PanReac AppliChem ITW Reagents, USA) and 1 mM $MgCl_2$ (Sigma-Aldrich, USA), diluted in milliQ water. The PEMTx solution was prepared from PEM solution, by adding 0.2% Triton X-100 (Sigma-Aldrich, USA). The NH_4Cl-PEMTx solution was prepared by diluting 50 mM of NH_4Cl (Sigma-Aldrich, USA) in PEMTx solution. The Na-citrate solution contained 10 mM 99% Trisodium Citrate Dihydrate (Alfa Aesar, USA) in RO H_2O.

First, I washed the slides in PEMTx solution for 10 min, then in NH_4Cl-PEMTx solution for another 10 min, and then 2 more times in PEMTx. The slides were then transferred and incubated in Sodium Citrate Solution (pH 6) for 15 min at 84°C in the Waterbath WNE 14 (Memmert, Germany). The tissue had to be at room temperature before proceeding with additional steps, therefore the slides were cooled down in a plastic chamber for 5 min under running water in the sink. Afterwards, I washed the slides again in PEMTx solution 2 times for 10 min. The slides were partially dried, and a hydrophobic barrier was created around the tissue with the ImmEdge Hydrophobic Barrier PAP Pen (Vector Laboratories, USA) to prevent solutions from leaking outside of the tissue area. I incubated the slides containing the tissue sections with blocking solution for 1-2 h at room temperature. The blocking buffer solution was prepared each time depending on the number of slides which were stained. For one slide, I combined 100 µL of Fetal Bovine Serum (FBS, Thermo Fisher Scientific, USA) and 10 µL of Dimethyl sulfoxide (DMSO, ACS reagent, Sigma-Aldrich, USA) with 890 µL of PEMTx solution. Afterwards, I incubated the slides with a primary antibody, which was diluted in a blocking buffer, at 4°C overnight in a humidified chamber. Primary antibodies were used in different dilutions, as indicated in Table 1. For the turquoise killifish tissue, Rabbit polyclonal purified Anti-Abeta-pE11 primary antibody (Synaptic Systems, Germany Cat# 218603, RRID: AB_2619913) was combined with DAPI on one set of slides, and Mouse monoclonal purified Anti-NeuN primary antibody, clone A60, (Sigma Aldrich. USA, Cat# MAB377)

and Rabbit polyclonal purified Anti-GFAP primary antibody (Agilent, USA, Cat# Z0334, RRID: AB_10013382) with DAPI on the other set of slides. For zebrafish tissue, Rabbit monoclonal purified Anti-NeuN antibody [EPR12763] (Abcam, UK, Cat# ab177487, RRID: AB_2532109), was combined with DAPI on one set of slides and Rabbit polyclonal purified Anti-GFAP primary antibody (Agilent, USA, Cat# Z0334, RRID: AB_10013382) with DAPI on the other set of slides. For every individual, I stained between 1 and 3 set of slides per combination of antibodies, depending on the quality of sections.

The following day, I first washed the slides with tissue sections in PEMTx solution 5 times for 20 minutes (on a shaker). The slides with the secondary antibody (1:500) and DAPI (dilution 1:1000) diluted in a blocking buffer for 1-2 h at room temperature in a humidified chamber and in the dark. I combined primary antibody Rabbit Anti-Abeta-pE11 with secondary antibody Alexa Fluor® 647 Donkey anti-rabbit IgG (min. x-reactivity) antibody (BioLegend, USA, Cat# 406414, RRID: AB_2563202). For primary antibodies Rabbit Anti-NeuN and Rabbit Anti-GFAP antibodies I used secondary antibody Alexa Fluor 555 (Thermo Fisher Scientific, USA, Cat# A-21428, RRID: AB_2535849). I combined primary antibody Mouse Anti-NeuN with secondary Goat anti-Mouse IgG (H+L) Cross-Adsorbed Secondary Antibody, Alexa Fluor 647 (Thermo Fisher Scientific, USA, Cat# A-21235, RRID: AB_2535804). The slides were washed in PEMTx solution 5 times for 10 min, then 2 times for 7 minutes in PEM solution (on the Orbital shaker 5000 (VWR, USA) and in the dark). I mounted every slide separately in ProLong Gold antifade reagent (ThermoFischer Scientific, USA) to diminish photobleaching and allow long-term storage of the samples. I sealed the slides with transparent nail polish to prevent evaporation and stored them at 4°C in the dark.

Table 1. Primary and secondary antibodies used for immunohistochemical analysis of the turquoise killifish and zebrafish brain samples.

Primary antibody	**Dilution**	**Secondary antibody**	**Dilution**	**Applied for**
Rabbit Anti-Abeta-pE11	1:200	Donkey anti-Rabbit Alexa Fluor 647	1:500	Turquoise killifish
Rabbit Anti-NeuN	1:1000	Goat anti-Rabbit Alexa Fluor 555	1:500	Zebrafish
Mouse Anti-NeuN	1:150	Goat anti-Mouse Alexa Fluor 647	1:500	Turquoise killifish
Rabbit Anti-GFAP	1:200	Goat anti-Rabbit Alexa Fluor 555	1:500	Turquoise killifish Zebrafish

* Dilutions are indicated in the table as a proportion of antibody and blocking buffer solution.

2.6. Fluorescence imaging

The slides were imaged in batches using Zeiss Axio Scan.Z1 microscope (Carl Zeiss, Germany), with a Plan-Apochromat 20x/0.8 M27 objective, Axiocam 506m imaging device and 1x Camera Adapter. Different imaging settings were used for different stainings (Table 2.). For all types of staining the effective numerical aperture was 0.8 and the binning mode 1.1.

Table 2. Imaging settings used for different antibody stainings. Abbreviations stand for the turquoise killifish (NF) and zebrafish (DR).

Primary Antibody	**Secondary Antibody**	**Light Source (Intensity)**	**Illumination Wavelength (nm)**	**Excitation Wavelength (nm)**	**Emission Wavelength (nm)**	**Exposure Time (ms)**	**Focus Depth (µm)**
Anti- Abeta-pE11 (NF)	Alexa Fluor 555	LED-Module 630nm (75%)	615-648	548	561	50	1.75
Anti-NeuN (DR)	Alexa Fluor 647	LED-Module 567nm (100%)	540-570	558	575	100	1.80
Anti-NeuN (NF)	Alexa Fluor 647	LED-Module 630nm (50%)	615-648	548	561	50	1.75
Anti-GFAP (NF)	Alexa Fluor 555	LED-Module 567nm (50%)	540-570	558	575	50	1.80
Anti-GFAP (DR)	Alexa Fluor 555	LED-Module 567nm (50%)	540-570	558	575	40	1.80
DAPI (NF, DR)		LED-Module 385nm (20%)	370-400	353	465	10	1.45

2.7. Image processing and signal quantification

2.6.1. Program ZEN 3.5 (Blue Edition)

Imaging results from the AxioScan microscope were stored in grouped files with all images from the same slide in one .CZI file. First, I processed the big files in a program ZEN 3.5 (Blue Edition) ZEN Digital Imaging for Light Microscopy (RRID:SCR_013672). All channel colours were set to the white channel for easier processing later. Using the command Draw Region of Interest (ROI), I selected specific brain regions and created a subset of images in the program. I chose up to three well preserved sections of the same brain region per individual slide and saved each section of a specific brain region as a separate .CZI file, with a distinctive name that indicated brain region, but not the condition.

2.6.2. Program Fiji (ImageJ2)

I loaded the separate images in .CZI file forms to a program, Fiji (ImageJ2) (RRID:SCR_002285), as a hyper stack in auto scaled grayscale colour mode and with split channels. First, I manually adjusted Level and Window balances to optimal intensity (with a detectable positive signal, while trying to avoid overexposing of the image). The region of interest was selected by drawing „freehand“ around it. I adjusted the threshold to cover as much of the positive signal as possible, without picking up any background signal. In certain zebrafish brain regions, the vascular tissue (blood vessels) was more intensely stained with Anti-NeuN than real neuronal signal. For those samples I subdivided regions of interest based on the shape of the positive signal, separately quantified the signal and later added all values together. I analysed specific region of interest by particle size (0-Infinity) and circularity (0.00-1.00). The results were summarised showing particle count, total area of the signal, average size of the particle, percentage area covered by the signal, mean grey value and integrated density value. The circularity value of 0.00 marks very irregular shapes, while the circularity value of 1.00 marks perfectly shaped circles. By adjusting circularity parameters to 0.30-1.00, the program was able to exclude extremely elongated shapes from the sample. This expedient helped solve the problem of blood vessels (elongated in shape) being stained alongside NeuN positive signals (rounded) in the brains of zebrafish.

2.6.3. Processing of representative images

I processed the acquired images of the tissue sections, which I present in the results in a different way, in the ZEN 3.5 program. I assigned different colours to different antibody stainings (yellow to Anti-Abeta, magenta to NeuN, green to GFAP, and dark blue to DAPI). Intensity settings were constant between different time points and brain regions of the same staining. For the turquoise killifish tissue, I set the intensity interval to 100-2000 for Anti-Abeta, 100-3000 for Anti-NeuN, 100-3000 for Anti-GFAP and 100-5000 for DAPI. For zebrafish tissue I set the intensity interval to 100-5000 for NeuN, 100-6000 for Anti-GFAP and 100-10000 for DAPI. I saved the images of regions of interest as .TIFF files and later rearranged them in Adobe Illustrator 2021 (RRID:SCR_010279).

2.8. Data analysis and statistics

I stored the collected data on quantified positive signals in a Microsoft Excel sheet, with each value under blinded file name. First, I decoded each file name and assigned a corresponding slide number from the database, the species name and time point. For some samples I processed more than one slide, so in the end there were more than 3 sections of a particular brain region for an individual brain. In that case, I down sampled the number by randomly choosing 3 values from the list (performed using https://www.random.org/lists/).

Brain size was calculated with the following formula:

$$Size\ of\ a\ Brain\ Region\ of\ Interest = \left(\frac{Total\ Area\ of\ Positive\ Signal}{\%\ of\ Positive\ Cross\ Sectional\ Surface\ Area}\right) * 100$$

For every brain region I calculated an average value of percentage of cross-sectional surface area covered with positive signal, as well as a total average of all brain regions for individual samples. For the total average of individual samples, I considered only samples with all brain regions with at least one value.

I further analysed the data on average brain sizes and percentages of cross-sectional surface area in the program GraphPad Prism Version 9.3.1. (RRID:SCR_002798). The ordinary one-way ANOVA test was performed to compare four different time points for the turquoise killifish and five different time points for the zebrafish. I performed a non-parametric Mann-Whitney test to compare 1.5-month and 6-month-old time points for the turquoise killifish as well as 3-month and 2.5-year-old time points for the zebrafish. I created graphs using the program GraphPad Prism.

2.9. Protein alignment

To determine how similar protein sequences of APP from turquoise killifish and zebrafish are to protein sequences from humans (*H. sapiens*) and mice (*M. musculus*), I aligned full-length peptide sequences in a program called Unipro UGENE (RRID:SCR_005579). Multiple protein sequences were aligned with the MUSCLE default mode. I downloaded the sequences of all protein variants from online database Ensembl (https://www.ensembl.org/index.html).

2.10. CRISPR/Cas9 transgenesis

2.10.1. Guide RNA design and synthesis

I used CRISPR/Cas9 tool to edit the genome of the turquoise killifish. First, I designed the guide RNA templates using an online program CHOPCHOP (https://chopchop.cbu.uib.no/). Using the CRISPR/Cas9 for knock-out of the gene of interest, I targeted exon 2 of *appa* and exon 3 of *appb* in the turquoise killifish. I downloaded the FASTA formats of the genes of interest from the Ensembl. From multiple selection, I selected two possible guide RNAs for *appa* and one for *appb* (bold label in Table 3.). I designed the template ssDNA target-specific oligonucleotide to synthesise gRNA by adding an overlapping nucleotide sequence to the N-terminus and T7 promoter sequence to the C- terminus (Table 3.). I removed the PAM sequence (NGG) because it is only required for recognition of the target sequence by the Cas9 protein, but it is not part of the sgRNA sequence. I ordered templates online, which were synthesised and delivered by a company called Integrated DNA Technologies (https://eu.idtdna.com/pages/products/custom-dna-rna/dna-oligos).

I synthesised the sgRNAs using the EnGen® sgRNA Synthesis Kit(New England BioLabs, USA, #E3322V), according to their standardized protocol. I cleaned the synthesised sgRNAs with the

Monarch® RNA Cleanup Kit (50µg, New England BioLabs, USA, #T2040L), following the instructions. I eluted the sgRNA in 20 µL of nuclease-free water (1 min elution and 1 min spinning time) and kept it on ice. The concentrations of purified sgRNA products were measured using the spectrophotometer NanoDrop™ 2000 (ThermoFischer Scientific, USA). For CRISPR/Cas9 injections, concentration of sgRNA solution was adjusted to 300 ng/µL.

Table 3. Templates of ssDNA target-specific oligonucleotides used for sgRNA synthesis. sgRNA sequence designed by program CHOPCHOP (bold bases), with N-terminus overlapping nucleotide sequence and C-terminus T7 promoter sequence on each side (not bold bases).

Target gene	**Template sequence (N- to C-terminus)**
appa – exon 2	TAATACGACTCACTATAGG**TCAACGTTCAGAGCGGCAAG**GTTTTAGAGCTAGAAATAGCA
appa – exon 2	TAATACGACTCACTATAGG**CAAGTGGGAGTCCGACCCCT**GTTTTAGAGCTAGAAATAGCA
appb – exon 3	TAATACGACTCACTATAGG**AAACCCACCGAGTCATCCAAAG**GTTTTAGAGCTAGAAATAGCA

2.10.2. CRISPR/Cas9 injections

I prepared the CRISPR/Cas9 and gRNA reaction mix with EnGen® Spy Cas9 NLS (20 µM, New England Biolags, USA), by mixing 1 µL of Cas9 NLS, 1 µL of each purified sgRNA (300 ng/µL), 2 µL Phenol Red for visualisation and nuclease free water up to 10 µL. I kept the reaction mix on ice until further use. I pulled the needles from glass capillaries 1.0 OD x 0.58 ID x 100 L mm (Harvard Apparatus, USA), using a micropipette puller machine P-1000 Next Generation Micropipette Puller (Sutter Instrument, USA) with the program previously established in the lab.

For CRISPR/Cas9 injections, the embryos need to be in a one- or two-cell developmental stage, which means they need to be collected shortly after fertilisation. I collected the embryos from the tanks housing the turquoise killifish ZMZ1001 breeders 3 hours after putting the sand box into the tank. I collected the embryos as described before, with dead and damaged embryos discarded from the pool. I transferred the embryos fit for injections to the agarose plate covered with methylene blue solution. I prepared the agarose plate by dissolving 0.75 g of Agarose Standard Roti®garose for DNA/RNA Electrophoresis (Carl Roth GmbH, Germany) in 50 mL 1x TAE buffer, pouring it into a Petri dish with a specific mould designed in the lab, boiling the mixture first using Microwave MW 7891 (Severin, Germany) and then cooling it down. I carefully positioned the embryos in rows in the agarose, with one- or two-cell embryo facing the needle holder at approximately 45°. Using Microloader™ Microcapillary Tips (Eppendorf, Germany), I loaded 1.5 µL of the reaction mix in the injection needle and loaded the needle on the needle holder connected to the source of nitrogen pressure Pressure Injector MPPI-3 (Applied Scientific

Imaging, USA). I adjusted the pressure manually during injections. I injected a small amount of reaction mix directly into the embryos one at a time.

I transferred the injected embryos to a new Petri dish with clean methylene blue solution and checked daily until they developed black eyes. I transferred the developed embryos to the plates with moist filter paper, further processed and hatched the embryos as described before.

2.11.3. Genotyping protocol

To genotype CRISPR/Cas9 injected fish and their progeny, I developed a genotyping protocol, which includes isolation of the DNA, PCR amplification of the target region of interest and purification of the PCR amplicons. I isolated fish DNA from 2-4 scales which I collected from the posterior part of the body of sexually matured fish (minimum 5-6 weeks of age). I transferred the scales to 50 µL of SEL buffer previously prepared in the lab (Table 4.). I added 2 µL of Proteinase K per 100 µL of the isolation buffer and the reaction mix was kept on ice. I incubated the scales in SEL isolation buffer and Proteinase K in the Touch™ Thermal Cycler C1000 (Bio-Rad Laboratories, USA) at 60°C for 1 h, 90°C for 15 min and 12°C until tubes were taken out of the machine. I stored the isolated DNA at 4°C. Since SEL buffer is compatible with the following PCR reaction, isolated DNA did not have to be additionally purified.

I used the isolated DNA as a template for PCR amplification of the target region of interest. I prepared each reaction mix (25 µL) by mixing 12.5 µL of *Taq* 2X Master Mix (New England Biolabs, USA), 0.5 µL Forward/Reverse Primer, 9 µL of Nuclease Free Water and 2.5 µL of the DNA sample. I tested several different primer pairs and picked out one primer pair for each target region (Table 5). Moreover, I tested different conditions of PCR reaction and in the end used the setup with the highest yield of DNA amplicons (Table 6). I stored the PCR amplicons at 4°C until further use.

Table 4. Components of SEL buffer used for DNA isolation from scales of the turquoise killifish.

Component	**Concentration**	**Volume (mL)**
KCl	1M	25
$MgCl_2$	1M	1.25
Tris pH 8.3	1M	5
Igepal	10%	2.25
Tween-20	10%	2.25
Gelatine	0.1%	50
miliQ H_2O		Up to 500

Table 5. Primer pairs used for genotyping of CRISPR/Cas9 injected fish and their progeny.

Primer Orientation	Target Region of Interest	Primer Sequence	Amplicon Length
Forward	*appa*, exon 2	CCTCTCTTTCAGGTCCCCAC	209 bp
Reverse	*appa*, exon 2	TTTTCTGCTCTGCTTTTAGGC	
Forward	*appb*, exon 3	AAGCTGCACAAGACCTTTGG	267 bp
Reverse	*appb*, exon 3	GCATTGCTGTCTAACTCCGC	

Table 6. Conditions of PCR reactions used for genotyping of CRISPR/Cas9 injected fish and the progeny.

Step	Time	Temperature (°C)	Number of cycles
1.	3:00	95.0	1x
2.	0:45	95.0	35x
	0:30	55.0	
	0:45	72.0	
3.	5:00	68.0	1x
	∞	10.0	

I purified PCR amplicons following a slightly adjusted magnetic bead clean up protocol. For short DNA fragments (200-300 bp), the proportion of DNA and magnetic beads should be 1:2. Beforehand, beads must be calibrated to the room temperature. Magnetic beads for DNA purification were previously made in the lab from Sera-Mag SpeedBead Carboxylate-Modified Magnetic Particles (Hydrophylic), (GE Life Sciences, now Cytiva, USA). I mixed DNA amplicons and beads in proportion 1:2, thoroughly pipetted the whole reaction 10-20 times and left it at room temperature for 5 min. I put the tubes on a magnetic stand DynaMag™-PCR Magnet (ThermoFischer Scientific, USA) for 5 min. I discarded the water from the tubes and washed the beads with freshly prepared 80% EtOH (prepared from 100% EtOH, VWR, USA) for a maximum of 30 s. I discarded the EtOH and repeated the washing step one more time. I discarded the EtOH again and dried the beads on air for up to 3 min to prevent cracking. I eluted the DNA from the beads with nuclease-free water (I adjusted the volume based on the initial volume of the

DNA amplicons and beads). To enhance elution, I put the tubes on the Orbital shaker 5000 (VWR, USA)for around 30 min. I stored the purified DNA at 4°C until further use.

I analysed the purified DNA using agarose-gel electrophoresis or Sanger sequencing. For analysis using electrophoresis, I loaded the DNA and 100 bp DNA Ladder (Promega Corporation, USA) to a 4%-agarose gel (Agarose Standard Roti®garose for DNA/RNA Electrophoresis, Carl Roth GmbH, Germany). The gel was submerged in the Rotisphere®10x TBE Buffer (Carl Roth GmbH, Germany), which was poured into the Sub-Cell® GT Cell (M/L) (Bio-Rad Laboratories, USA) connected to the PowerPac™ Universal Power Supply (Bio-Rad Laboratories, USA). I ran the electrophoresis at 90-100 V for at least 45 min, or until bands separated on the gel. Gels were illuminated with UV light using ChemiDoc™ MP Imaging System (Bio-Rad Laboratories, USA). For Sanger sequencing, I prepared the sequencing reaction mixture by mixing around 5 µL of the purified PCR product, 10 µL of nuclease free water and 2 µL of either forward or reverse primer (Table 5). I sent the tubes with reaction mixtures for Sanger sequencing to Eurofins Genomics (https://eurofinsgenomics.eu/). I analysed the results manually by comparing the wild-type control sequence to the sequences containing double peaks, indicating mutations.

3. RESULTS

3.1. Comparison of brain degeneration between turquoise killifish and zebrafish

3.1.1. Brain size changes in the aging turquoise killifish

Most studies on the brain aging and degeneration in turquoise killifish, which involve astrogliosis and neuronal changes, focus on certain brain regions and research involving the whole length of the brain tissue is scarce. In this thesis, I aim to analyse cross-sections spanning from the most anterior to the most posterior part of the brain, which would help me elucidate whether brain degeneration varies between different brain regions, or if this process happens across the whole brain at the same time.

To analyse brains of turquoise killifish and zebrafish, I performed IHC analysis of the cross-sections of the whole brain tissue. Brains follow the rostro-caudal axis, meaning that the neural tube can be subdivided into anterior/posterior segments. Looking at the shape of the brain, the brain of the fish is longitudinal, while human brains display a C-shape. I divided the brain into seven different brain regions (Figure 4A-B), which correspond to the main anatomical brain regions. The telencephalon (TC) is in the most anterior part of the brain, continued by the optic tectum (OT) surrounding the hypothalamus. I divided the hypothalamus into two regions: hypothalamus superior lobe (HSL) and hypothalamus inferior lobe (HIL). I divided the more posterior part of the brain into the cerebellum (CB) and rhomboencephalon. The CB is the brain region with the largest quantity of cell nuclei, located above the anterior rhomboencephalon (AR) in the same cross-section. I divided the rhomboencephalon into two regions: the AR and the posterior rhomboencephalon (PR). I analysed each half of the brain section as a separate repeat, and further in the text I refer to it as a brain hemisphere.

The median life span of the turquoise killifish is between 4 and 8 months, with a maximum lifespan of around a year. In zebrafish, the median lifespan is around 2.5 years and maximum lifespan around 5.5 years. To observe the hallmarks of AD-like pathology across several timepoints from young to old individuals, I analysed the cross-sections of four different time points in turquoise killifish, ranging from young adults (1.5 months), adults (3 and 6 months) and old (9 months) individuals. In zebrafish, I analysed the cross sections from individuals of five different time points, ranging from young adult (3 and 6 months), adult (10 months and 2.5 years) to old (4.8 years) fish. To compare the size of the brain tissue between turquoise killifish and zebrafish, I calculated the total surface area of a certain brain region from the cross-sectional surface area and the percentage of cross-sectional surface area positive for GFAP signal. The average value of the size of every brain region hemisphere was calculated from separate brain sections.

Several brain regions in turquoise killifish expand almost 2-fold over the course of less than 5 months (from 1.5 months to 6 months), after which they shrink by an average of 10-20 % in 9-month-old fish. (Figure 4C). I observed an increase in brain size followed by a decrease in the brains of old turquoise

killifish across all brain regions. I tested the difference between the sizes across different brain regions using an ordinary one-way ANOVA analysis. The results support the significant difference within all brain regions across the brain of turquoise killifish, including the TC (P value <0.0001, R^2 0.7450), the OT (P value 0.0002, R^2 0.6338), the HSL (P value <0.0001, R^2 0. 8495), the HIL (P value <0.0001, R^2 0. 8310), CB (P value 0.0007, R^2 0.5994), the AR (P value <0.0001, R^2 0.6984) and the PR (P value 0.0016, R^2 0.5434).

Moreover, I tested a difference between 1.5-month and 6-month-old turquoise killifish. The results support the observed significant increases in size in all brain regions (P value 0.0043). In addition, I observed a general trend showing a decrease in cross-sectional surface area between 6- and 9-months in all brain regions, with a significant difference found in the OT (P value 0.0480), the HSL (P value 0.0101), the HIL (P value 0.0051) and the PR (P value 0.0480).

In zebrafish, the brain grows throughout the lifetime, with every brain region gradually increasing in size between 3-month-old and 4.8-year-old individuals (Figure 4D). In comparison to the turquoise killifish, I observed that the zebrafish brain expands around 30 % per brain region over the course of 4.5 years. For most of the brain regions, the average brain sizes fluctuate between two neighbouring time points (mostly between 10 months, 2.5 years and 4.8 years), but the general trend displays an increase in size over time. To test the difference between all five time points, I performed the ordinary one-way ANOVA test. The test does not support the question for several brain regions, resulting in no significant difference in the size of zebrafish TC, HSL and PR, even though the brain regions show a general increase in brain size over time. Performed ordinary one-way ANOVA test supports the results in the remaining brain regions, with a significant difference in the OT (P val 0.0008, R^2 0.5803), the HSL (P val 0.001, R^2 0.5704), the CB (P val 0.0008, R^2 0.5949) and the AR (P val 0.0014, R^2 0.5555).

Moreover, I questioned whether the observed difference between 3-month-old and older time points in zebrafish holds any significance, therefore I performed a non-parametric Mann-Whitney test. Between 3 and 6 months of age, the test resulted in no significant differences in any of the brain regions. Between 3 months and 10 months, the test supports the results with a significant difference observed only in the OT (P val 0.0159). Between 3 months and 2.5 years of age, the test for the HSL supports the results with a significant difference (P val 0.0317). Between 3 months and 4.8 years of age, the test supports the results with a significant difference in the OT and the HSL (both with P val 0.0043) and the CB (P val 0.0095).

Overall, I found that the brains of turquoise killifish have a larger cross-section area compared to the same areas of zebrafish, and overall brain size is larger in turquoise killifish than in zebrafish observed upon brain isolation from the skull (data not shown). By comparing the sizes of brain hemispheres, divided into seven different brain regions along rostro-caudal brain axis, I noticed that the brain size of turquoise killifish is almost double the size of the brain size of zebrafish. Moreover, all seven brain

regions in turquoise killifish seem to expand until fish reach 6 months of age, while the brains of zebrafish seem to constantly grow throughout life. I observed that turquoise killifish displays a decrease in brain size between 6-month-old and 9-month-old individuals, referred to as the brain atrophy, which correlates to the AD-like pathology in human patients.

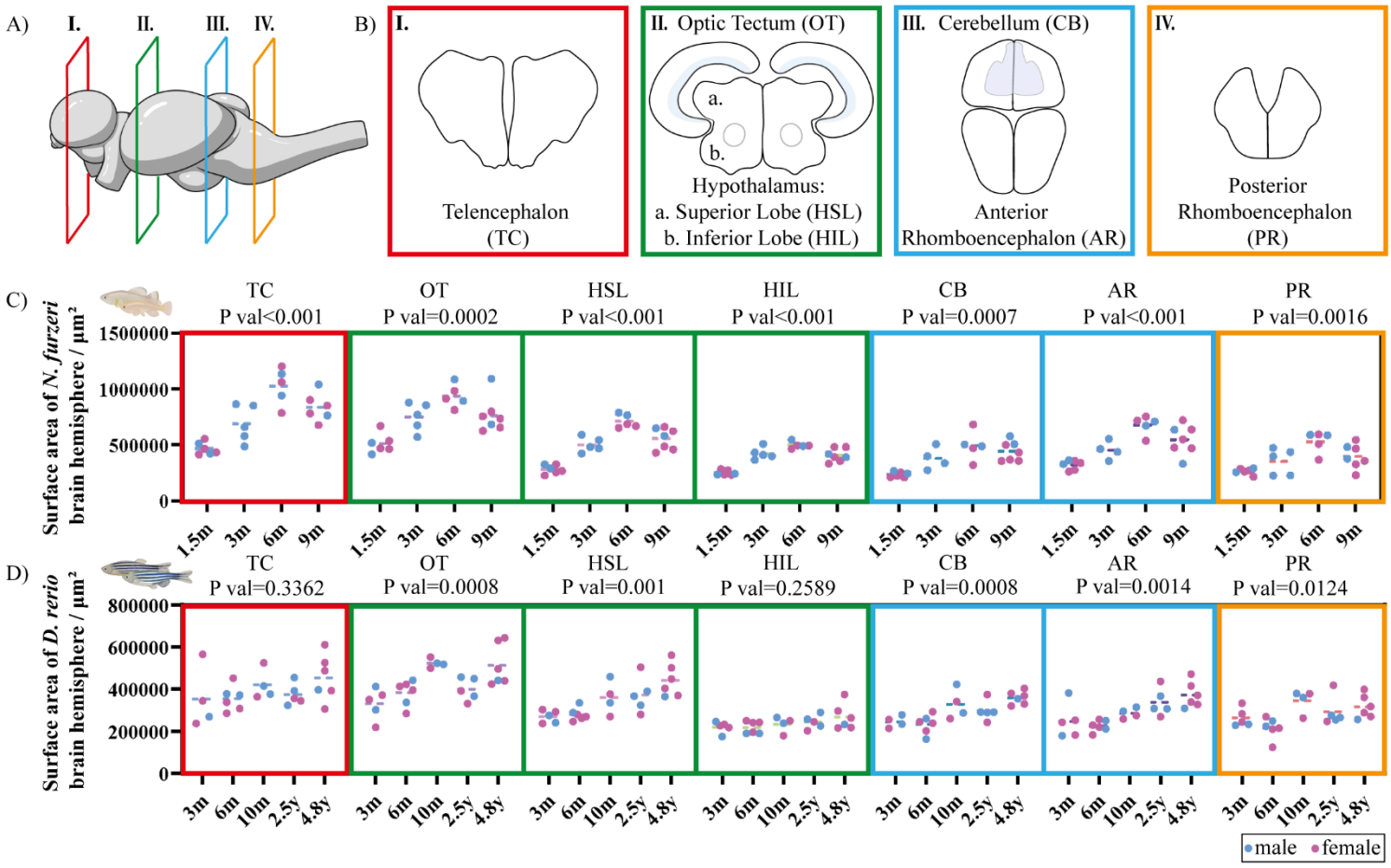

Figure 4. Age-dependent changes in cross-sectional surface area differ between brains of turquoise killifish and zebrafish (A, B) Schematic representation of turquoise killifish brain divided by four major cutting planes into seven different brain regions referred to throughout the thesis. **(C)** Brain hemisphere sizes of region of interest across different time points in turquoise killifish. The ordinary one-way ANOVA analysis of separate brain regions in turquoise killifish shows significant difference within all brain regions (P values indicated above the graphs). **(D)** Brain hemisphere sizes of regions of interest across different time points in zebrafish. The ordinary one-way ANOVA test shows significant difference in the OT, HSL, CB, AR and PR (P values indicated above the graphs). Each dot represents a single brain, displaying the average between values acquired from between 1 and 3 brain sections per brain. The size was measured based on the brain sections used for the IHC. The abbreviations in (C) and (D) correspond to the brain regions indicated in (B).

3.1.2. Age-dependent changes in the astrogliosis and neuronal density in the brain tissue of turquoise killifish and zebrafish

As part of the first objective to compare the brain degeneration in turquoise killifish and zebrafish, I questioned whether there are any changes in the levels of astrogliosis and neuronal density, two important hallmarks of AD-like pathology. To measure the astrogliosis across different time points and brain regions, I utilised IHC and Anti-GFAP antibody to stain mature astrocytes. To detect differentiated neuronal cells and estimate neuronal density in the aging brain, I performed IHC on the brain cross-sections using the Anti-NeuN antibody which detects most types of neuronal nuclei. Due to differences in epitopes in neuronal nuclei, I used different Anti-NeuN antibodies to stain the tissue of turquoise killifish and zebrafish. Stained cross-sections were imaged, and I quantified the percentages of the cross-sectional surface area positive for GFAP and NeuN signal.

For GFAP and NeuN stainings, I analysed seven different brain regions across four (for turquoise killifish) and five (for zebrafish) time points. To be precise, I first focused on all brain regions of 1.5-month-old and 6-month-old brains in turquoise killifish and 3-month-old and 2.5-years-old brains in zebrafish. The 1.5-month and 3-month-old time points entail young, recently fertile fish. The 6-month and 2.5-year-old fish entail adult fish in the stage of life corresponding to the median life span of a given species. I then looked at average values and briefly discussed all brain regions across all time points.

3.1.2.1. GFAP positive signal in the telencephalon

In the TC of turquoise killifish (Supplementary Figure 2A), the percentage of cross-sectional surface area positive for a GFAP signal increases from around 3% in young to almost double the amount in adult fish (Supplementary Figure 2B). Most of the positive signal localises in the ventral middle part of the TC hemisphere, with the rest of the signal dispersing from the middle of the hemisphere (Supplementary Figure 2D-E). The cross-sectional surface area positive for GFAP signal in the TC of zebrafish is more variable in 3-month-old fish compared to 6-month-old fish, with average value decreasing with age (Supplementary Figure 2F). The TC of zebrafish brain tissue shows similar pattern of the positive signal dispersion, both in young and adult fish (Supplementary Figure 2G, I).

3.1.2.2. NeuN positive signal in the telencephalon

The aging TC of turquoise killifish displays a decrease in the neuronal density, calculated as the percentage of cross-sectional surface area positive for NeuN signal (Supplementary Figure 2C). To test the difference between 1.5-months and 6-months old fish, I performed a non-parametric Mann-Whitney test, which supports the results as being significant. It is important to note that there is an increase in the size of the TC between these two time points (Figure 4C). The TC of 3-month and 2.5-year-old zebrafish does not show differences in the cross-sectional surface area positive for NeuN signal between two timepoints (Supplementary Figure 2H), which was supported by the performed Mann-Whitney test, with the brain size remaining roughly the same in the aging brain (Supplementary Figure 2G, I).

3.1.2.3. GFAP positive signal in the optic tectum

From the first look at the OT (Supplementary Figure 3A) stained with DAPI (staining cell nuclei), the OT can be easily divided into two regions – one region rich in cell nuclei surrounding the hypothalamus and the rest of the optic tectum with localised cell bodies. In general, luminal surface area between the OT and the HSL, which can be seen as a hole in the tissue, is larger in the brains of turquoise killifish compared to the brain of zebrafish (Supplementary Figure 3D-E, G).

In the OT of turquoise killifish, the cross-sectional surface area covered with GFAP positive signal increases four-fold on average, from around 2 % to more than 8 % between 1.5-month-old and 6-month-old fish. I questioned the significance of this results using a non-parametric Mann-Whitney test. The test supports the results indicating significant age-dependent astrogliosis in the OT (Supplementary Figure 3B). GFAP positive signal is mainly localised in the outer areas of the brain region, with positive signal being detected in the area surrounding the hypothalamus in both the young and adult turquoise killifish brain (Supplementary Figure 3D-E). In the OT of zebrafish, the GFAP positive signal is stable over time, with 1-2 % of cross-sectional surface area covered in both 3-month and 2.5-year-old fish (Supplementary Figure 3F). The detectable signal is localised in the outer parts of the OT, without prominent signal localising around neighbouring hypothalamus regions (Supplementary Figure 3G).

3.1.2.4. NeuN positive signal in the optic tectum

In the OT of turquoise killifish, I observed a decrease in the cross-sectional surface area positive for NeuN signal between 1.5-month and 6-month-old fish (Supplementary Figure 3C). I tested the difference between these two time points using a non-parametric Mann-Whitney test, which supported the results, indicating a significant decrease in NeuN positive signal and a decrease in the neuronal density. In the OT, NeuN positive signal is mainly localised in the nuclear zone surrounding the hypothalamus. The nuclear zone appears to cover a larger cross-sectional surface area of the OT in young brains compared to older brains (Supplementary Figure 3D-E), although this difference was not quantified. As for zebrafish, there is no significant difference between young 3-month-old and adult 2.5-year-old individuals (Supplementary Figure 3H).

3.1.2.5. GFAP positive signal in the hypothalamus

Considering that the hypothalamus forms one of the biggest brain regions, I divided this brain region into the hypothalamus superior (HSL) and inferior lobe (HIL) (Supplementary Figure 4A). In the brain of turquoise killifish, both lobes show an increase in GFAP positive signal with age, indicating age-dependent astrogliosis. However, many mature astrocytes localised in the HSL, especially in the more dorsal part of the brain closer to the CB (Supplementary Figure 4F-G). On average, the signal increases two-fold (from 6 % to almost 12 %) in the HSL and three-fold (from 0.5 % to 1.5 %) in the HIL of the 1.5-months and 6-months old fish (Supplementary Figure 4B-C).

The hypothalamus of zebrafish shows little to no change in the percentage of cross-sectional surface area positive for GFAP signal, in both the HSL and HIL (Supplementary Figure 5A-B). Mature astrocytes are predominantly localised in the area where the right and left HSL hemisphere come into contact (Supplementary Figure 5E).

3.1.2.6. NeuN positive signal in the hypothalamus

In the brain of turquoise killifish, the HSL does not show a significant decrease in the cross-sectional surface area positive for NeuN signal when compared between 1.5-month and 6-month-old fish (Supplementary Figure 4D). On the other hand, the HIL shows a significant decrease from an average of 12 % of cross-sectional surface area covered in 1.5-month to around 6 % in 6-month-old brain (Supplementary Figure 4E). In zebrafish brain, both the HSL and the HIL do not show significant difference in the cross-sectional surface area positive for NeuN signal between 3-month and 2.5-year-old brain (Supplementary Figure 5C-D). Moreover, based on the histological staining, the signal seems to remain constant between 3-month-old and 2.5-years-old zebrafish (Supplementary Figure 5F).

3.1.2.7. GFAP positive signal in the cerebellum

The CB of both turquoise killifish and zebrafish contains a large amount of cell nuclei, localised in the central and dorsal part of the brain region of both species (Supplementary Figure 6). However, the CB of the two species is morphologically different. The CB of turquoise killifish has a nuclear zone located in the middle of the brain, while the CB of zebrafish has two nuclear zones, one in the middle and one on the outer side of the brain. Moreover, the CB of turquoise killifish is more rounded in shape compared to a slightly elongated CB of zebrafish.

The amount of positive GFAP signal increases over time, indicating proliferation of astrocytes within the aging of both species. On average, in the CB of turquoise killifish the positive signal increases almost three-fold, from 1 % in 1.5-month to almost 3 % in 6-month-old fish (Supplementary Figure 6B).

In the brain of zebrafish, the positive signal increases two-fold, from 1 % in 3-month-old to 2 % in 2.5-year-old fish (Supplementary Figure 6F). However, the shape of the GFAP positive signal differs substantially between the two species. In turquoise killifish, the GFAP expression pattern follows the rest of brain regions, albeit with less prominent filamentous shapes. GFAP positive signal in the 2.5-year-old CB of zebrafish is more rounded and always located in the ventral part of the region, surrounding the nuclear zone, suggesting that astrocytes' bodies are preferably localised in the ventral CB (Supplementary Figure 6G).

3.1.2.8. NeuN positive signal in the cerebellum

I did not observe a significant difference in the cross-sectional surface area positive for NeuN signal in the CB of 1.5-month and 6-month-old brains of turquoise killifish (Supplementary Figure 6C). It is important to note that a lot of the NeuN positive signal is localised in the nuclear zone of this region,

which is full of cell nuclei. The separate cell nuclei could only be distinguished in the borders of the nuclear zone. Therefore, the whole nuclear zone was quantified as one big and inseparable cross-sectional surface area.

As for the CB in zebrafish, I was not able to quantify the cross-sectional surface area positive for NeuN signal. One of the reasons is that the antibody used for the brain tissue of turquoise killifish did not prove to be as efficient for the zebrafish' brain tissue. Moreover, after I switched to a different NeuN antibody, the new antibody showed unspecific binding to a vascular tissue in the brain (Supplementary Figure 9C).

3.1.2.9. GFAP positive signal in the rhomboencephalon

I divided the rhomboencephalon in the anterior (AR) and posterior (PR) part (Supplementary Figure 7A, Supplementary Figure 8A), both of which show significant increases in the cross-sectional surface area positive for GFAP signal in turquoise killifish but not in zebrafish brain tissue. Between 1.5-month and 6-month-old turquoise killifish, the signal on average increases from less than 6 % to more than 8 % in the AR (Supplementary Figure 7B) and from around 6 % to more than 10 % the PR (Supplementary Figure 8B). In both cases, the GFAP positive signal is predominantly detected between the left and right brain hemisphere and on the outer parts of the brain region, indicating that mature astrocytes localise in these regions, protruding into the middle part of the hemisphere (Supplementary Figure 7D-E, Supplementary Figure 8D-E).

In the rhomboencephalon of zebrafish, the amount of detected GFAP positive signal does not significantly change over time, in both the AR and PR (Supplementary Figure 7F, Supplementary Figure 8F). Considering the regions where the signal localises, the same pattern as in turquoise killifish is followed – more signal can be detected in the outer parts of the observed brain hemisphere (Supplementary Figure 7G, Supplementary Figure 8G).

3.1.2.10. NeuN positive signal in the rhomboencephalon

In the AR of turquoise killifish, no significant difference was observed in the percentage of the cross-sectional surface area covered with NeuN positive between 1.5-month and 6-month-old brain (Supplementary Figure 7C). However, in the PR of turquoise killifish, I observed a significant decrease in the cross-sectional surface area positive for the NeuN signal between 1.5-month and 6-month-old brains (Supplementary Figure 8C). In the rhomboencephalon of zebrafish, I did not observe a significant difference in the cross-sectional surface area positive for the NeuN signal between both 3-month and 2.5-year-old AR and PR regions, but the general trend indicates a slight decrease in neuronal density (Supplementary Figure 7H, Supplementary Figure 8H).

3.1.2.11. General overview

To answer the general question whether turquoise killifish and zebrafish differently express two hallmarks of AD, astrogliosis and loss of neuronal density, I calculated the average values of the cross-sectional surface area covered with the GFAP and NeuN positive signal for the whole brain (Figure 5). I calculated the average values considering average values of all seven brain regions of interest (TC, OT, HSL, HIL, CB, AR and PR). In the representation, I omit all individual brains that miss an average value for one or more brain regions. In the graphs, I plotted the percentage of the whole area covered with the GFAP or NeuN positive signal across four different time points for turquoise killifish and five different time points for zebrafish.

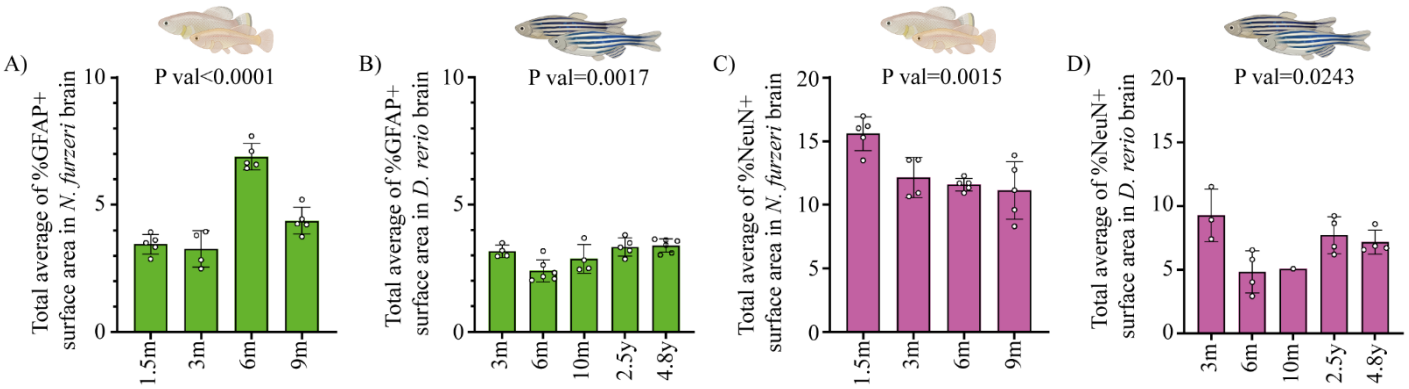

Figure 5. Age dependent astrogliosis and decrease in neuronal density in the whole brain of turquoise killifish and zebrafish (A) Quantification of the percentage of NeuN covered surface area in the brain of 1.5-month, 3-month, 6-month, and 9-months old turquoise killifish. The average values of the cross-sectional surface area covered with the GFAP and NeuN positive signal were calculated for the whole brain, taking average values of all seven brain regions of interest. Each dot represents an individual brain which has at least one value per brain region. Ordinary one-way ANOVA test supports the results with a significant difference between sample groups with P value is indicated above the graph. **(B)** Quantification of the percentage of GFAP covered surface area in the brain of 3-month, 6-month, 10-month, 2.5-year and 4.8-year-old zebrafish. Ordinary one-way ANOVA supports the significant difference between sample groups, with P value indicated above the graph. **(C)** Quantification of the percentage of GFAP covered surface area in the brain of 1.5-month, 3-month, 6-month and 9-month-old turquoise killifish. Ordinary one-way ANOVA supports the results with a significant difference between sample groups, with a P value indicated above the graph. **(D)** Quantification of the percentage of NeuN covered surface area in the brain of 3-month, 6-month, 10-month, 2.5-year and 4.8-year-old zebrafish. Ordinary one-way ANOVA supports the significant difference between the sample groups, with P value indicated above the graph. Mann-Whitney test's P values are indicated above the graphs.

In general, the percentage of the cross-sectional surface area covered with the GFAP positive signal increases between 1.5-months old and 6-months old brain tissue of turquoise killifish (Figure 5A). The biggest expansion of astrocytes seems to happen sometimes between 3 and 6 months of age. Moreover, the cross-sectional surface area covered with the GFAP positive signal decreases between 6-month and 9-month-old brain tissue of turquoise killifish. However, that does not seem to be the case in the brain

tissue of zebrafish (Figure 5B). The zebrafish brain displays only a slight change in the GFAP positive signal, mainly in younger time points. In the later phases of the zebrafish life cycle, astrocytes remain stable in size. The results indicate that turquoise killifish undergo age-dependent astrogliosis, observed as astrocyte expansion in the cross-sections of brain tissue, while zebrafish seem to maintain astrocyte homeostasis during aging.

Overall, the largest cross-sectional surface area covered with the NeuN positive signal is present in 1.5-months old turquoise killifish brain. After 3 months, the percentage of cross-sectional surface area positive for the NeuN signal stabilised and remained the same throughout remaining time points (Figure 5C). Brain regions expand in size until fish reach 6 months of age, while the neuronal nuclei seem to remain constant in size (data not shown). Therefore, it is important to note that all the results show nuclear density of neuronal cells, not the cell count. However, we observed a trend that shows a slight decrease in the NeuN positive signal in the aging turquoise killifish, while the positive signal in zebrafish seemingly fluctuates over the lifespan. Decreases in the NeuN positive signal indicate loss in neuronal density, which could be consistent with the neuronal loss which happens during aging and neurodegenerative diseases.

In summary, I show that turquoise killifish display an increase in the cross-sectional surface area covered with the GFAP positive signal in all seven brain regions over time, indicating an age-dependent astrogliosis encompassing the whole brain. Moreover, data on the brain tissue of turquoise killifish shows a slight decrease in NeuN positive signal over different time points, indicating loss in neuronal density associated with aging. On the contrary, zebrafish tissue does not display a strong increase in the GFAP positive signal nor a decrease in the NeuN positive signal.

3.2. Age-dependent accumulation of $A\beta_{pE11-42}$ in the brain of turquoise killifish

3.2.1. Aβ sequence alignment

To address whether turquoise killifish would form a good model for natural amyloidosis, I first assessed the level of conservation of the APP between different species. I first aligned all splice variant sequences of APP in mammalian and APPA and APPB in fish (Figure 6). Therefore, I considered human (*Homo sapiens*) and mouse (*Mus musculus*) protein sequences as well as turquoise killifish and zebrafish protein sequences. In total, I aligned all known isoforms of the APP protein, including 10 splice variants of protein APP in human, 10 variants of APPA and 9 of APPB in turquoise killifish, 4 variants of APPA and 5 variants of protein APPB in zebrafish, as well as 6 variants of protein APP in mouse (Figure 6B).

A major part of the membrane-bound APP is localized in the extracellular space, with the 42-Amyloid-β peptide mostly located inside of the cell membrane, closer to the C-terminus (Figure 6A). The human APP consists of 770 amino acids (data not shown), while other species have slightly shorter protein sequences. All four species show a certain degree of similarity in the amino acid sequence, with larger mismatches approximately between positions 220 and 300 for turquoise killifish and zebrafish, as well

as right before amyloid-β sequence, between positions 640 and 710 (data not shown). Two enzymes cut the APP protein to form the 42-Amyloid-β, including the β-secretase cutting on the N-terminus of the peptide and the γ-secretase cutting on the C-terminus of the Aβ (Figure 6B). The β-secretase cutting sites in turquoise killifish and zebrafish (M-E for APPA and APPB in turquoise killifish and APPA in zebrafish, L-D for APPB in zebrafish) differ from the cutting site in humans and mice (M-D). The γ-secretase cutting sites are preserved in all four species.

In more detail, I focused on the $A\beta_{42}$ peptide and specific binding site of the Anti-$A\beta_{pE11-42}$ antibody. The Anti-$A\beta_{pE11-42}$ antibody binds the 6 amino acid sequence (E-V-H-H-Q-K) on the 11 amino acids truncated N-terminus of the human $A\beta_{42}$ peptide sequence (Figure 6B). I observed that all 6 amino acids in the antibody binding site in the APPA of turquoise killifish are the same as in the human sequence. Moreover, the APPB of turquoise killifish shares 4 out of 6 amino acids in the binding sequence with the human sequence (E-V-Y-H-E-K). In the APPB of turquoise killifish, second histidine (H) in the original sequence is replaced by the amino acid tyrosine (Y), while glutamine (Q) was replaced by glutamate (E).

The only difference between the mouse and human $A\beta_{42}$ peptide sequence is in three amino acids, including the position 5 (arginine (R-5) in human and glycine (G-5) in mice), the position 10 (tyrosine (Y-10) in human and lysine (K-10) in mice) and the position 13 (histidine (H-13) in human and R-13 in mice). The human and turquoise killifish share the three amino acids in the $A\beta_{42}$ peptide sequence of APPA, while APPB of turquoise killifish and zebrafish share R-5 and Y-10 but not H-13. The peptide sequence of turquoise killifish contains H-13 instead of Y-13, while zebrafish shares R-13 with mouse peptide sequence. In zebrafish, the APPA only shares R-5 with the human sequence, misses the Y-10 and shares Y-13 with turquoise killifish. This arrangement suggest that sequence-intrinsic differences might influence the level of amyloidosis in AD-like pathology.

Moreover, I observed that both the $A\beta_{42}$ peptide and the antibody binding sequence in zebrafish APPA and APPB peptides are quite different compared to the human peptide sequence (Figure 6B). In the APPA of zebrafish, the antibody binding sequence (E-V-Y-H-Q-K) resembles the human sequence. However, the APPB is almost completely different, with only one shared valine (V) in the right place and one misplaced lysine (K).

In summary, the differences between human and turquoise killifish $A\beta_{42}$ peptide exist, but the sequence crucial for the Anti-$A\beta_{pE11-42}$ antibody recognition is conserved in the APPA and partially conserved in the APPB. Moreover, certain differences present between the human and mouse $A\beta_{42}$ peptide are not present between human and turquoise killifish. In zebrafish, the peptide sequence, especially the Anti-$A\beta_{pE11-42}$ antibody binding site, is less conserved.

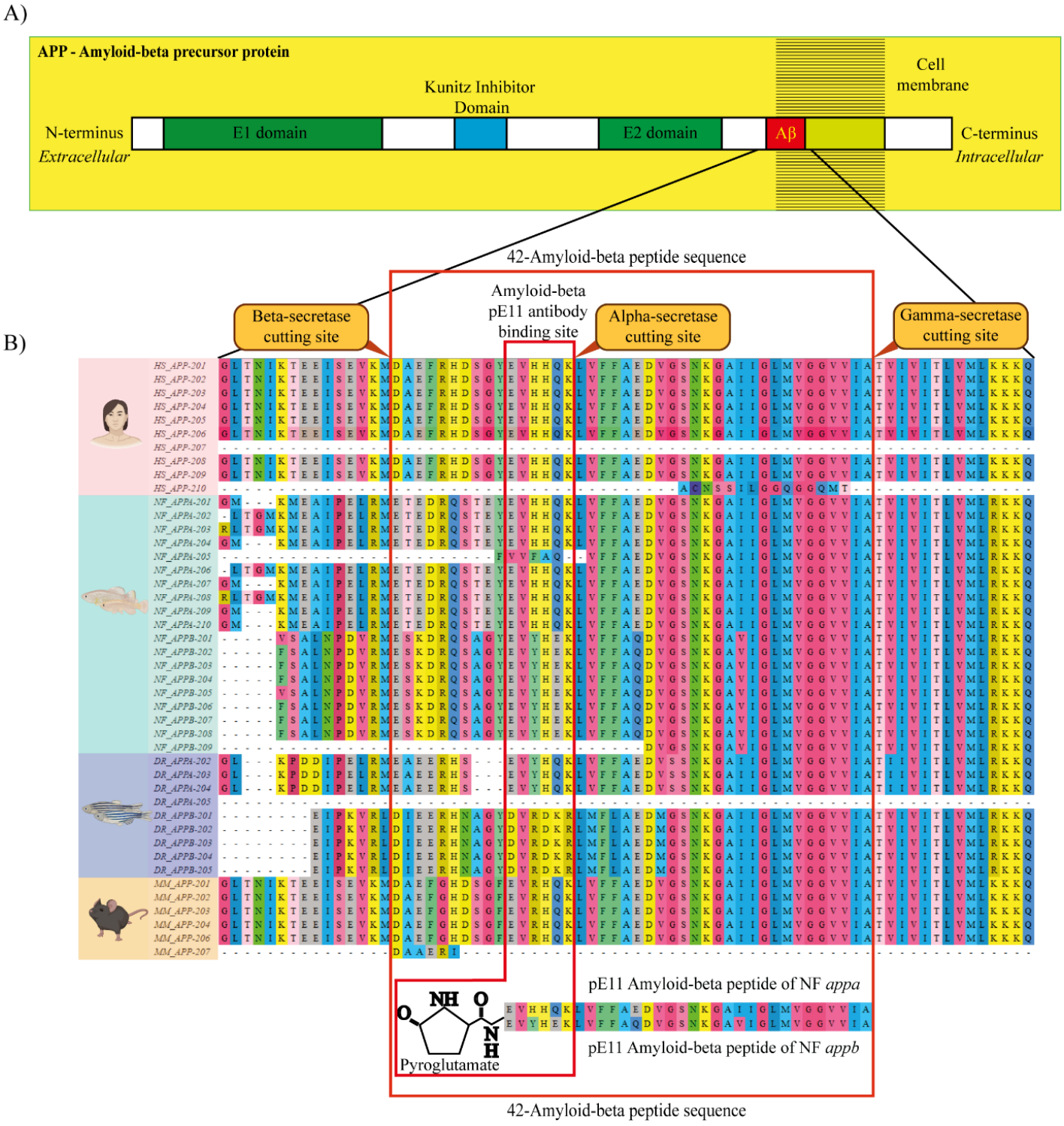

Figure 6. Alignment of protein sequences of Amyloid-beta Precursore Protein (APP) across species shows substantial sequence conservation of the Aβ$_{42}$ domain. A) Schematic representation of APP protein. **B)** Protein alignment of Aβ$_{42}$ peptides (outer red squared box). Each protein splice variant is assigned a specific ID, with the abbreviation of the species, gene and a number from the Ensembl database. Pyroglutamated version of N-terminus truncated Aβ is shown in the bottom of the panel. Aβ$_{pE11-42}$ antibody binds six amino acids of truncated and pyroglutamated version of Aβ (inner red squared box). Cutting sites of Alpha-, Beta-, and Gamma-secretases are indicated with arrows and orange boxes.

3.2.2. Age-dependent accumulation of $A\beta_{pE11-42}$ in the brain of turquoise killifish

The second objective of this study was to determine whether aging turquoise killifish accumulate $A\beta_{pE11-42}$ in the brain. To investigate the accumulation of Aβ in the brain of turquoise killifish, I performed the IHC analysis of the brain cross-sections using the Anti-$A\beta_{pE11-42}$ antibody, which binds to a modified variant of the $A\beta_{42}$ peptide. The antibody is verified to bind to a version of the $A\beta_{42}$ peptide with 11 amino acids missing on its modified N-terminus, carrying pyroglutamate instead of glutamate. $A\beta_{pE11-42}$ is a more toxic variant of the Aβ, and less susceptible to the enzymatic degradation and protein clearance. $A\beta_{pE11-42}$ can be detected in more advanced late-onset stages of AD. The highly specific Anti-$A\beta_{pE11-42}$ antibody enables the detection of the truncated $A\beta_{pE11-42}$ peptide and excludes the full-length APP. As shown in the previous section, the binding site of the Anti-$A\beta_{pE11-42}$ antibody is completely preserved in the APPA of turquoise killifish, while the APPB shows two out of six amino acid substitutions. Therefore, turquoise killifish make for a good target to study the accumulation of $A\beta_{pE11-42}$ during aging.

The stained cross-sections were imaged, and the cross-sectional surface area quantified for the positive $A\beta_{pE11-42}$ signal. The positive signal in each hemisphere of a brain region of interest is presented as a percentage of cross-sectional surface area positive for the $A\beta_{pE11-42}$ signal. I tested the Anti-$A\beta_{pE11-42}$ antibody on both turquoise killifish and zebrafish brain tissue. The staining showed a partially positive $A\beta_{pE11-42}$ signal in zebrafish brain tissue but the intensity of the signal was quite low (data not shown). In the preliminary stages of this study, I quantified the $A\beta_{pE11-42}$ positive signal in zebrafish and the results implied that the percentage of cross-sectional surface area positive for the $A\beta_{pE11-42}$ signal remained stable throughout zebrafish lifespan. However, due to the lack of conservation of the epitope which could explain low intensity of the observed signal, I decided to not follow up on this type of staining in zebrafish. Since the modified $A\beta_{pE11-42}$ peptide is present in pathological AD (in phase 4 and phase 5 of the disease in patiens) and less in normal brain aging, I observed a proxy pathology in turquoise killifish which resembles later stages of human AD.

As I did for GFAP and NeuN, I analysed four different time points and seven different brain regions in the brain of turquoise killifish. In more detail, I first present the results in 1.5-month-old and 6-month-old fish. I took 1.5-month-old as a representation of young fish that had recently become fertile and 6-month-old fish as an adult fish within its median life span.

In stained cross-sections of the turquoise killifish brain, I observed several different staining patterns (Figure 7). The most common stained structures are described as broad and elongated intracellular $A\beta_{pE11-42}$ structures (approximately 5 μm in width and 12 μm in length) surrounding the nuclei (Figure 7A), rounded intracellular $A\beta_{pE11-42}$ structures (approximately 15-20 μm in diameter) surrounding the nuclei (Figure 7B) and long filaments of $A\beta_{pE11-42}$, likely representing extracellular filaments (Figure 7C). Rounded structures are surrounding the cell nuclei. Therefore, I presume the signal localises intracellularly. Less frequently I also observed narrow and long structures (approximately 4 μm in width and 12 μm in length) bright in intensity, surrounding and overlapping with the cell nuclei (Figure 7D), the blood vessels represented as clumps of cells (Figure 7E), and very rare structures (approximately 40 μm in width and 50 μm in length) surrounding the large nuclei (Figure 7F).

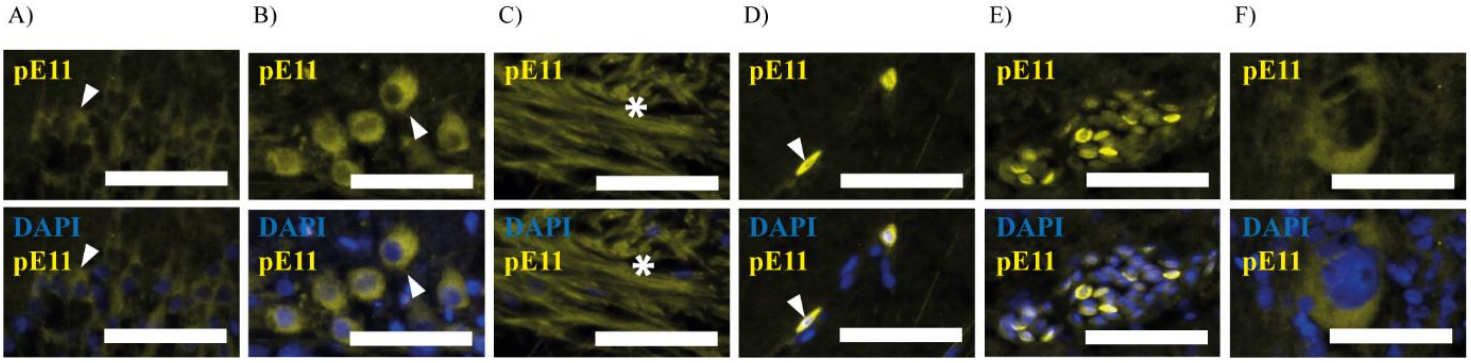

Figure 7. $A\beta_{pE11-42}$ positive structures detected in the brain of turquoise killifish. A) Broad and elongated intracellular $A\beta_{pE11-42}$ structures (approximately 5μm in width and 12μm in length) surrounding the nuclei. **B)** Rounded intracellular $A\beta_{pE11-42}$ structures (approximately 15-20μm in diameter) surrounding the nuclei. **C)** Long filaments of $A\beta_{pE11-42}$, cellular localization unknown **D)** Narrow and long structures (approximately 4μm in width and 12μm in length) bright in intensity, surrounding and overlapping with cell nuclei **E)** Blood vessels represented as clumps of cells. **F)** Very rare structures (approximately 40 μm in width and 50μm in length) surrounding large nuclei. The white arrowheads indicate examples of potential intracellular signal, while asterisk indicates potential extracellular filamentous signal. Both will be used to mark structures in later figures. The scale bar represents 50μm.

4.2.2.1. Telencephalon

I compared the TC of 1.5-month and 6-month-old turquoise killifish in more detail (Figure 8). The cross-sectional surface area covered by $A\beta_{pE11-42}$ positive signal increases between 1.5-month to 6-month-old hemispheres of the TC (Figure 8B). I questioned whether there is a significant difference between 1.5-month and 6-month-old groups and for that I utilised a non-parametric Mann-Whitney test. The test supports the results with a significant difference between two time points, more precisely with a P value of 0.0004. I observed almost no signal in the young TC (Figure 8C), while the old TC shows accumulation of $A\beta_{pE11-42}$ throughout the whole brain region (Figure 8D, overview).

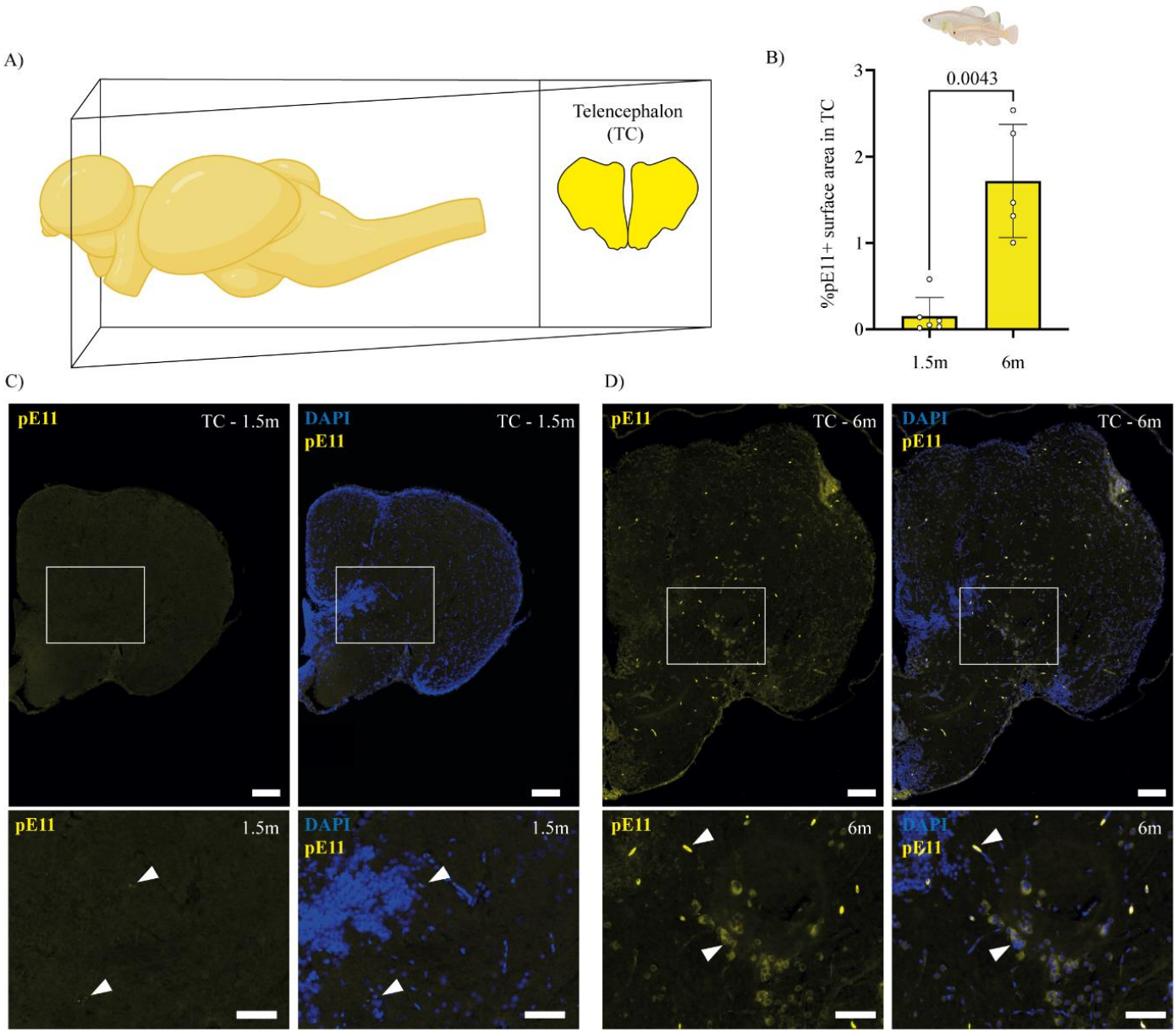

Figure 8. $A\beta_{pE11-42}$ accumulates in the telencephalon of turquoise killifish brain. (A) Schematic representation of the brain region of interest**. (B)** Quantification of the percentage of $A\beta_{pE11-42}$ covered surface area in the TC of 1.5-month-old and 6-month-old brain of turquoise killifish. A non-parametric Mann-Whitney test supports the results indicating a significant upregulation of $A\beta_{pE11-42}$ with age. P value is indicated above the graph. Each dot represents a single brain, displaying the average between values acquired from either 2 or 3 brain sections per brain. **(C, D)** Representative sections of the 1.5-month-old (C) and 6-month-old (D) TC of turquoise killifish stained for $A\beta_{pE11-42}$ and DAPI. The white arrowheads indicate examples of positive signal. The scale bar represents 100µm in the overview (top) and 50µm in the zoom-in (bottom). Mann-Whitney test P value is indicated above the graphs.

4.2.2.2. Optic tectum

The significant increase in the cross-sectional surface area positive for $A\beta_{pE11-42}$ signal was observed between 1.5-month and 6-month-old OT (P value 0.0022, Figure 9B). I could clearly observe a difference based solely on acquired images, with the OT of 1.5-month-old turquoise killifish showing close to no positive signal and the OT of 6-month-old turquoise killifish clearly showing the intense positive signal (Figure 9C-D, overview). In the 6-month-old turquoise killifish, the signal localises primarily in a previously described nuclear zone of the OT, surrounding the hypothalamus (Figure 9D, zoom-in).

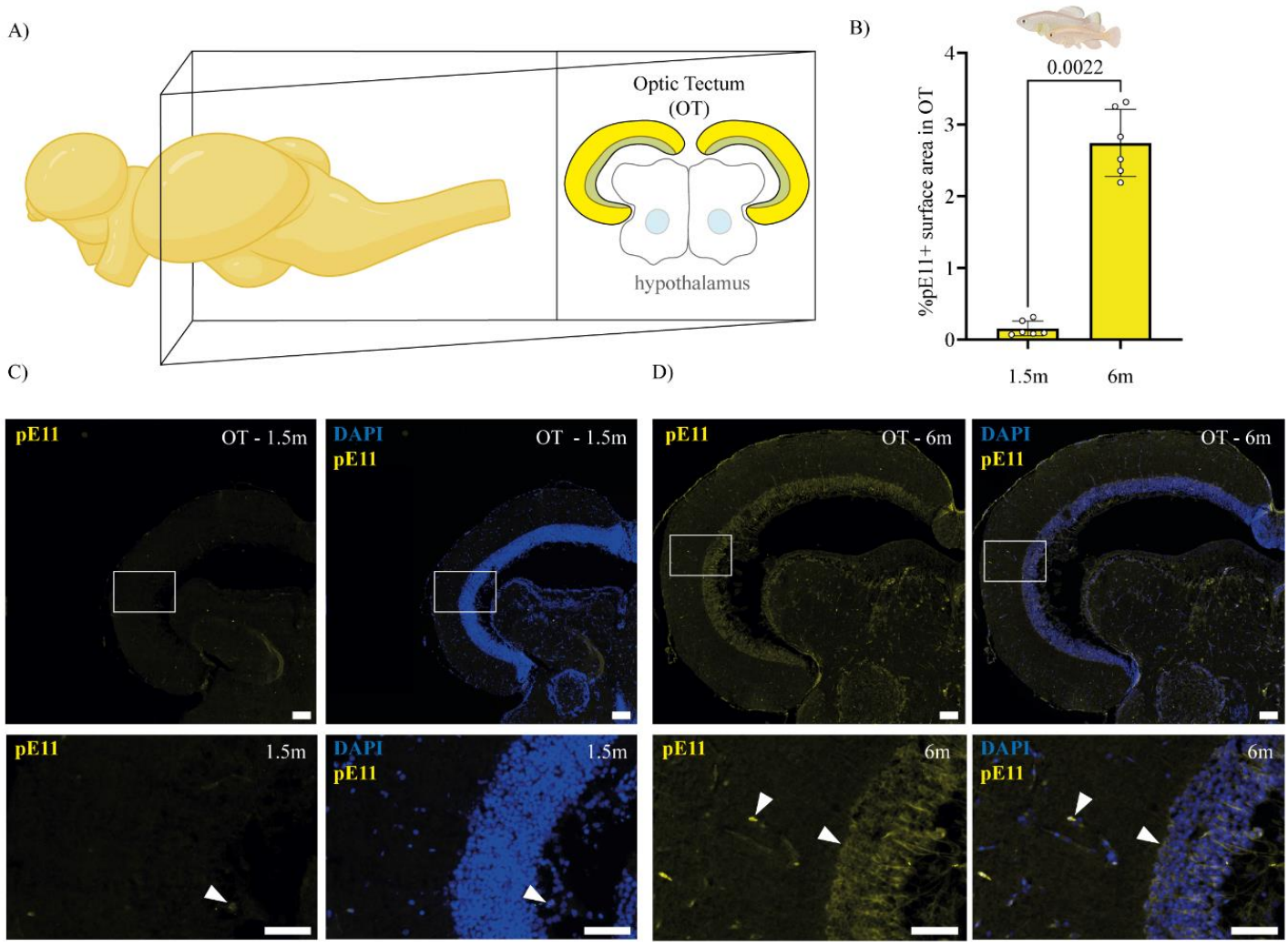

Figure 9. $A\beta_{pE11-42}$ accumulates in the optic tectum of turquoise killifish brain. (A) Schematic representation of the brain region of interest**. (B)** Quantification of the percentage of $A\beta_{pE11-42}$ covered surface area in the OT of 1.5-month-old and 6-month-old brain of turquoise killifish. A non-parametric Mann-Whitney test supports the results indicating a significant upregulation of $A\beta_{pE11-42}$ with age. P value is indicated above the graph. Each dot represents a single brain, displaying the average between values acquired from either 2 or 3 brain sections per brain. **(C, D)** Representative sections of the 1.5-month-old (C) and 6-month-old (D) OT of turquoise killifish stained for $A\beta_{pE11-42}$ and DAPI. The white arrowheads indicate examples of positive signal. The scale bar represents 100µm in the overview (top) and 50µm in the zoom-in (bottom). Mann-Whitney test P value *is* indicated above the graphs.

4.2.2.3. Hypothalamus

Different sub-regions of hypothalamus show differences in expression of positive $A\beta_{pE11-42}$ signal (Figure 10). Moreover, in the hypothalamus of 1.5-month-old turquoise killifish, there appears to be very little positive signal, while the hypothalamus of 6-month-old turquoise killifish shows a bright and robust signal (Figure 10D-E, overview). To prove whether the difference is significant, I performed a non-parametric Mann-Whitney test and compared 1.5-month-old and 6-month-old samples. The test supported the results with a significant increase in both HSL and HIL, with P values of 0.0022 (Figure 10B, C).

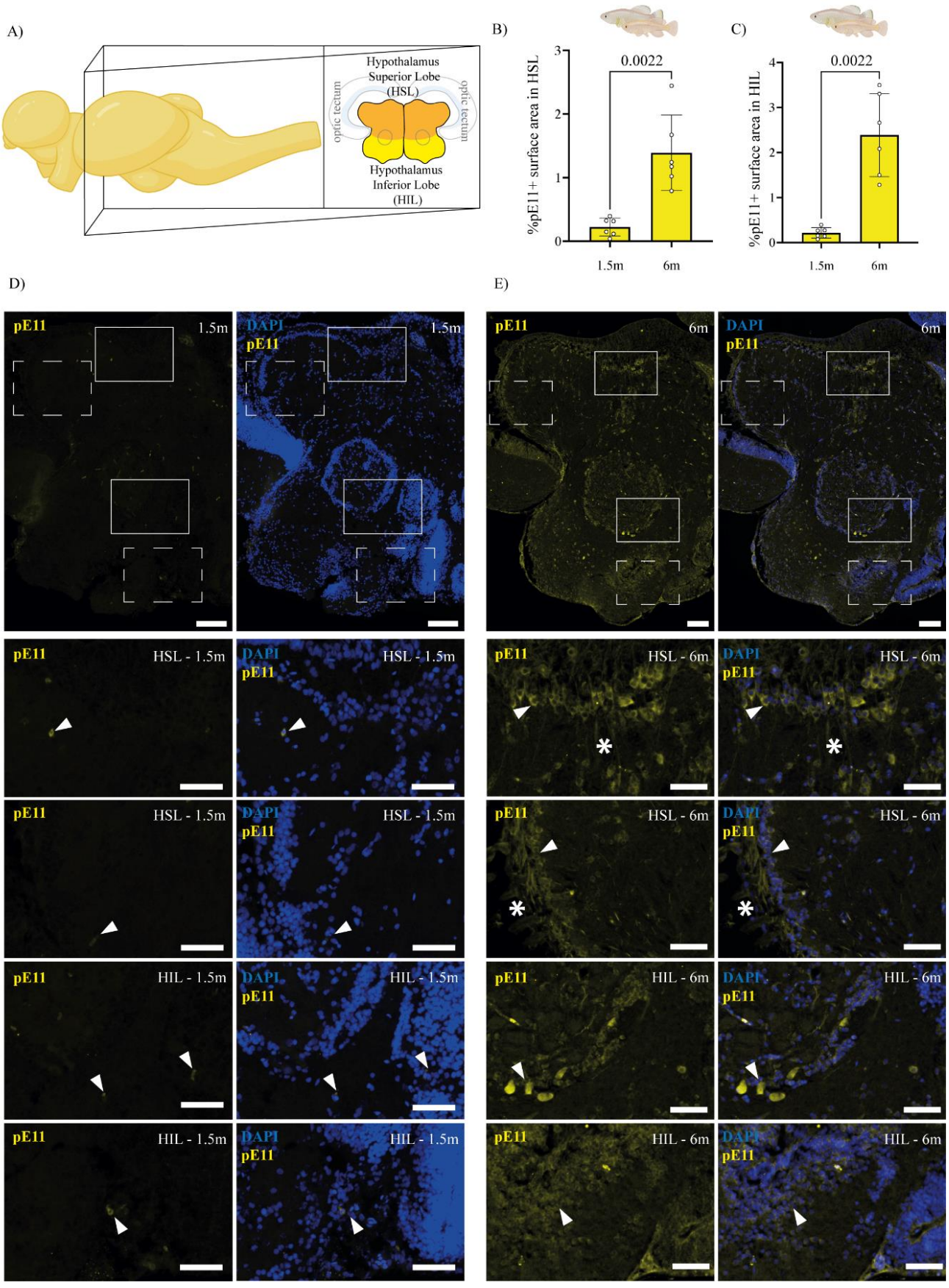
A)
Hypothalamus
Superior Lobe
(HSL)
optic tectum
optic tectum
Hypothalamus
Inferior Lobe
(HIL)
B)
0.0022
%pE11+ surface area in HSL
1.5m
6m
C)
0.0022
%pE11+ surface area in HIL
1.5m
6m
D)
E)
pE11
DAPI
pE11
1.5m
6m
HSL - 1.5m
HSL - 6m
HIL - 1.5m
HIL - 6m

Figure 10. $A\beta_{pE11-42}$ accumulates in the hypothalamus of turquoise killifish brain. (A) Schematic representation of the brain region of interest, divided into the Hypothalamus Superior Lobe (HSL) and the Hypothalamus Inferior Lobe (HIL)**. (B)** Quantification of the percentage of $A\beta_{pE11-42}$ covered surface area in the HSL (left) and the HIL (right) of 1.5-month-old and 6-month-old brain of turquoise killifish. A non-parametric Mann-Whitney test supports the results indicating a significant upregulation of $A\beta_{pE11-42}$ with age. P value calculated is indicated above the graph. Each dot represents a single brain, displaying the average between values acquired from either 2 or 3 brain sections per brain. **(C, D)** Representative sections of the 1.5-month-old (C) and 6-month-old (D) hypothalamus of turquoise killifish stained for $A\beta_{pE11-42}$ and DAPI. The white arrowheads indicate examples of cellular $A\beta_{pE11-42}$ positive signal. The asterisk indicates examples of filamentous $A\beta_{pE11-42}$ positive signal. The scale bar represents 100µm in the overview (top) and 50µm in the zoom-in (bottom). Mann-Whitney test P value is indicated above the graphs.

4.2.2.4. Cerebellum

Positive $A\beta_{pE11-42}$ signal is primarily localised in the centre of the CB (Figure 11). Measured as a percentage of cross-sectional surface area covered with the $A\beta_{pE11-42}$ positive signal, there is an increase in the accumulation of $A\beta_{pE11-42}$ between 1.5-month-old and 6-month-old CB of turquoise killifish (Figure 11B). I asked whether the difference is significant, and thus performed a non-parametric Mann-Whitney test, which supported the results giving a significant difference between two given time points, (P value of 0.0043). In the CB of 1.5-month-old fish there appears to be almost no $A\beta_{pE11-42}$ positive signal, while the CB of 6-month-old CB displays many staining patterns of a $A\beta_{pE11-42}$ positive signal high in intensity (Figure 11D, overview). The signal appears to aggregate mostly around, but not inside of the nuclear zone (Figure 11D, zoom-in).

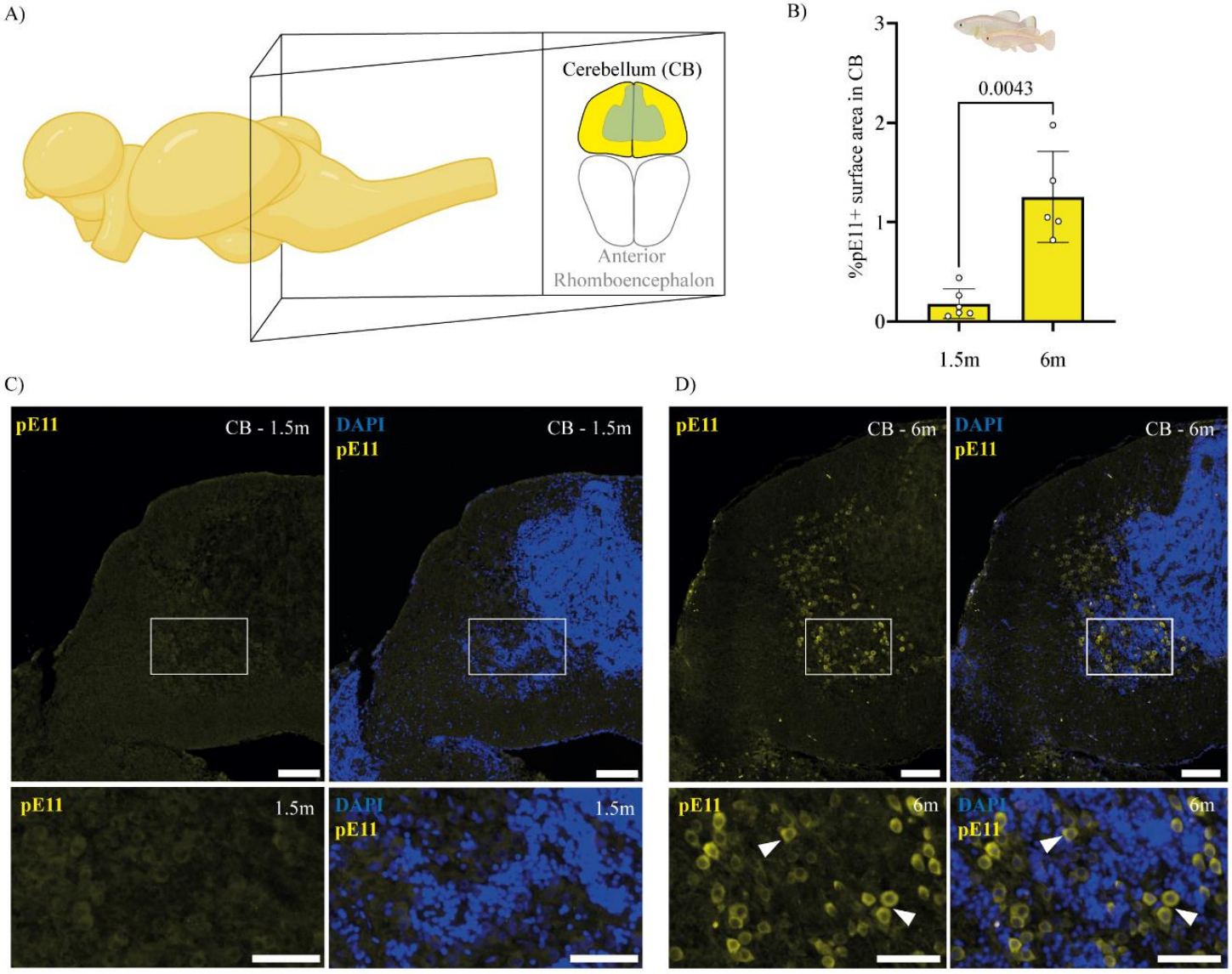

Figure 3. $A\beta_{pE11-42}$ accumulates in the cerebellum of turquoise killifish brain. (A) Schematic representation of the brain region of interest**. (B)** Quantification of the percentage of $A\beta_{pE11-42}$ covered surface area in the CB of 1.5-month-old and 6-month-old brain of turquoise killifish. A non-parametric Mann-Whitney test supports the results indicating a significant upregulation of $A\beta_{pE11-42}$ with age. P value calculated is indicated above the graph. Each dot represents a single brain, displaying the average between values acquired from either 2 or 3 brain sections per brain. **(C, D)** Representative sections of the 1.5-month-old (C) and 6-month-old (D) CB of turquoise killifish stained for $A\beta_{pE11-42}$ and DAPI. The white arrowheads indicate examples of positive signal. The scale bar represents 100µm in the overview (top) and 50µm in the zoom-in (bottom). Mann-Whitney test P value is indicated above the graphs.

4.2.2.5. Rhomboencephalon

Furthermore, I compared 1.5-month and 6-month-old hemispheres of AR and PR. I observed an increase in $A\beta_{pE11-42}$ positive signal between the two time points in both AR (Figure 12B) and PR (Figure 13B). I questioned whether the difference is of significance and performed a non-parametric Mann-Whitney test. The test supported the results with a P value of 0.0053 for the AR and a P value < 0.0001 for the PR. In young 1.5-month-old AR and PR, $A\beta_{pE11-42}$ quantified signal was weak, scarce and hard to distinguish from the background (Figure 12C, Figure 13C). In the 6-month-old AR and PR positive signal was abundant and easily distinguished from the background (Figure 12D, Figure 13D, overviews).

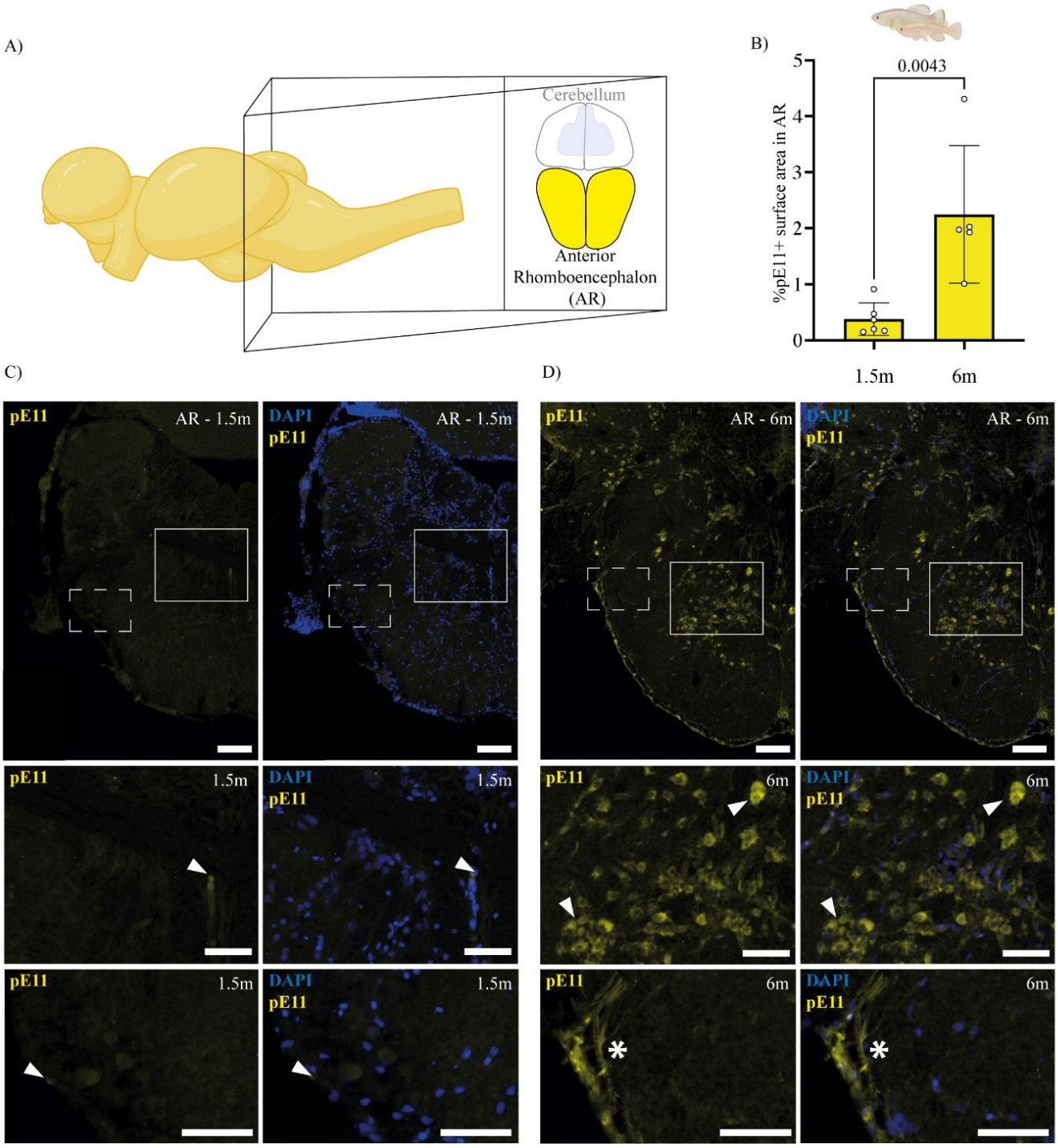

Figure 4. $A\beta_{pE11\text{-}42}$ accumulates in the anterior rhomboencephalon of turquoise killifish brain. (A) Schematic representation of the brain region of interest**. (B)** Quantification of the percentage of $A\beta_{pE11\text{-}42}$ covered surface area in the AR of 1.5-month-old and 6-month-old brain of turquoise killifish. A non-parametric Mann-Whitney test supports the results indicating a significant upregulation of $A\beta_{pE11\text{-}42}$ with age. P value calculated is indicated above the graph. Each dot represents a single brain, displaying the average between values acquired from either 2 or 3 brain sections per brain. **(C, D)** Representative sections of the 1.5-month-old (C) and 6-month-old (D) AR of turquoise killifish stained for $A\beta_{pE11\text{-}42}$ and DAPI. The white arrowheads indicate examples of cellular $A\beta_{pE11\text{-}42}$ positive signal. The asterisk indicates examples of filamentous $A\beta_{pE11\text{-}42}$ positive signal. The scale bar represents 100µm in the overview (top) and 50µm in the zoom-in (bottom). Mann-Whitney test P value is indicated above the graphs.

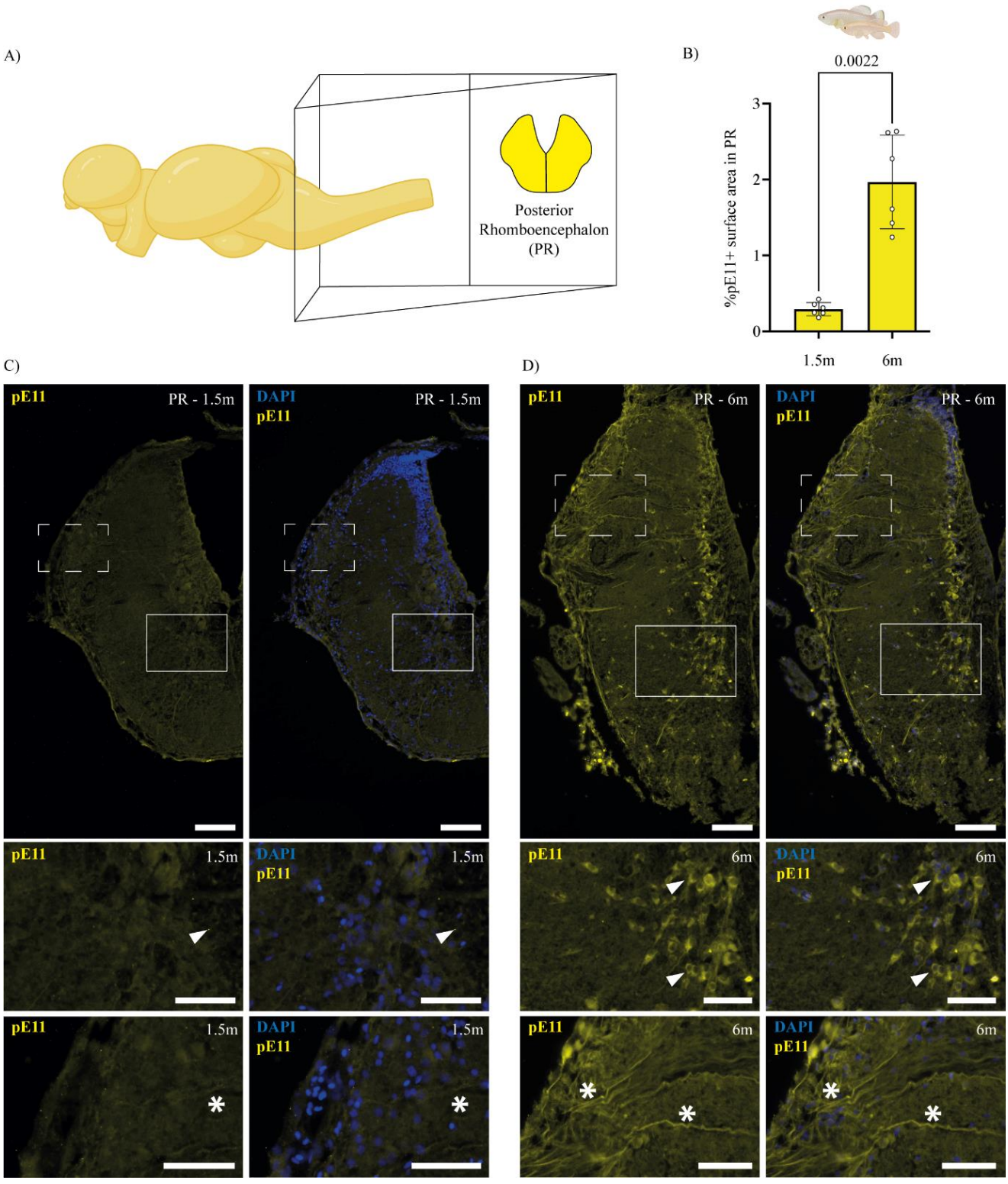

Figure 5. $A\beta_{pE11\text{-}42}$ accumulates in the anterior rhomboencephalon of turquoise killifish brain. (A) Schematic representation of the brain region of interest**. (B)** Quantification of the percentage of $A\beta_{pE11\text{-}42}$ covered surface area in the PR of 1.5-month-old and 6-month-old brain of turquoise killifish. A non-parametric Mann-Whitney test supports the results indicating a significant upregulation of $A\beta_{pE11\text{-}42}$ with age. P value calculated is indicated above the graph. Each dot represents a single brain, displaying the average between values acquired from either 2 or 3 brain sections per brain. **(C, D)** Representative sections of the 1.5-month-old (C) and 6-month-old (D) PR of turquoise killifish stained for $A\beta_{pE11\text{-}42}$ and DAPI. The white arrowheads indicate examples of cellular $A\beta_{pE11\text{-}42}$

positive signal. The asterisk indicates examples of filamentous $A\beta_{pE11-42}$ positive signal. The scale bar represents 100µm in the overview (top) and 50µm in the zoom-in (bottom). Mann-Whitney test P value is indicated above the graphs.

4.2.2.6. General overview

To answer the question whether turquoise killifish display detectable and age-dependent accumulation of $A\beta_{pE11-42}$ on the level of the whole brain, I calculated the average values of the cross-sectional surface area covered with $A\beta_{pE11-42}$ positive signal for the whole brain (Figure 14). I considered only average values of individual brains with all brain regions of interest (TC, OT, HSL, HIL, CB, AR and PR). In the representation, I omitted all individual brains that miss an average value for one or more brain regions. In the graphs, I plotted the percentage of the whole area covered with $A\beta_{pE11-42}$ positive signal across four different time points for turquoise killifish.

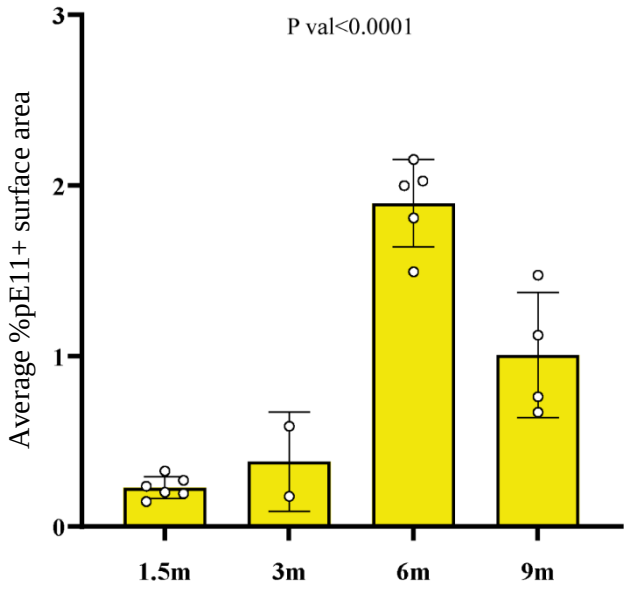

Figure 6. $A\beta_{pE11-42}$ accumulates in the whole brain of turquoise killifish brain. Quantification of the percentage of cross-sectional surface area covered with $A\beta_{pE11-42}$ positive signal in the whole brain of 1.5-month, 3-month, 6-month, and 9-month-old turquoise killifish. The average values of the cross-sectional surface area covered with positive signal were calculated for the whole brain, taking average values of all seven brain regions of interest. Each dot represents an individual brain which has at least one value per brain region. Ordinary one-way ANOVA supports the results with a significant difference between sample groups. P value is indicated above the graph.

The average cross-sectional surface area positive for a $A\beta_{pE11-42}$ signal increases in the aging brain of turquoise killifish (Figure 14). I performed an ordinary one-way ANOVA test on the samples of turquoise killifish and observed a significant difference between four time points (P val <0.0001, R^2 0.9143). I observed the age-dependent accumulation of $A\beta_{pE11-42}$ in the brain of turquoise killifish, substantially increasing between 3 months and 6 months of age, with a slight decrease in fish approaching 9 months.

In general, I observed that $A\beta_{pE11-42}$ positive signal seems to be at a low value in turquoise killifish (less than 0.5 %) in all brain regions until fish reach 3 months (Supplementary Figure 1C). Between 3 months and 6 months, the cross-sectional surface area positive for a $A\beta_{pE11-42}$ signal significantly increases.

The ordinary one-way ANOVA test performed on the TC of 1.5-month, 3-month, 6-month and 9-month-old turquoise killifish supports the significant difference in the results between the samples, with following values for the TC (P value <0.0001, R^2 0.8096), the OT (P value<0.0001, R^2 of 0.8743), HSL (P value of 0.0013, R^2 of 0.5544), HIL (P value of 0.0003, R^2 of 0.6159), CB (P value of 0.0014 and R^2 of 0.6582), AR (P value 0.0033, R^2 0.5889) and PR (P value<0.0001, R^2 0.8057).

In general, in fish up until 3 months of age (corresponding to advanced adulthood), I barely observed any types of staining. However, I observed different staining patterns in the adult 6-month-old fish (Table 7). I observed that the broad and elongated structures are more common in the anterior parts of the brain (from the TC to the HIL) and the rounded intracellular structures in the more posterior parts (from the HSL to the PR). The long extracellular filaments are present in the most brain regions, except the CB where they are not detectable. The narrow and long structures bright in intensity seem to be distributed throughout the whole brain.

Table 7. Different $A\beta_{pE11-42}$ staining patterns observed in the 6-month old brain of turquoise killifish. Brain is divided in different regions, including the telencephalon (TC), optic tectum (OT), hypothalamus superior lobe (HSL), hypothalamus inferior lobe (HIL), cerebellum (CB), anterior rhomboencephalon (AR) and posterior rhomboencephalon (PR). The patterns can be characterised as frequently observed patterns (++), observed patterns (+) and no observed patterns (-).

Staining patterns	**TC**	**OT**	**HSL**	**HIL**	**CB**	**AR**	**PR**
Broad and elongated, intracellular	++	++	++	++	-	+	+
Rounded intracellular	+	-	++	++	++	++	++
Long extracellular filaments	+	+	+	+	-	++	++
Narrow and long, bright in intensity	+	+	+	+	+	+	+

The results of this study show age-dependent accumulation of $A\beta_{pE11-42}$ (mature and toxic form of the Aβ peptide, associated with later stages of AD) in all brain regions of the brain in turquoise killifish, with slight variations in signal intensity and type of observed staining pattern. The results show that the turquoise killifish displays an Aβ accumulation pattern similar to that of AD-like pathology in humans.

.

3.3. CRISPR/Cas9-mediated knock-out of *appa* and *appb* to allow studying the role of Aβ in the brain of turquoise killifish

The third objective of my project was to produce an *appa*/*appb* knock-out strain which would help study the role of Aβ in the brain degeneration of turquoise killifish. To reach this objective, I aimed to genetically modify the long-lived wild-type strain of the turquoise killifish – ZMZ1001. I used the CRISPR/Cas9 as a tool for genome editing, which was previously established in turquoise killifish (Harel *et al.*, 2016). I injected 1- or 2-cell-embryos with a reaction mix containing the CRISPR/Cas9 complex and specific sgRNA targeting *appa* and *appb*. Since the teleost fish have two paralogue genes that are homologous to the human APP, there is a possibility that in the absence of one gene product, the other paralogue overexpresses and compensates for the missing product. I used two different sgRNA targeting the same region of interest to increase the chance of successful CRISR/Cas9 targeting because sometimes sgRNAs do not perform well. I chose the exon 2 over exon 1 because in contrast to exon 1, all splice variants of *appa* contain exon 2, hence a mutation in exon 2 will affect all splice-variants and consequent Aβ synthesis. I brought injected embryos until adulthood, genotyped the fish by isolating DNA from scales and identified possible carriers.

In the first case, I injected two sgRNAs that target exon 2 of *appa* (Figure 15A) into 1- or 2-cell stage embryos. Around 5% of injected fish successfully reached adulthood and were genotyped (data not shown). Prior to successful genotyping, I established a protocol suitable for this type of genotyping, which was presented in the Methods section of this study. Since the deletion can be detected on an agarose-gel after gel-electrophoresis, the embryos could be genotyped and analysed (Figure 15B).

I identified potential fish carrying mutations and crossed those fish with the wild-type fish, which I internally call KO_10, KO_12, KO_15, the number corresponding to the number in the fish database. The KO_10, KO_12 and KO_15 represent my F0 generation of injected fish. I collected the F1 embryos (progeny of the F0 and wild-type fish). In the F1, I identified a heterozygous mutant carrier, progeny of the KO_10. The mutant carried 26 base pair deletion in the sequence of exon 2 in the *appa* (Figure 15D). I set up the fish in the breeding tank together with a wild-type partner fish. Their progeny was considered the F2 generation. In total, 13 F2 fish progeny of 26 bp carrier fish were brought to adulthood and genotyped (data not shown). I identified 6 heterozygous fish carrying the same 26 bp mutations (3 males and 3 females), thus I was able to set up 3 breeding tanks. I collected the progeny, which I considered to be the F3 generation. The embryos have potential to be either wild-type, heterozygous mutant, or homozygous mutant (Figure 15C, D, E respectively). Fish are currently housed at The Leibniz Institute on Aging – Fritz Lipmann Institute (FLI) in Jena and will be further used to study the role of Aβ in brain degeneration and developing AD-like pathology in turquoise killifish.

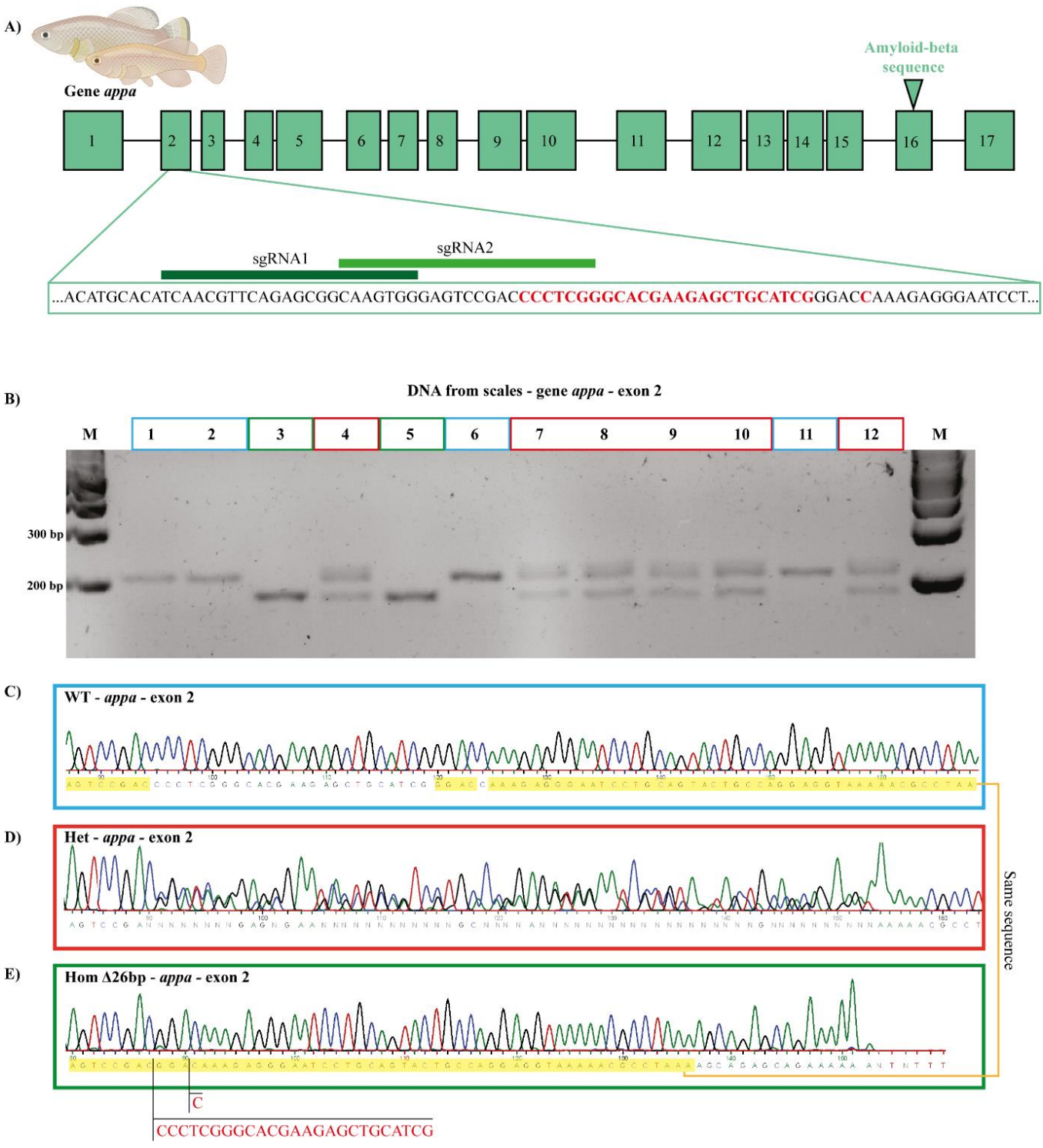

Figure 15. Establishment of an appa knock-out model produced by the CRISPR/Cas9 mediated mutagenesis in turquoise killifish. (A) Target site located in the exon 2 of appa gene of interest, with two sgRNA binding sites used for the CRISPR/Cas9 mediated mutagenesis. The red color is indicating bases that are missing in the mutant fish. Sequence coding for Amyloid-beta is in the Exon 16. **(B)** Genotyping for mutation in appa on agarose gel using DNA isolated from the F2 generation of CRISPR/Cas9 mutated fish. Sizes of gel bands in the ladder (M) neighboring the signal are indicated on both sides of the gel. Box colors in (B) correspond to box colors in (C, D, E), indicating which mutation is present in the sample. **(C)** Homozygous wild type DNA sequence of appa. Presented sequence is part of exon 2 of appa. **(D)** Heterozygous DNA sequence of appa. Presented sequence

contains wild-type DNA and mutated DNA with deletion of 26 base pairs. **(E)** Homozygous mutated DNA sequence of appa. Sequence contains deletion of 26 base pairs compared to the wild-type DNA.

For the *appb*, I injected one sgRNA targeting the exon 3 of the gene of interest (Figure 16A). I did two rounds of injections, and with poor hatching success, I brought 5 injected fish to a sexually mature phase. I set up 5 breeding tanks with separate injected fish paired with wild-type fish, without previous genotyping. I collected the embryos from all five breeding tanks, isolated the DNA and amplified the target region following the established protocol. The PCR products were analyzed on the gel (complete data not shown), and only one parent pair showed messy bands on the gel, indicating potential mutations (Figure 16B). Unfortunately, further breeding and hatching produced fish with only wild-type genotype (data not shown).

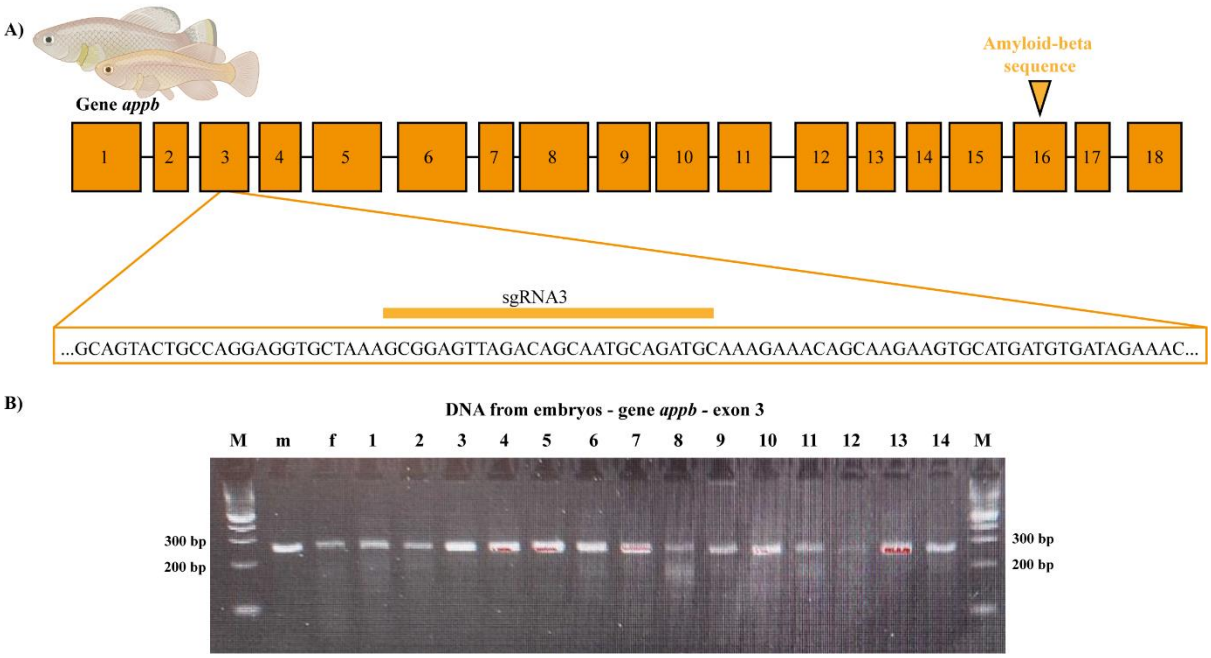

Figure 16. Attempted establishment of an *appb* knock-out model produced by CRISPR/Cas9 mediated mutagenesis in turquoise killifish. (A) Target site located in the exon 3 of *appb* gene of interest, with one sgRNA binding site used for CRISPR/Cas9 mediated mutagenesis. **(B)** Genotyping for mutation in the *appb* on agarose gel using DNA isolated from developing embryos of the F1 CRISPR/Cas9 mutated fish. The red collar on the gel indicates signal which was overexposed upon accruing the image of the gel. Sizes of gel bands in the ladder (M) neighbouring the signal are indicated on both sides of the gel.

Overall, this research produced a valuable *appa* KO killifish model, with a homozygous deletion of 26 base pairs. In future perspective, the antibodies against different variants of the APP will be validated, which will enable further analysis and usage of this model to study the causal role of Aβ in brain degeneration as well as potential AD-like pathology. The homozygous mutant fish should not produce Appa, thus resulting in the phenotype that, in theory, should ameliorate AD-like pathology in the aging brain.

4. DISCUSSION

In my thesis, I aimed to establish African turquoise killifish as a model for studying the role of Aβ during brain degeneration and developing AD-like pathology. My first aim was to analyse the differences between the turquoise killifish, which has been shown to recapitulate several hallmarks of neurodegenerative pathology, and the zebrafish as a control species that does not develop such pathologies.

Upon IHC analysis of brain tissue and estimating the sizes of brain hemisphere of seven different brain regions in both turquoise killifish and zebrafish, I observed different patterns in brain expansion and shrinkage over time. I found that the brain of turquoise killifish expands until fish reach 6 months of age, with subsequent shrinkage up until 9 months of age. Considering that the maximum lifespan in many strains of turquoise killifish is 9 months, the last time point analysed in this study is considered very old. In humans, the brain atrophy, usually analysed via Magnetic Resonance Imaging (MRI), is a valid biomarker for both diagnosis and progression of AD and other neurodegenerative diseases (Frisoni *et al.*, 2010; Pini *et al.*, 2016). Studies in AD patients show an annual decline of 1-4 % in the brain volume, depending on the observed population (Jack *et al.*, 2004; Schott *et al.*, 2005; Sluimer *et al.*, 2008).

In this study, I calculated the cross-sectional surface area of specific brain regions of interest, not the volume, so I cannot directly compare the results with the human brain atrophy. However, I observed that the cross-sectional surface area of the turquoise killifish brain expands rapidly until fish reach 6 months of age, with the cross-sectional surface area doubling in size between 1.5 months and 6 months of age, only to shrink an average of 10-20 % in the brain cross-sectional surface area in the next 3 months. I did not observe such a rapid expansion of brain in zebrafish, nor any signs of shrinkage in old zebrafish individuals. Previous studies observed that the dorsal TC of post-hatching turquoise killifish larvae grow three times faster compared to the TC of zebrafish, probably due to their short lifespan in an ephemeral habitat (Coolen *et al.*, 2020). Brain shrinkage over a lifespan of turquoise killifish could be explained as a consequence of brain damage and brain degenerative processes previously described in this species, such as degeneration of dopamine neurons and accumulation of α-synuclein (Matsui *et al.*, 2019), as well as neuroinflammation and low capability of neurogenesis (Van Houcke *et al.*, 2021). Unlike other teleost fish, the turquoise killifish holds low capacity of neurogenesis later in life, thus any damage in the brain tissue will not be replaced and older fish show scarring of the damaged tissue (Van Houcke *et al.*, 2021). Contrary to the turquoise killifish, the zebrafish brain seems to increase in size throughout its whole life. Therefore, my results indicate that the brain of turquoise killifish reduces in size in the later phases of life, which is the first important hallmark of brain degeneration as well as AD-pathology described in this thesis.

To analyse changes in brain size in more detail, measuring the whole volume of the brain should be performed and the results compared to studies done on AD patients. Several quantitative techniques have been used to assess brain volume in fish (Ullmann *et al.*, 2010). In future perspective, we could measure volume using any of the available methods, with water displacement strategy proven to be simultaneously simple and accurate.

As part of the objective to compare brain degeneration in the turquoise killifish zebrafish, I analysed the cross-sections of brains across four time points in turquoise killifish and five time points in zebrafish. My observations show age-dependent and significant increases in the cross-sectional surface area positive for the Glial Fibrillary Acidic Protein (GFAP) signal. GFAP is the most widely used marker for astrocytes found exclusively in the central nervous system (Eng *et al.*, 2000). Using this marker, I observed an age-dependent increase in active astrogliosis, starting sometime between 3 months and 6 months of age. On the contrary, in zebrafish, the cross-sectional surface area positive for astrogliosis remains stable throughout fish lifespan, with a small difference between 3-month-old and 4.8-year-old individuals. My findings correlate with previous studies showing that short-live strain of turquoise killifish undergo significant astrogliosis during aging (Tozzini *et al.*, 2012). The study by Tozzini *et al*. (2012) showed that no GFAP was detected in the TC and only low levels in the OT of young 5-week-old turquoise killifish. Moreover, they observed elevated levels of GFAP in the OT of 6-month-old fish in comparison to young fish. I observed comparable patterns of the GFAP positive signal in my samples of the TC and the OT. Previous studies focused on more anterior parts of the brain, and this is, to my knowledge, the first attempt to characterise astrogliosis of the whole turquoise killifish brain. The main function of the astrocytes is to support neurons and recycle certain neurotransmitters (Yang and Wang, 2015), with the ratio of astrocytes to neurons being 1:1 (von Bartheld *et al.*, 2016). Besides the markers utilised in this study, one could consider to also look at different hallmarks of brain degeneration, for example changes in microglia, macrophages and oligodendrocytes could be the experimental focal point, helping to further elucidate neuroinflammatory processes in the aging brain of turquoise killifish.

In this study, I analysed the brain tissue of turquoise killifish and zebrafish focusing on the Neuronal Nuceli (NeuN) protein that stains most types of neurons (Gusel'nikova and Korzhevskiy, 2015). By analysing neuronal nuclei, I was able to estimate age-dependent neuronal density. Overall, I observed that the amount of cross-sectional surface area positive for NeuN signal gradually decreases in aging turquoise killifish but remains stable in zebrafish. However, it is important to note that due to reduced neurogenesis and continuous brain growth with age, one possible explanation could be that the reduction in area covered by neurons is caused by expanding brain size. Contrary to this theory, however, I did not observe a change in the percentage of NeuN positive signal between 6 months and 9 months of age, despite observed brain shrinkage between these two time points. The stability of NeuN positive signal could be explained by the proportional shrinkage of neurons, following the shrinkage of the whole brain.

By utilising Fluoro-Jade B staining that marks neuronal degeneration (Schmued and Hopkins, 2000) previous studies observed neurofibrillary degeneration in the TC, OT, CB and brainstem of aging turquoise killifish (Valenzano *et al.*, 2006; Terzibasi *et al.*, 2007). Some studies also show age-dependent impairment of dopaminergic and noradrenergic neurons (Matsui *et al.*, 2019; Vanhunsel *et al.*, 2021).

I encountered several obstacles with NeuN staining. First, the antibody used to analyse the brain tissue of turquoise killifish performed poorly in the brain tissue of zebrafish, so I had to switch to another antibody. The switch caused the second problem, which was unspecific binding of a new antibody to the vascular tissue, which has also been shown in the literature (Härtig *et al.*, 2009) (Supplementary Figure 9D). The problem could be solved by using a different secondary antibody, for instance Alexa647 instead of Alexa555, which shows lower affinity for binding to the vascular tissue.

Initially, my plan was to count DAPI positive signal staining for all cell nuclei and present NeuN results compared to DAPI. More precisely, I wanted to present the results as a percentage of neuronal nuclei in a pool of all cell nuclei. However, that could not be the case because in certain brain regions the NeuN positive signal does not completely overlap with DAPI positive signal. The anti-NeuN antibody seems to stain the area outside of the cell nuclei, both in the brain tissue of turquoise killifish and zebrafish (Supplementary Figure 9A-B). Different NeuN and DAPI staining patterns impose a problem because the ratio of the NeuN and DAPI signal would be high. Showing the ratio of NeuN and DAPI would falsely indicate that neuronal nuclei are prevalent to all other cell nuclei in the brain. Therefore, I presented my results as a percentage of cross-sectional surface area covered by NeuN positive signal, without DAPI positive signal. During the quantification, I noticed that the more posterior parts of the brain (especially the HSL and the whole rhomboencephalon) show more nuclei with an abnormal NeuN positive signal covering a larger area than DAPI positive signal compared to more anterior parts (data not shown). Presuming that abnormal NeuN signal indicates that neuronal cells are damaged in the posterior part would be in correlation to previous studies performed in the turquoise killifish, which show that accumulation of α-synuclein, a protein associated with the development and progression of PD, starts in the more posterior parts of the aging brain (Matsui *et al.*, 2019).

In my thesis, I observed an overlapping NeuN and DAPI positive signal indicating enlarged nuclei with the negative signal forming a hole inside of the cell nuclei (Supplementary Figure 9C). The same pattern has not been observed in cross-sections of the brain tissue in zebrafish (data not shown). I presume that the observed enlarged nuclei represent the nuclei of damaged neurons, which is supported by the evidence showing the same morphology in rats with type-2 diabetes (Hussain *et al.*, 2014). Previously, it has been shown that aggregation of proteins inside of neurons (one of the main hallmarks of AD-like pathology) causes the abnormal morphology of neuronal nuclei (Woulfe, 2007).

To my knowledge, this is the first study focusing on the accumulation of Aβ in the aging brain of turquoise killifish. I showed that accumulation of Aβ increases either gradually or suddenly sometime between 3 and 6 months, then slightly decreases towards 9 months. To exclude all other products of APP and full-length APP itself, I focused on a modified form of $A\beta_{pE11-42}$ peptide, carrying pyroglutamate at its 11 amino acid truncated N-terminus. $A\beta_{pE11-42}$ peptide has been shown to be a more toxic form of $A\beta_{40/42}$ peptide because it is less susceptible to protein degradation. Moreover, $A\beta_{pE11-42}$ peptide is linked to later and more severe AD-like pathology in human patients (Thal *et al.*, 2015).

The accumulation of amyloid-β is one of the hallmarks of AD-like pathology (Thal *et al.*, 2015). Currently available animal models have induced AD-like pathology, require interventions such as genome manipulation and insertion of human transgenes or injections of different Aβ peptides (Götz *et al.*, 2018). Only few other organisms besides humans are known to display spontaneous accumulation of Aβ peptides. One of them is the kokanee salmon (*Oncorhynchus nerka kennerlyi*) where sexually mature and spawning fish show the accumulation of Aβ positive signal in the telencephalon, diencephalon, mesencephalon and rhomboencephalon (Maldonado *et al.*, 2002). The salmon fish that accumulate Aβ in their sexually mature and spawning phase are known to die after they spawn, thus it has been postulated that their rapid aging could be linked to Aβ accumulation in the brain (Maldonado *et al.*, 2002). In the study on salmons, Aβ did not accumulate in certain regions of the hypothalamus and Purkinje cells of the CB. However, the study on salmons did not dive deeper into general cognitive impairment, neuronal loss, neuroinflammation or any other hallmarks of AD. Another study in the chimpanzees (*Pan troglodytes*) showed that Aβ forms brain plaques and depositions in the blood vessels, with higher levels of Aβ depositing in blood vessels than in plaques (Edler *et al.*, 2017). The difference in the inflammatory response linked to the NFTs and Aβ have been observed between humans and chimpanzees (Edler *et al.*, 2018; Munger *et al.*, 2019), potentially explaining why the neuronal loss happens in humans, while chimpanzees show neuronal preservation (Edler *et al.*, 2020).

Interestingly, genes coding for the APP are more conserved in several seemingly important amino acids in the peptide sequence of human and turquoise killifish compared to the mouse and zebrafish peptide sequence. Between the turquoise killifish and human, the APPA shares all three amino acids with the human Aβ peptide sequence (R-5, Y-10 and H-13), while the APPB shares two out of three (Figure 6). Recent studies on the mice expressing humanized Aβ peptide show that changing only 3 amino acids in mouse Aβ sequence to match the human wild-type sequence lead to the cognitive impairment, changes in the synaptic plasticity, neuroinflammation, changes in the brain volume and gene expression but they do not form the Aβ plaques (Baglietto-Vargas *et al.*, 2021). These three amino acids seem to play an important role in developing pathologies induced by the accumulation of Aβ in both mice and humans, so it is possible that they are important for processing and accumulation of Aβ in turquoise killifish, despite other differences in the Aβ peptide sequences compared to the peptide sequence in humans.

Whether the accumulation of Aβ in the brain is a cause or a consequence of cognitive impairment, brain degeneration and AD-like pathology remains unclear. To be able to elucidate this potential causal role of Aβ, I developed a CRISPR/Cas9-mediated mutant of *appa* in the turquoise killifish. I successfully targeted the *appa*, one of the two paralogue genes coding for the APP in the turquoise killifish. My homozygous mutant fish are viable and fertile and present no visible differences with their wild-type siblings. The homozygous fish are still younger than 6 months, but future perspective of this research is to utilise this model to study whether the lack of Aβ alleviates AD-like pathology. However, since the genome of turquoise killifish contains two paralogue genes of human *App*, *appb* still needs to be targeted to get a full knock-out fish. The attempt has been made in the scope of this study, but unfortunately failed due to a low hatching efficiency of the injected fish. I did identify potential founder fish and I was able to grow less than 10 fish to adulthood, but unfortunately all of them had the wild-type genotype (data not shown). Another unfortunate event was that our founder fish stopped breeding early in its developing stage and died shortly after. Therefore, we were not able to collect more embryos and hatch more of the potentially mutated fish. In the future, more rounds of CRISPR/Cas9 injections will be performed in the lab, with the aim to target *appb*.

5. CONCLUSIONS

- I observe that the African turquoise killifish presents hallmarks of AD-like pathology not seen in the zebrafish, including brain atrophy, astrogliosis, changes in neuronal density and accumulation of $A\beta_{pE11-42}$. Meanwhile, the zebrafish seems to possess greater capability to neutralise the processes leading to the brain degeneration.
- I show that the turquoise killifish is a potentially valuable model organism for studying the role of age-dependent accumulation of Aβ peptide in the brain aging, brain degeneration and AD-like pathology.
- I created a new CRISPR/Cas9-mediated *appa* mutant line that could prove to be a powerful platform to study whether Aβ peptide plays a causal role in brain degeneration and developing AD-like pathology.

6. LITERATURE

Aduhelm | ALZFORUM (2022) https://www.alzforum.org/therapeutics/aduhelm (Accessed: 14 July 2022).

Ahmadi-Abhari, S., Guzman-Castillo, M., Bandosz, P., Shipley, M.J., Muniz-Terrera, G., Singh-Manoux, A., Kivimäki, M., Steptoe, A., Capewell, S., O'Flaherty, M., Brunner, E.J. (2017): Temporal trend in dementia incidence since 2002 and projections for prevalence in England and Wales to 2040: modelling study. *BMJ* 9:j2856.

Allard, J.B., Kamei, H., Duan, C. (2013): Inducible transgenic expression in the short-lived fish *Nothobranchius furzeri*: Transgenic turquoise *Nothobranchius furzeri*. *Journal of Fish Biology* 82(5): 1733–1738.

Alzheimer's disease - Symptoms and causes (2022) *Mayo Clinic*. https://www.mayoclinic.org/diseases-conditions/alzheimers-disease/symptoms-causes/syc-20350447 (Accessed: 24 July 2022).

Alzheimer's disease - Treatment (2018) https://www.nhs.uk/conditions/alzheimers-disease/treatment/ (Accessed: 14 July 2022).

Alzheimer's Disease (AD) | DrugBank Online (no date) https://go.drugbank.com/indications/DBCOND0049114 (Accessed: 17 July 2022).

Azam, S., Haque, Md.E., Balakrishnan, R., Kim, I.-S., Choi, D.-K. (2021): The ageing brain: molecular cellular basis of neurodegeneration, *Frontiers in Cell and Developmental Biology* 9.

Azevedo, F.A.C., Carvalho, L.R.B., Grinberg, L.T., Farfel, J.M., Ferretti, R.E.L., Leite, R.E.P., Filho, W.J., Lent, R., Herculano-Houzel, S. (2009): Equal numbers of neuronal and nonneuronal cells make the human brain an isometrically scaled-up primate brain. *The Journal of Comparative Neurology* 513(5): 532–541. Available at: https://doi.org/10.1002/cne.21974.

Baglietto-Vargas, D., Forner, S., Cai, L., Martini, A.C., Trujillo-Estrada, L., Swarup, V., Nguyen, M.M.T., Do Huynh, K., Javonillo, D.I., Tran, K.M., Phan, J., Jiang, S., Kramár, E.A., Nuñez-Diaz, C., Balderrama-Gutierrez, G., Garcia, F., Childs, J., Rodriguez-Ortiz, C.J., Garcia-Leon, J.A., Kitazawa, M., Shahnawaz, M., Matheos, D.P., Ma, X., Da Cunha, C., Walls, K.C., Ager, R.R., Soto, C., Gutierrez, A., Moreno-Gonzalez, I., Mortazavi, A., Tenner, A.J., MacGregor, G.R., Wood, M., Green, K.N., LaFerla, F.M. (2021): Generation of a humanized Aβ expressing mouse demonstrating aspects of Alzheimer's disease-like pathology. *Nature Communications* 12(1): 2421.

Banote, R.K., Chebli, J., Şatır, T.M., Varshney, G.K., Camacho, R., Ledin, J., Burgess, S.M., Abramsson, A., Zetterberg, H. (2020): Amyloid precursor protein-b facilitates cell adhesion during early development in zebrafish. *Scientific Reports* 10(1): 10127.

Bartáková, V., Reichard, M., Janko, K., Polačik, M., Blažek, R., Reichwald, K., Cellerino, A., Bryja, J. (2013): Strong population genetic structuring in an annual fish, *Nothobranchius furzeri*, suggests multiple savannah refugia in southern Mozambique. *BMC Evolutionary Biology* 13(1): 196.

von Bartheld, C.S., Bahney, J., Herculano-Houzel, S. (2016): The search for true numbers of neurons and glial cells in the human brain: A review of 150 years of cell counting: Quantifying neurons and glia in human brain. *Journal of Comparative Neurology* 524(18): 3865–3895.

Baumgart, M., Di Cicco, E., Rossi, G., Cellerino, A., Tozzini, E.T. (2015): Comparison of captive lifespan, age-associated liver neoplasias and age-dependent gene expression between two annual fish species: *Nothobranchius furzeri* and *Nothobranchius korthause*. *Biogerontology* 16(1): 63–69.

Bennett, D.A., Wilson, R.S., Boyle, P.A., Buchman, A.S., Schneider, J.A. (2012): Relation of neuropathology to cognition in persons without cognitive impairment. *Annals of Neurology* 72(4): 599–609.

Bhattarai, P., Thomas, A.K., Zhang, Y., Kizil, C. (2017): The effects of aging on Amyloid-β42-induced neurodegeneration and regeneration in adult zebrafish brain. *Neurogenesis* 4(1): e1322666.

Bronzuoli, M.R., Iacomino, A., Steardo, L. and Scuderi, C. (2016): Targeting neuroinflammation in Alzheimer's disease. *Journal of Inflammation Research* 9: 199–208.

Brookmeyer, R., Abdalla, N., Kawas, C.H., Corrada, M.M. (2018): Forecasting the prevalence of preclinical and clinical Alzheimer's disease in the United States. *Alzheimer's & Dementia*, 14(2): 121–129.

Bryson, H.M. Benfield, P. (1997) Donepezil. *Drugs & Aging*, 10(3): 234–239.

Catchen, J.M., Braasch, I., Postlethwait, J.H. (2011): Conserved synteny and the zebrafish genome. *Methods in Cell Biology*. Elsevier 259–285.

Chen, G., Xu, T., Yan, Y., Zhou, Y., Jiang, Y., Melcher, K., Xu, H.E. (2017): Amyloid beta: structure, biology and structure-based therapeutic development. *Acta Pharmacologica Sinica* 38(9): 1205–1235.

Coolen, M., Labusch, M., Mannioui, A., Bally-Cuif, L. (2020): Mosaic heterochrony in neural progenitors sustains accelerated brain growth and neurogenesis in the juvenile killifish *N. furzeri*. *Current Biology* 30(4): 736-745.e4.

Crews, L., Masliah, E. (2010): Molecular mechanisms of neurodegeneration in Alzheimer's disease. *Human Molecular Genetics* 19(R1): R12–R20.

Cui, R., Willemsen, D., Valenzano, D.R. (2020): *Nothobranchius furzeri* (African Turquoise Killifish). *Trends in Genetics* 36(7): 540–541.

Davis, D.G., Schmitt, F.A., Wekstein, D.R., Markesbery, W.R. (1999): Alzheimer neuropathologic alterations in aged cognitively normal subjects. *Journal of Neuropathology and Experimental Neurology* 58(4): 376–388.

De Sousa, R.A.L. (2022): Reactive gliosis in Alzheimer's disease: a crucial role for cognitive impairment and memory loss. *Metabolic Brain Disease*, 37(4): 851–857.

DeMattos, R.B., Bales, K.R., Cummins, D.J., Dodart, J.-C., Paul, S.M., Holtzman, D.M. (2001): Peripheral anti-Aβ antibody alters CNS and plasma Aβ clearance and decreases brain Aβ burden in a mouse model of Alzheimer's disease. *Proceedings of the National Academy of Sciences* 98(15): 8850–8855.

Dementia (2021) *World Health Organization*. https://www.who.int/news-room/fact-sheets/detail/dementia (Accessed: 17 July 2022).

DePaula-Silva, A.B., Gorbea, C., Doty, D.J., Libbey, J.E., Sanchez, J.M.S., Hanak, T.J., Cazalla, D., Fujinami, R.S. (2019): Differential transcriptional profiles identify microglial- and macrophage-specific gene markers expressed during virus-induced neuroinflammation. *Journal of Neuroinflammation* 16(1): 152.

Deyts, C., Thinakaran, G., Parent, A.T. (2016): APP receptor? To be or not to be. *Trends in Pharmacological Sciences* 37(5): 390–411.

Di Cicco, E., Tozzini, E.T., Rossi, G., Cellerino, A. (2011): The short-lived annual fish *Nothobranchius furzeri* shows a typical teleost aging process reinforced by high incidence of age-dependent neoplasias. *Experimental Gerontology* 46(4): 249–256.

Dodzian, J., Kean, S., Seidel, J., Valenzano, D.R. (2018): A Protocol for Laboratory Housing of Turquoise Killifish (*Nothobranchius furzeri*). *JoVE (Journal of Visualized Experiments)* 134: e57073.

Dong, S., Duan, Y., Hu, Y., Zhao, Z. (2012): Advances in the Pathogenesis of Alzheimer's Disease: a Re-Evaluation of Amyloid Cascade Hypothesis. *Translational Neurodegeneration* 1(1): 18.

Duce, J.A., Tsatsanis, A., Cater, M.A., James, S.A., Robb, E., Wikhe, K., Leong, S.L., Perez, K., Johanssen, T., Greenough, M.A., Cho, H.-H., Galatis, D., Moir, R.D., Masters, C.L., McLean, C., Tanzi, R.E., Cappai, R., Barnham, K.J., Ciccotosto, G.D., Rogers, J.T., Bush, A.I. (2010): Iron-export ferroxidase activity of β-Amyloid precursor protein is inhibited by zinc in Alzheimer's disease. *Cell* 142(6): 857–867.

Eckman, E.A., Reed, D.K., Eckman, C.B. (2001): Degradation of the Alzheimer's Amyloid β peptide by endothelin-converting enzyme. *Journal of Biological Chemistry* 276(27): 24540–24548.

Eckman, E.A., Watson, M., Marlow, L., Sambamurti, K., Eckman, C.B. (2003): Alzheimer's disease β-Amyloid peptide is increased in mice deficient in endothelin-converting enzyme. *Journal of Biological Chemistry* 278(4): 2081–2084.

Edler, M.K., Munger, E.L., Meindl, R.S., Hopkins, W.D., Ely, J.J., Erwin, J.M., Mufson, E.J., Hof, P.R., Sherwood, C.C., Raghanti, M.A. (2020): Neuron loss associated with age but not Alzheimer's disease pathology in the chimpanzee brain. *Philosophical Transactions of the Royal Society B: Biological Sciences*, 375(1811): 20190619.

Edler, M.K., Sherwood, C.C., Meindl, R.S., Hopkins, W.D., Ely, J.J., Erwin, J.M., Mufson, E.J., Hof, P.R., Raghanti, M.A. (2017): Aged chimpanzees exhibit pathologic hallmarks of Alzheimer's disease. *Neurobiology of Aging* 59: 107–120.

Edler, M.K., Sherwood, C.C., Meindl, R.S., Munger, E.L., Hopkins, W.D., Ely, J.J., Erwin, J.M., Perl, D.P., Mufson, E.J., Hof, P.R. and Raghanti, M.A. (2018): Microglia changes associated to Alzheimer's disease pathology in aged chimpanzees. *Journal of Comparative Neurology* 526(18): 2921–2936.

Elobeid, A., Libard, S., Leino, M., Popova, S.N., Alafuzoff, I. (2016): Altered proteins in the aging brain. *Journal of Neuropathology & Experimental Neurology* 75(4): 316–325.

Eng, L.F., Ghirnikar, R.S., Lee, Y.L. (2000): Glial fibrillary acidic protein: GFAP-thirty-one years (1969-2000). *Neurochemical Research* 25(9–10): 1439–1451.

Felice, F.G., Vieira, M.N.N., Saraiva, L.M., Figueroa-Villar, J.D., Garcia-Abreu, J., Liu, R., Chang, L., Klein, W.L., Ferreira, S.T. (2004): Targeting the neurotoxic species in Alzheimer's disease: inhibitors of Aβ oligomerization. *The FASEB Journal* 18(12): 1366–1372.

Fricker, M., Tolkovsky, A.M., Borutaite, V., Coleman, M., Brown, G.C. (2018): Neuronal cell death'. *Physiological Reviews* 98(2): 813–880.

Frisoni, G.B., Fox, N.C., Jack, C.R., Scheltens, P., Thompson, P.M. (2010): The clinical use of structural MRI in Alzheimer disease. *Nature Reviews Neurology* 6(2): 67–77.

Frisoni, G.B., Laakso, M.P., Beltramello, A., Geroldi, C., Bianchetti, A., Soininen, H., Trabucchi, M. (1999): Hippocampal and entorhinal cortex atrophy in frontotemporal dementia and Alzheimer's disease. *Neurology* 52(1): 91–91.

Frozza, R.L., Lourenco, M.V. and De Felice, F.G. (2018): Challenges for Alzheimer's disease therapy: insights from novel mechanisms beyond memory defects. *Frontiers in Neuroscience* 12: 37.

Games, D., Adams, D., Alessandrini, R., Barbour, R., Borthelette, P., Blackwell, C., Carr, T., Clemens, J., Donaldson, T., Gillespie, F., Guido, T., Hagopian, S., Johnson-Wood, K., Khan, K., Lee, M., Leibowitz, P., Lieberburg, I., Little, S., Masliah, E., McConlogue, L., Montoya-Zavala, M., Mucke, L., Paganini, L., Penniman, E., Power, M., Schenk, D., Seubert, P., Snyder, B., Soriano, F., Tan, H., Vitale, J., Wadsworth, S., Wolozin, B., Zhao, J. (1995): Alzheimer-type neuropathology in transgenic mice overexpressing V717F β-amyloid precursor protein. *Nature*, 373(6514): 523–527.

Geerts, H. (2009): Of mice and men: Bridging the translational disconnect in CNS drug discovery. *CNS Drugs* 23(11): 915–926.

Genade, T., Benedetti, M., Terzibasi, E., Roncaglia, P., Valenzano, D.R., Cattaneo, A. and Cellerino, A. (2005): Annual fishes of the genus *Nothobranchius* as a model system for aging research. *Aging Cell* 4(5): 23–233.

Glenner, G.G., Wong, C.W. (1984): Alzheimer's disease: Initial report of the purification and characterization of a novel cerebrovascular amyloid protein. *Biochemical and Biophysical Research Communications* 120(3): 885–890.

Götz, J., Bodea, L.-G., Goedert, M. (2018): Rodent models for Alzheimer disease. *Nature Reviews Neuroscience* 19(10): 583–598.

Gouras, G.K., Tsai, J., Naslund, J., Vincent, B., Edgar, M., Checler, F., Greenfield, J.P., Haroutunian, V., Buxbaum, J.D., Xu, H., Greengard, P., Relkin, N.R. (2000): Intraneuronal Aβ42 accumulation in human brain. *The American Journal of Pathology* 156(1): 15–20.

Gregersen, R., Lambertsen, K., Finsen, B. (2000): Microglia and macrophages are the major source of tumor necrosis factor in permanent middle cerebral artery occlusion in mice. *Journal of Cerebral Blood Flow & Metabolism* 20(1): 53–65.

Grundke-Iqbal, I., Iqbal, K., George, L., Tung, Y.C., Kim, K.S., Wisniewski, H.M. (1989): Amyloid protein and neurofibrillary tangles coexist in the same neuron in Alzheimer disease. *Proceedings of the National Academy of Sciences* 86(8): 2853–2857.

Gusel'nikova, V.V. and Korzhevskiy, D.E. (2015): NeuN as a neuronal nuclear antigen and neuron differentiation marker. *Acta Naturae* 7(2): 42–47.

Haass, C., Selkoe, D.J. (1993): Cellular processing of β-amyloid precursor protein and the genesis of amyloid β-peptide. *Cell* 75(6): 1039–1042.

Hafez, D., Huang, J.Y., Huynh, A.M., Valtierra, S., Rockenstein, E., Bruno, A.M., Lu, B., DesGroseillers, L., Masliah, E., Marr, R.A. (2011): Neprilysin-2 is an important β-Amyloid degrading enzyme. *The American Journal of Pathology* 178(1): 306–312.

Hall, A.M., Roberson, E.D. (2012): Mouse models of Alzheimer's disease. *Brain Research Bulletin* 88(1): 3–12.

Hallmarks of Neurodegeneration (2022) *Cell Signaling Technology*. https://www.cellsignal.com/science-resources/hallmarks-of-ndg (Accessed: 24 July 2022).

Harel, I., Benayoun, B.A., Machado, B., Singh, P.P., Hu, C.-K., Pech, M.F., Valenzano, D.R., Zhang, E., Sharp, S.C., Artandi, S.E., Brunet, A. (2015): A platform for rapid exploration of aging and diseases in a naturally short-lived vertebrate. *Cell* 160(5): 1013–1026.

Harel, I., Valenzano, D.R., Brunet, A. (2016): Efficient genome engineering approaches for the short-lived African turquoise killifish. *Nature Protocols*, 11(10): 2010–2028.

Härtig, W., Reichenbach, A., Voigt, C., Boltze, J., Bulavina, L., Schuhmann, M.U., Seeger, J., Schusser, G.F., Freytag, C., Grosche, J. (2009): Triple fluorescence labelling of neuronal, glial and vascular markers revealing pathological alterations in various animal models. *Journal of Chemical Neuroanatomy* 37(2): 128–138.

Hartmann, N., Englert, C. (2012): A microinjection protocol for the generation of transgenic killifish (Species: *Nothobranchius furzeri*). *Developmental Dynamics* 241(6): 1133–1141.

Hartmann, N., Reichwald, K., Lechel, A., Graf, M., Kirschner, J., Dorn, A., Terzibasi, E., Wellner, J., Platzer, M., Rudolph, K.L., Cellerino, A., Englert, C. (2009): Telomeres shorten while Tert expression increases during ageing of the short-lived fish *Nothobranchius furzeri*. *Mechanisms of Ageing and Development* 130(5): 290–296.

Hartmann, N., Reichwald, K., Wittig, I., Dröse, S., Schmeisser, S., Lück, C., Hahn, C., Graf, M., Gausmann, U., Terzibasi, E., Cellerino, A., Ristow, M., Brandt, U., Platzer, M., Englert, C. (2011): Mitochondrial DNA copy number and function decrease with age in the short-lived fish *Nothobranchius furzeri*: Decline of mitochondrial function in aging fish. *Aging Cell* 10(5): 824–831.

Harvey, R.J. (2003): The prevalence and causes of dementia in people under the age of 65 years. *Journal of Neurology, Neurosurgery & Psychiatry* 74(9): 1206–1209.

Hol, E.M., Pekny, M. (2015): Glial fibrillary acidic protein (GFAP) and the astrocyte intermediate filament system in diseases of the central nervous system. *Current Opinion in Cell Biology* 32: 121–130.

Hou, Y., Dan, X., Babbar, M., Wei, Y., Hasselbalch, S.G., Croteau, D.L., Bohr, V.A. (2019): Ageing as a risk factor for neurodegenerative disease. *Nature Reviews Neurology* 15(10): 565–581.

Hu, C.-K., Brunet, A. (2018): The African turquoise killifish: A research organism to study vertebrate aging and diapause. *Aging Cell* 17(3): p. e12757.

Huang, S.-M., Mouri, A., Kokubo, H., Nakajima, R., Suemoto, T., Higuchi, M., Staufenbiel, M., Noda, Y., Yamaguchi, H., Nabeshima, T., Saido, T.C., Iwata, N. (2006): Neprilysin-sensitive synapse-associated Amyloid-β peptide oligomers impair neuronal plasticity and cognitive function. *Journal of Biological Chemistry* 281(26): 17941–17951.

Hussain, S., Mansouri, S., Sjöholm, Å., Patrone, C., Darsalia, V. (2014): Evidence for cortical neuronal loss in male type 2 diabetic Goto-Kakizaki rats. *Journal of Alzheimer's Disease* 41(2): 551–560.

Hyman, B.T., Phelps, C.H., Beach, T.G., Bigio, E.H., Cairns, N.J., Carrillo, M.C., Dickson, D.W., Duyckaerts, C., Frosch, M.P., Masliah, E., Mirra, S.S., Nelson, P.T., Schneider, J.A., Thal, D.R., Thies, B., Trojanowski, J.Q., Vinters, H.V., Montine, T.J. (2012): National Institute on Aging–Alzheimer's Association guidelines for the neuropathologic assessment of Alzheimer's disease. *Alzheimer's & Dementia* 8(1): 1–13.

Jack, C.R., Shiung, M.M., Gunter, J.L., O'Brien, P.C., Weigand, S.D., Knopman, D.S., Boeve, B.F., Ivnik, R.J., Smith, G.E., Cha, R.H., Tangalos, E.G., Petersen, R.C. (2004): Comparison of different MRI brain atrophy rate measures with clinical disease progression in AD. *Neurology* 62(4): 591–600.

Jankowsky, J.L., Zheng, H. (2017): Practical considerations for choosing a mouse model of Alzheimer's disease. *Molecular Neurodegeneration* 12(1): 89.

Jay, M., De Faveri, F. and McDearmid, J.R. (2015): Firing dynamics and modulatory actions of supraspinal dopaminergic neurons during zebrafish locomotor behavior. *Current Biology* 25(4): 435–444.

Jia, Q., Deng, Y., Qing, H. (2014): Potential therapeutic strategies for Alzheimer's disease targeting or beyond *β*-Amyloid: Insights from clinical trials. *BioMed Research International* 2014: 1–22.

Jinek, M., Chylinski, K., Fonfara, I., Hauer, M., Doudna, J.A., Charpentier, E. (2012): A programmable dual-RNA–guided DNA endonuclease in adaptive bacterial immunity. *Science*, 337(6096): 816–821.

Jurga, A.M., Paleczna, M., Kadluczka, J., Kuter, K.Z. (2021): Beyond the GFAP-astrocyte protein markers in the brain. *Biomolecules* 11(9): 1361.

Kim, Y., Nam, H.G., Valenzano, D.R. (2016): The short-lived African turquoise killifish: an emerging experimental model for ageing. *Disease Models & Mechanisms* 9(2): 115–129.

LaFerla, F.M., Green, K.N., Oddo, S. (2007): Intracellular amyloid-β in Alzheimer's disease. *Nature Reviews Neuroscience* 8(7): 499–509.

Ledo, J.H., Liebmann, T., Zhang, R., Chang, J.C., Azevedo, E.P., Wong, E., Silva, H.M., Troyanskaya, O.G., Bustos, V., Greengard, P. (2021): Presenilin 1 phosphorylation regulates amyloid-β degradation by microglia. *Molecular Psychiatry* 26(10): 5620–5635.

Lee, E.B., Zhang, B., Liu, K., Greenbaum, E.A., Doms, R.W., Trojanowski, J.Q., Lee, V.M.-Y. (2005): BACE overexpression alters the subcellular processing of APP and inhibits Aβ deposition in vivo. *Journal of Cell Biology* 168(2): 291–302.

Leng, K., Li, E., Eser, R., Piergies, A., Sit, R., Tan, M., Neff, N., Li, S.H., Rodriguez, R.D., Suemoto, C.K., Leite, R.E.P., Ehrenberg, A.J., Pasqualucci, C.A., Seeley, W.W., Spina, S., Heinsen, H., Grinberg, L.T., Kampmann, M. (2021): Molecular characterization of selectively vulnerable neurons in Alzheimer's disease. *Nature Neuroscience* 24(2): 276–287.

Liu, C.-C., Kanekiyo, T., Xu, H., Bu, G. (2013): Apolipoprotein E and Alzheimer disease: risk, mechanisms and therapy. *Nature Reviews Neurology* 9(2): 106–118.

López-Otín, C., Blasco, M.A., Partridge, L., Serrano, M., Kroemer, G. (2013): The hallmarks of aging. *Cell* 153(6): 1194–1217.

Loy, C.T., Schofield, P.R., Turner, A.M., Kwok, J.B. (2014): Genetics of dementia. *The Lancet*, 383(9919): 828–840.

Maldonado, T.A., Jones, R.E., Norris, D.O. (2002): Timing of neurodegeneration and beta-amyloid (Aβ) peptide deposition in the brain of aging kokanee salmon. *Journal of Neurobiology* 53(1): 21–35.

Marino, S., Bonanno, L., Lo Buono, V., Ciurleo, R., Corallo, F., Morabito, R., Chirico, G., Marra, A. and Bramanti, P. (2019): Longitudinal analysis of brain atrophy in Alzheimer's disease and frontotemporal dementia. *Journal of International Medical Research* 47(10): 5019–5027.

Matias, I., Morgado, J., Gomes, F.C.A. (2019): Astrocyte heterogeneity: impact to brain aging and disease. *Frontiers in Aging Neuroscience* 11: 59.

Matsui, H., Gavinio, R., Takahashi, R. (2012): Medaka fish Parkinson's disease model. *Experimental Neurobiology* 21(3): 94–100.

Matsui, H., Kenmochi, N., Namikawa, K. (2019): Age- and α-synuclein-dependent degeneration of dopamine and noradrenaline neurons in the annual killifish *Nothobranchius furzeri*. *Cell Reports*, 26(7): 1727-1733.e6.

Matsui, H., Uemura, N., Yamakado, H., Takeda, S., Takahashi, R. (2014): Exploring the pathogenetic mechanisms underlying Parkinson's disease in medaka fish. *Journal of Parkinson's Disease* 4(2): 301–310.

Milanese, C., Sager, J.J., Bai, Q., Farrell, T.C., Cannon, J.R., Greenamyre, J.T., Burton, E.A. (2012): Hypokinesia and reduced dopamine levels in zebrafish lacking β- and γ1-Synucleins. *Journal of Biological Chemistry* 287(5): 2971–2983.

Mirra, S.S., Heyman, A., McKeel, D., Sumi, S.M., Crain, B.J., Brownlee, L.M., Vogel, F.S., Hughes, J.P., Belle, G. v., Berg, L., and participating CERAD neuropathologists (1991): The Consortium to Establish a Registry for Alzheimer's Disease (CERAD): Part II. Standardization of the neuropathologic assessment of Alzheimer's disease. *Neurology*, 41(4): 479–479.

Monterey, M.D., Wei, H., Wu, X., Wu, J.Q. (2021): The many daces of astrocytes in Alzheimer's disease. *Frontiers in Neurology* 12: 619626.

Mukhin, V.N., Pavlov, K.I., Klimenko, V.M. (2017): Mechanisms of neuron loss in Alzheimer's disease. *Neuroscience and Behavioral Physiology* 47(5): 508–516.

Munger, E.L., Edler, M.K., Hopkins, W.D., Ely, J.J., Erwin, J.M., Perl, D.P., Mufson, E.J., Hof, P.R., Sherwood, C.C., Raghanti, M.A. (2019): Astrocytic changes with aging and Alzheimer's disease-type pathology in chimpanzees. *Journal of Comparative Neurology* 527(7): 1179–1195.

Nasrabady, S.E., Rizvi, B., Goldman, J.E., Brickman, A.M. (2018): White matter changes in Alzheimer's disease: a focus on myelin and oligodendrocytes. *Acta Neuropathologica Communications* 6(1): 22.

Neuner, S.M., Heuer, S.E., Huentelman, M.J., O'Connell, K.M.S., Kaczorowski, C.C. (2019): Harnessing genetic complexity to enhance translatability of Alzheimer's disease mouse models: A path toward precision medicine. *Neuron* 101(3): 399-411.e5.

Newman, M., Ebrahimie, E., Lardelli, M. (2014): Using the zebrafish model for Alzheimer's disease research. *Frontiers in Genetics* 5.

Nichols, M.R., St-Pierre, M., Wendeln, A., Makoni, N.J., Gouwens, L.K., Garrad, E.C., Sohrabi, M., Neher, J.J., Tremblay, M., Combs, C.K. (2019): Inflammatory mechanisms in neurodegeneration. *Journal of Neurochemistry* 149(5): 562–581.

Nishiyama, Y., Taguchi, H., Hara, M., Planque, S.A., Mitsuda, Y., Paul, S. (2014): Metal-dependent amyloid β-degrading catalytic antibody construct. *Journal of Biotechnology* 180: 17–22.

Nussbaum, R.L., Ellis, C.E. (2003): Alzheimer's disease and Parkinson's disease. *New England Journal of Medicine* 348(14): 1356–1364.

Osborn, L.M., Kamphuis, W., Wadman, W.J., Hol, E.M. (2016): Astrogliosis: An integral player in the pathogenesis of Alzheimer's disease. *Progress in Neurobiology* 144: 121–141.

Pakkenberg, B. (2003): Aging and the human neocortex. *Experimental Gerontology* 38(1–2): 95–99.

Panza, F., Lozupone, M., Seripa, D. and Imbimbo, B.P. (2019): Amyloid-β immunotherapy for Alzheimer disease: Is it now a long shot?: Aβ Immunotherapy Gamble. *Annals of Neurology* 85(3): 303–315.

Pini, L., Pievani, M., Bocchetta, M., Altomare, D., Bosco, P., Cavedo, E., Galluzzi, S., Marizzoni, M., Frisoni, G.B. (2016): Brain atrophy in Alzheimer's disease and aging. *Ageing Research Reviews* 30: 25–48.

Rasmussen, J., Langerman, H. (2019): Alzheimer's disease – why we need early diagnosis. *Degenerative Neurological and Neuromuscular Disease* Volume 9: 123–130.

Reichwald, K., Petzold, A., Koch, P., Downie, B.R., Hartmann, N., Pietsch, S., Baumgart, M., Chalopin, D., Felder, M., Bens, M., Sahm, A., Szafranski, K., Taudien, S., Groth, M., Arisi, I., Weise, A., Bhatt, S.S., Sharma, V., Kraus, J.M., Schmid, F., Priebe, S., Liehr, T., Görlach, M., Than, M.E., Hiller, M., Kestler, H.A., Volff, J.-N., Schartl, M., Cellerino, A., Englert, C., Platzer, M. (2015): Insights into sex chromosome evolution and aging from the genome of a short-lived fish. *Cell* 163(6): 1527–1538.

Rijal Upadhaya, A., Kosterin, I., Kumar, S., von Arnim, C.A.F., Yamaguchi, H., Fändrich, M., Walter, J., Thal, D.R. (2014): Biochemical stages of amyloid-β peptide aggregation and accumulation in the human brain and their association with symptomatic and pathologically preclinical Alzheimer's disease. *Brain* 137(3): 887–903.

Rose, M.R. (2009): Adaptation, aging, and genomic information. *Aging (Albany NY)* 1(5): 444–450.

Saleem, S., Kannan, R.R. (2018): Zebrafish: an emerging real-time model system to study Alzheimer's disease and neurospecific drug discovery. *Cell Death Discovery* 4(1): 45.

Schlenzig, D., Manhart, S., Cinar, Y., Kleinschmidt, M., Hause, G., Willbold, D., Funke, S.A., Schilling, S., Demuth, H.-U. (2009): Pyroglutamate formation influences solubility and amyloidogenicity of amyloid peptides. *Biochemistry* 48(29): 7072–7078.

Schmued, L.C. and Hopkins, K.J. (2000): Fluoro-Jade B: a high affinity fluorescent marker for the localization of neuronal degeneration. *Brain Research* 874(2): 123–130.

Schott, J.M., Price, S.L., Frost, C., Whitwell, J.L., Rossor, M.N., Fox, N.C. (2005): Measuring atrophy in Alzheimer disease: A serial MRI study over 6 and 12 months. *Neurology* 65(1): 119–124.

Shao, C., Roberts, K.N., Markesbery, W.R., Scheff, S.W., Lovell, M.A. (2006): Oxidative stress in head trauma in aging. *Free Radical Biology and Medicine* 41(1): 77–85.

Shi, Y.-B., Tu, T., Jiang, J., Zhang, Q.-L., Ai, J.-Q., Pan, A., Manavis, J., Tu, E., Yan, X.-X. (2020): Early dendritic dystrophy in human brains with primary age-related tauopathy. *Frontiers in Aging Neuroscience* 12: 596894.

Simić, G., Kostović, I., Winblad, B. and Bogdanović, N. (1997): Volume and number of neurons of the human hippocampal formation in normal aging and Alzheimer's disease. *The Journal of Comparative Neurology* 379(4): 482–494.

Sluimer, J.D., Vrenken, H., Blankenstein, M.A., Fox, N.C., Scheltens, P., Barkhof, F., van der Flier, W.M. (2008): Whole-brain atrophy rate in Alzheimer disease: Identifying fast progressors. *Neurology*, 70(19:2): 1836–1841.

Smith, P., Willemsen, D., Popkes, M., Metge, F., Gandiwa, E., Reichard, M., Valenzano, D.R. (2017): Regulation of life span by the gut microbiota in the short-lived African turquoise killifish. *eLife*, 6: e27014.

Sun, X., Chen, W.-D., Wang, Y.-D. (2015): β-Amyloid: the key peptide in the pathogenesis of Alzheimer's disease. *Frontiers in Pharmacology* 6.

Sweeney, M.D., Sagare, A.P., Zlokovic, B.V. (2018): Blood–brain barrier breakdown in Alzheimer disease and other neurodegenerative disorders. *Nature Reviews Neurology* 14(3): 133–150.

Takahashi, R.H., Capetillo-Zarate, E., Lin, M.T., Milner, T.A., Gouras, G.K. (2010): Co-occurrence of Alzheimer's disease β-amyloid and tau pathologies at synapses. *Neurobiology of Aging* 31(7): 1145–1152.

Takahashi, R.H., Milner, T.A., Li, F., Nam, E.E., Edgar, M.A., Yamaguchi, H., Beal, M.F., Xu, H., Greengard, P., Gouras, G.K. (2002): Intraneuronal Alzheimer Aβ42 accumulates in multivesicular bodies and is associated with synaptic pathology. *The American Journal of Pathology* 161(5): 1869–1879.

Tanzi, R.E., Moir, R.D., Wagner, S.L. (2004): Clearance of Alzheimer's Aβ peptide. *Neuron* 43(5): 605–608.

Terzibasi, E., Lefrançois, C., Domenici, P., Hartmann, N., Graf, M., Cellerino, A. (2009): Effects of dietary restriction on mortality and age-related phenotypes in the short-lived fish *Nothobranchius furzeri*. *Aging Cell* 8(2): 88–99.

Terzibasi, E., Valenzano, D.R., Benedetti, M., Roncaglia, P., Cattaneo, A., Domenici, L., Cellerino, A. (2008): Large differences in aging phenotype between strains of the short-lived annual fish *Nothobranchius furzeri*. *PLoS ONE* 3(12): e3866.

Terzibasi, E., Valenzano, D.R., Cellerino, A. (2007): The short-lived fish *Nothobranchius furzeri* as a new model system for aging studies. *Experimental Gerontology* 42(1–2): 81–89.

Thal, D.R., Rüb, U., Orantes, M., Braak, H. (2002): Phases of Aβ-deposition in the human brain and its relevance for the development of AD. *Neurology* 58(12): 1791–1800.

Thal, D.R., Rüb, U., Schultz, C., Sassin, I., Ghebremedhin, E., Del Tredici, K., Braak, E., Braak, H. (2000): Sequence of Aβ-protein deposition in the human medial temporal lobe. *Journal of Neuropathology & Experimental Neurology* 59(8): 733–748.

Thal, D.R., Walter, J., Saido, T.C., Fändrich, M. (2015): Neuropathology and biochemistry of Aβ and its aggregates in Alzheimer's disease. *Acta Neuropathologica* 129(2): 167–182.

Tozzini, E.T., Baumgart, M., Battistoni, G., Cellerino, A. (2012): Adult neurogenesis in the short-lived teleost *Nothobranchius furzeri*: localization of neurogenic niches, molecular characterization and effects of aging. *Aging Cell* 11(2): 241–251.

Tucker, H.M., Kihiko-Ehmann, M., Wright, S., Rydel, R.E., Estus, S. (2002): Tissue plasminogen activator requires plasminogen to modulate Amyloid-β neurotoxicity and deposition. *Journal of Neurochemistry* 75(5): 2172–2177.

Ullmann, J.F.P., Cowin, G., Collin, S.P. (2010): Quantitative assessment of brain volumes in fish: Comparison of methodologies. *Brain, Behavior and Evolution* 76(3–4): 261–270.

Valdesalici, S., Cellerino, A. (2003): Extremely short lifespan in the annual fish *Nothobranchius furzeri*. *Proceedings of the Royal Society of London. Series B: Biological Sciences* 270(suppl_2).

Valenzano, D.R., Benayoun, B.A., Singh, P.P., Zhang, E., Etter, P.D., Hu, C.-K., Clément-Ziza, M., Willemsen, D., Cui, R., Harel, I., Machado, B.E., Yee, M.-C., Sharp, S.C., Bustamante, C.D., Beyer, A., Johnson, E.A., Brunet, A. (2015): The African turquoise killifish genome provides insights into evolution and genetic architecture of lifespan. *Cell* 163(6): 1539–1554.

Valenzano, D.R., Kirschner, J., Kamber, R.A., Zhang, E., Weber, D., Cellerino, A., Englert, C., Platzer, M., Reichwald, K., Brunet, A. (2009): Mapping loci associated with tail color and sex determination in the short-lived fish *Nothobranchius furzeri*. *Genetics* 183(4): 1385–1395.

Valenzano, D.R., Sharp, S. and Brunet, A. (2011): Transposon-mediated transgenesis in the short-lived African killifish *Nothobranchius furzeri* , a vertebrate model for aging.*G3 Genes|Genomes|Genetics* 1(7): 531–538.

Valenzano, D.R., Terzibasi, E., Cattaneo, A., Domenici, L., Cellerino, A. (2006): Temperature affects longevity and age-related locomotor and cognitive decay in the short-lived fish *Nothobranchius furzeri*. *Aging Cell* 5(3): 275–278.

Valenzano, D.R., Terzibasi, E., Genade, T., Cattaneo, A., Domenici, L., Cellerino, A. (2006): Resveratrol prolongs lifespan and retards the onset of age-related markers in a short-lived vertebrate. *Current Biology* 16(3): 296–300.

Van Houcke, J., Mariën, V., Zandecki, C., Vanhunsel, S., Moons, L., Ayana, R., Seuntjens, E., Arckens, L. (2021): Aging impairs the essential contributions of non-glial progenitors to neurorepair in the dorsal telencephalon of the killifish *Nothobranchius furzeri*. *Aging Cell* 20(9).

Van Nostrand, W.E., Porter, M. (1999): Plasmin cleavage of the Amyloid β-protein: Alteration of secondary structure and stimulation of tissue plasminogen activator activity. *Biochemistry* 38(35): 11570–11576.

Vanhunsel, S., Bergmans, S., Beckers, A., Etienne, I., Van Houcke, J., Seuntjens, E., Arckens, L., De Groef, L., Moons, L. (2021): The killifish visual system as an in vivo model to study brain aging and rejuvenation. *npj Aging and Mechanisms of Disease* 7(1): 22.

Vereecken, Th.H.L.G., Vogels, O.J.M., Nieuwenhuys, R. (1994): Neuron loss and shrinkage in the amygdala in Alzheimer's disease. *Neurobiology of Aging* 15(1): 45–54.

Wang, C.-M., deVries, S., Camboni, M., Glass, M., Martin, P.T. (2010): Immunization with the SDPM1 peptide lowers amyloid plaque burden and improves cognitive function in the APPswePSEN1(A246E) transgenic mouse model of Alzheimer's disease. *Neurobiology of Disease* 39(3): 409–422.

What new Alzheimer's treatments are on the horizon? (2022) *Mayo Clinic*. https://www.mayoclinic.org/diseases-conditions/alzheimers-disease/in-depth/alzheimers-treatments/art-20047780 (Accessed: 24 July 2022).

Whitwell, J.L., Dickson, D.W., Murray, M.E., Weigand, S.D., Tosakulwong, N., Senjem, M.L., Knopman, D.S., Boeve, B.F., Parisi, J.E., Petersen, R.C., Jack, C.R., Josephs, K.A. (2012): Neuroimaging correlates of pathologically defined subtypes of Alzheimer's disease: a case-control study. *The Lancet Neurology* 11(10): 868–877.

Williams, R.W., Herrup, K. (1988): The Control of Neuron Number. *Annual Review of Neuroscience*, 11(1): 423–453.

Woulfe, J.M. (2007): Abnormalities of the nucleus and nuclear inclusions in neurodegenerative disease: a work in progress. *Neuropathology and Applied Neurobiology* 33(1).

Xiao, X., Liu, H., Liu, X., Zhang, W., Zhang, S., Jiao, B. (2021): APP, PSEN1, and PSEN2 variants in Alzheimer's disease: Systematic re-evaluation according to ACMG guidelines. *Frontiers in Aging Neuroscience* 13: 695808.

Yakupova, E.I., Bobyleva, L.G., Vikhlyantsev, I.M., Bobylev, A.G. (2019): Congo Red and amyloids: history and relationship. *Bioscience Reports* 39(1): BSR20181415.

Yang, Z., Wang, K.K.W. (2015): Glial fibrillary acidic protein: from intermediate filament assembly and gliosis to neurobiomarker. *Trends in Neurosciences* 38(6): 364–374.

Zhang, B., Bailey, W.M., McVicar, A.L., Gensel, J.C. (2016): Age increases reactive oxygen species production in macrophages and potentiates oxidative damage after spinal cord injury. *Neurobiology of Aging* 47: 157–167.

Zhang, G., Wang, Z., Hu, H., Zhao, M., Sun, L. (2021): Microglia in Alzheimer's disease: A target for therapeutic intervention. *Frontiers in Cellular Neuroscience* 15: 749587.

Zhang, Z., Ma, Z., Zou, W., Guo, H., Liu, M., Ma, Y., Zhang, L. (2019): The appropriate marker for astrocytes: Comparing the distribution and expression of three astrocytic markers in different mouse cerebral regions. *BioMed Research International* 2019: 1–15.

7. CURRICULUM VITAE

I was born in 1997 in Zagreb, the capital city of Croatia. Even though I grew up in one of the smaller towns surrounding the capital, I decided to pursue my secondary education in Zagreb, where I attended the II. Gymnasium. In 2016 I enrolled in the undergraduate studies in Molecular biology at the Faculty of Science, University of Zagreb. In the spring of 2019, I did my laboratory skill training at the Division of Animal Physiology of Faculty of Science, where I worked under direct supervision of mag. biol. exp. Dyana Odeh, investigating physiological effects of heavy metals and anaesthetics in rats. During my undergraduate studies, I was a member of organising committee of the Student's Symposium in Biology and Life Sciences (SiSB) and the Career Day of the Faculty of Science. Members of both organising committees were awarded Rector's award for socially beneficial work in the academic and wider community; in 2018 for SiSB and in 2019 for the Career Day. Moreover, during my undergraduate studies I was a student body representative in several student bodies and volunteed at the Night of Biology and Open Day of Department of Chemistry at the Faculty of Science, University of Zagreb. In 2018, I led a research workshop called "Enzymes – What they do and how they work" for participants of the Summer School of Science in Požega, Croatia. In 2018, I started working part-time as a student educator in the Zagreb Zoo, where I have been working since then, with occasional breaks.

In 2019, I finished my undergraduate studies and enrolled in the graduate studies in Molecular biology at the Faculty of Science, University of Zagreb. In the beginning of 2020, I was supposed to do my laboratory skill training on the TurtleBIOME project, but the internship had to be redesigned due to the COVID-19 pandemic and I did literature review instead. Later in 2020, I volunteered in the Rubelj Research Group at the Division of Molecular Biology at the Ruđer Bošković Institute, Zagreb. In March 2021, I started working on my master's thesis in the Valenzano Research Group at the Max Planck Institute for Biology of Ageing in Cologne, Germany. During my internship, I worked on the project which involved whole genome sequencing of the African turquoise killifish genome using *Oxford Nanopore Technologies* under direct supervision of dr.sc. David Willemsen and on the project investigating brain degeneration of the same fish species under direct supervision of dr.sc. Dennis de Bakker.

5. SUPPLEMENTARY MATERIAL

Supplementary Table 1. List of all samples analysed in this study. Fish ID number corresponds to the ID in lab's tissue database.

Fish ID number	Species	Hatching date	Sacrifice date	Age	Sex
#9	*N. furzeri*, ZMZ1001	29/06/2020	30/03/2021	9m	Female
#10	*N. furzeri*, ZMZ1001	29/06/2020	30/03/2021	9m	Female
#11	*N. furzeri*, ZMZ1001	29/06/2020	30/03/2021	9m	Male
#115	*D. rerio*	25/06/2020	27/04/2021	10m	Female
#116	*D. rerio*	25/06/2020	27/04/2021	10m	Male
#117	*D. rerio*	25/06/2020	27/04/2021	10m	Male
#120	*D. rerio*	25/06/2020	27/04/2021	10m	Female
#132	*D. rerio*	16/02/2021	17/05/2021	3m	Female
#133	*D. rerio*	16/02/2021	17/05/2021	3m	Female
#136	*D. rerio*	16/02/2021	17/05/2021	3m	Female
#137	*D. rerio*	16/02/2021	17/05/2021	3m	Male
#138	*D. rerio*	16/02/2021	17/05/2021	3m	Male
#142	*D. rerio*	28/09/2018	17/05/2021	2.5y	Female
#143	*D. rerio*	28/09/2018	17/05/2021	2.5y	Male
#144	*D. rerio*	28/09/2018	17/05/2021	2.5y	Female
#145	*D. rerio*	28/09/2018	17/05/2021	2.5y	Male
#146	*D. rerio*	28/09/2018	17/05/2021	2.5y	Male

#152	*D. rerio*	18/11/2020	19/05/2021	6m	Female
#153	*D. rerio*	18/11/2020	19/05/2021	6m	Male
#154	*D. rerio*	18/11/2020	19/05/2021	6m	Male
#155	*D. rerio*	18/11/2020	19/05/2021	6m	Female
#156	*D. rerio*	18/11/2020	19/05/2021	6m	Female
#157	*D. rerio*	18/11/2020	19/05/2021	6m	Female
#158	*N. furzeri*, ZMZ1001	15/02/2021	20/05/2021	3m	Male
#159	*N. furzeri*, ZMZ1001	15/02/2021	20/05/2021	3m	Male
#160	*N. furzeri*, ZMZ1001	15/02/2021	20/05/2021	3m	Male
#170	*N. furzeri*, ZMZ1001	17/05/2021	28/06/2021	1.5m	Male
#171	*N. furzeri*, ZMZ1001	17/05/2021	28/06/2021	1.5m	Female
#173	*N. furzeri*, ZMZ1001	17/05/2021	28/06/2021	1.5m	Female
#174	*N. furzeri*, ZMZ1001	17/05/2021	28/06/2021	1.5m	Female
#175	*N. furzeri*, ZMZ1001	17/05/2021	28/06/2021	1.5m	Male
#176	*N. furzeri*, ZMZ1001	17/05/2021	28/06/2021	1.5m	Female
#223	*N. furzeri*, ZMZ1001	04/01/2021	04/09/2021	9m	Male
#224	*N. furzeri*, ZMZ1001	04/01/2021	04/09/2021	9m	Female
#225	*N. furzeri*, ZMZ1001	04/01/2021	04/09/2021	9m	Male
#226	*N. furzeri*, ZMZ1001	04/01/2021	04/09/2021	9m	Female
#263	*N. furzeri*, ZMZ1001	17/05/2021	16/11/2021	6m	Female
#264	*N. furzeri*, ZMZ1001	17/05/2021	16/11/2021	6m	Male
#265	*N. furzeri*, ZMZ1001	17/05/2021	16/11/2021	6m	Male

#266	*N. furzeri*, ZMZ1001	17/05/2021	16/11/2021	6m	Female
#267	*N. furzeri*, ZMZ1001	17/05/2021	16/11/2021	6m	Female
#291	*D. rerio*	23/05/2017	10/01/2022	4y8m2w	Male
#292	*D. rerio*	23/05/2017	10/01/2022	4y8m2w	Female
#293	*D. rerio*	23/05/2017	10/01/2022	4y8m2w	Female
#294	*D. rerio*	23/05/2017	10/01/2022	4y8m2w	Female
#295	*D. rerio*	23/05/2017	10/01/2022	4y8m2w	Female
#296	*D. rerio*	23/05/2017	10/01/2022	4y8m2w	Female
#305	*N. furzeri*, ZMZ1001	25/10/2021	31/01/2022	3m	Male
#306	*N. furzeri*, ZMZ1001	25/10/2021	31/01/2022	3m	Male

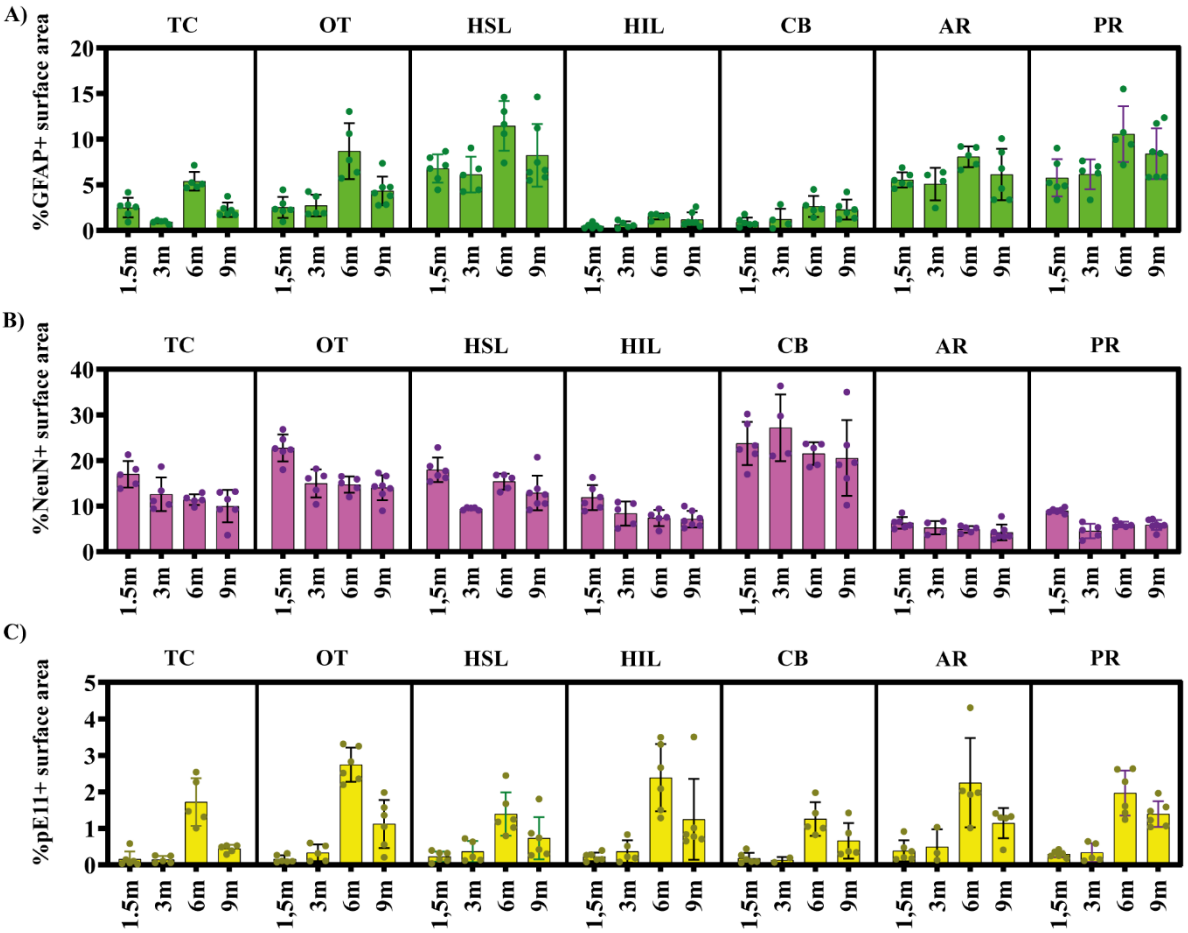

Supplementary Figure 1. Overview of all seven analysed brain regions. Each dot on the graph represents a single brain, displaying the average between values acquired from between 1 and 3 brain sections per brain. Abbreviations stand for telencephalon (TC), optic tectum (OT), hypothalamus superior lobe (HSL), hypothalamus inferior lobe (HIL), cerebellum (CB), anterior rhomboencephalon (AR) and posterior rhomboencephalon (PR). **(A)** Quantification of the percentage of GFAP covered surface area in seven brain regions of turquoise killifish, across four time points. The results display a significant upregulation of GFAP with age in six out of seven brain regions. The ordinary one-way ANOVA test supports the results for the most brain regions, with P values for the TC (<0.0001), the OT (<0.0001), the HSL (0.0175), the HIL (0.0094), the CB (0.0307) and PR (0.0176). The ordinary one-way ANOVA test does not support the significance of the results for the AR, with the P value of 0.0955. **(B)** Quantification of the percentage of NeuN covered surface area in seven brain regions of turquoise killifish, across four time points. The results display a significant downregulation of NeuN with age in five out of seven brain regions. The ordinary one-way ANOVA test supports the results for the most brain regions, with P values for the TC (0.0096), the OT (<0.0001), the HSL (0.0003), the HIL (0.0059) and PR (<0.0001). The ordinary one-way ANOVA test does not support the significance of the results for the CB (0.3952) and the AR (0.0857). **(C)** Quantification of the percentage of $A\beta_{pE11-42}$ covered surface area in seven brain regions of turquoise killifish, across four time points. The results display a significant upregulation of $A\beta_{pE11-42}$ with age in all seven brain regions. The ordinary one-way ANOVA test supports the results for the most brain regions, with P values for the TC (<0.0001), the OT (<0.0001), the HSL (0.0013), the HIL (0.0003), the CB (0.00014), AR (0.0033) and PR (<0.0001).

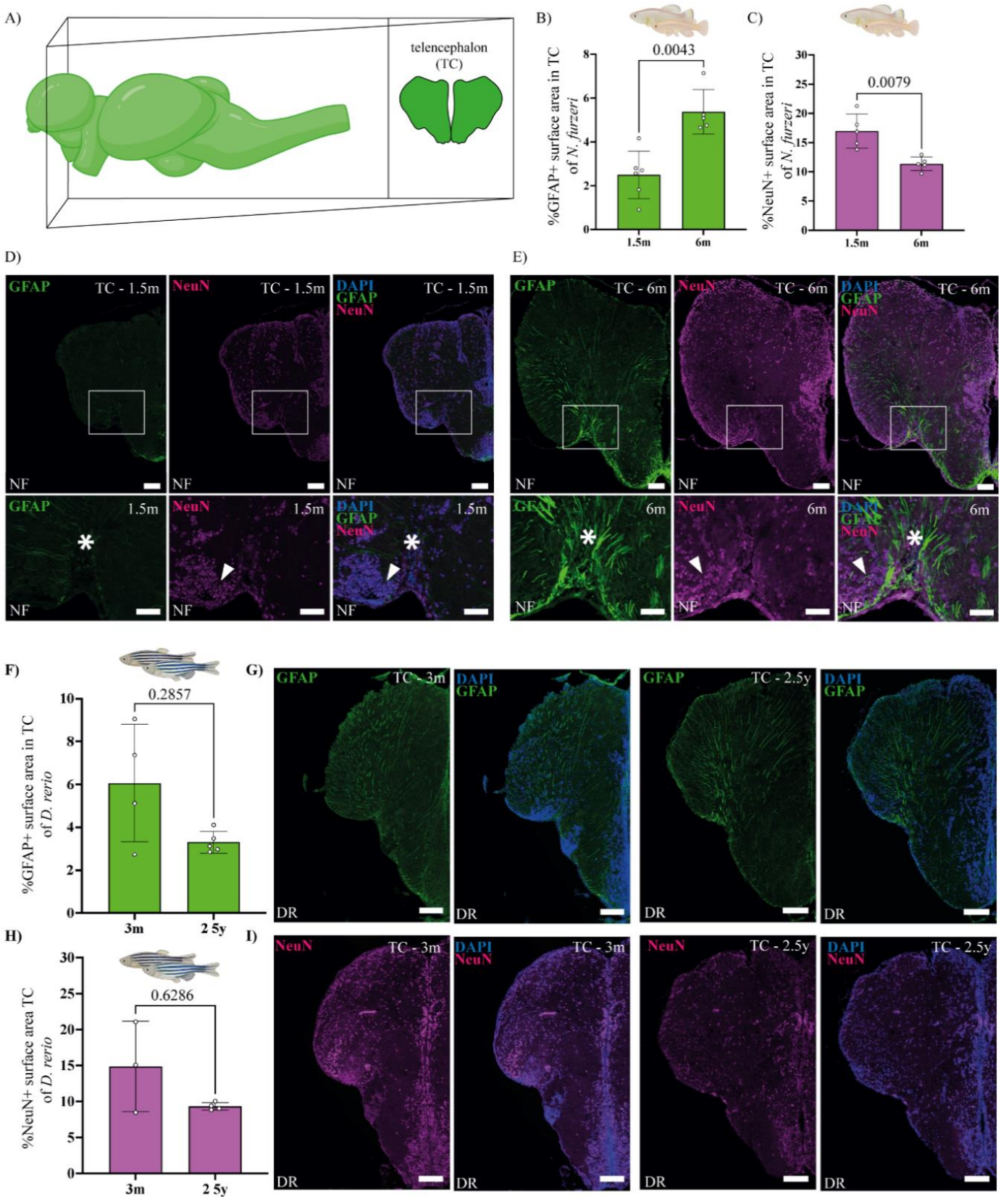
A)
telencephalon
(TC)
B)
0.0043
%GFAP+ surface area in TC
of N. furzeri
1.5m
6m
C)
0.0079
%NeuN+ surface area in TC
of N. furzeri
1.5m
6m
D)
E)
GFAP
NeuN
DAPI
TC - 1.5m
TC - 6m
1.5m
6m
NF
F)
0.2857
%GFAP+ surface area in TC
of D. rerio
3m
2 5y
G)
TC - 3m
TC - 2.5y
DR
H)
0.6286
%NeuN+ surface area TC
of D. rerio
I)

Supplementary Figure 2. Age-dependent astrogliosis and decreased neuronal density in the telencephalon of turquoise killifish but not in the telencephalon of zebrafish A) Schematic representation of the brain region of interest. **(B)** Quantification of the percentage of GFAP covered surface area in the TC of 1.5-month-old and 6-month-old brains of turquoise killifish displaying significant upregulation of GFAP with age. **(C)** Quantification of the percentage of NeuN covered surface area in the TC of 1.5-month-old and 6-month-old brain of turquoise killifish, displaying significant upregulation of NeuN with age. **(D, E)** Representative sections of the TC of 1.5-month-old (D) and 6-month-old (E) turquoise killifish stained for GFAP, NeuN, and DAPI. The white asterisk indicates examples of positive GFAP signal, The white arrowheads indicate examples of positive NeuN signal. The scale bar represents 100μm in the overview (top) and 50μm in the zoom-in (bottom). **(F)** Quantification of the percentage of GFAP covered surface area in the TC of 3-month-old and 2.5-year-old brain of zebrafish, supported by no significance in the difference. **(G)** Representative sections of the 3-month-old (left) and 2.5-year-old (right) TC of zebrafish stained for GFAP and DAPI. **(H)** Quantification of the percentage of NeuN covered surface area in the TC of 3- month-old and 2.5-year-old brain of zebrafish, indicated by no significance in difference between the results. **(I)** Representative sections of the 3-month-old (left) and 2.5-year-old (right) TC of zebrafish stained for NeuN and DAPI. The scale bar represents 100μm in the overview. Each dot on the graph represents a single brain, displaying the average between values acquired from between 1 and 3 brain sections per brain. Mann-Whitney test's P values are indicated above the graphs.

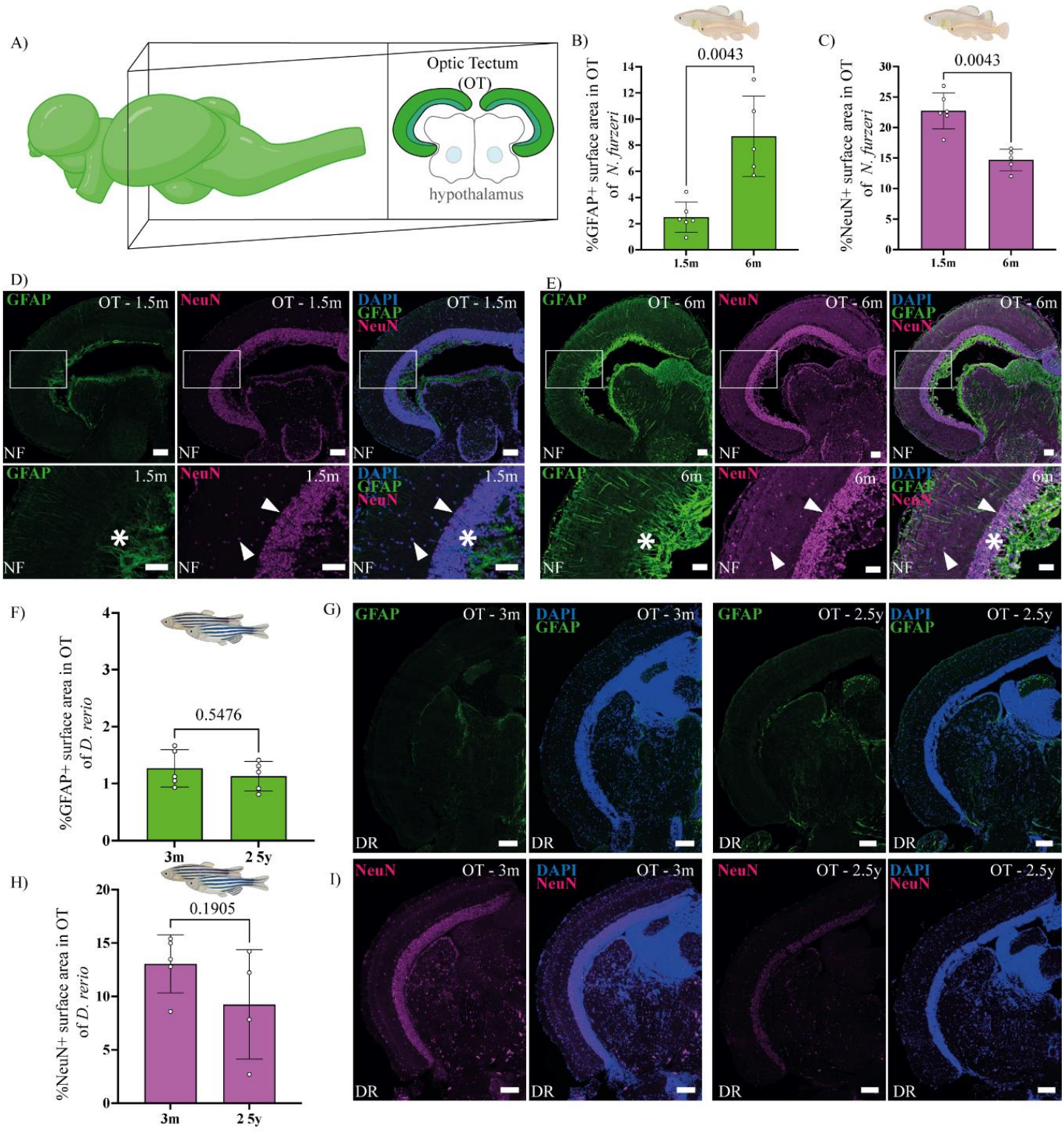
A)
Optic Tectum
(OT)
hypothalamus
B)
0.0043
%GFAP+ surface area in OT of N. furzeri
1.5m
6m
C)
0.0043
%NeuN+ surface area in OT of N. furzeri
1.5m
6m
D)
GFAP OT - 1.5m
NeuN OT - 1.5m
DAPI GFAP NeuN OT - 1.5m
GFAP 1.5m
NeuN 1.5m
DAPI GFAP NeuN 1.5m
NF
E)
GFAP OT - 6m
NeuN OT - 6m
DAPI GFAP NeuN OT - 6m
GFAP 6m
NeuN 6m
DAPI GFAP NeuN 6m
NF
F)
0.5476
%GFAP+ surface area in OT of D. rerio
3m
2 5y
G)
GFAP OT - 3m
DAPI GFAP OT - 3m
GFAP OT - 2.5y
DAPI GFAP OT - 2.5y
DR
H)
0.1905
%NeuN+ surface area in OT of D. rerio
3m
2 5y
I)
NeuN OT - 3m
DAPI NeuN OT - 3m
NeuN OT - 2.5y
DAPI NeuN OT - 2.5y
DR

Supplementary Figure 3. Age dependent astrogliosis and decrease in neuronal densitiy in the optic tectum of turquoise killifish but not in the optic tectum of zebrafish. (A) Schematic representation of the brain region of interest. **(B)** Quantification of the percentage of GFAP covered surface area in the OT of 1.5-month-old and 6-month-old brain in turquoise killifish, with indicated significant upregulation of GFAP with age. **(C)** Quantification of the percentage of NeuN covered surface area in the optic tectum of 1.5-month-old and 6-month-old brain of turquoise killifish, with indicated significant upregulation of NeuN with age. **(D, E)** Representative sections of the 1.5-month-old. (D) and 6-month-old (E) OT of turquoise killifish stained for GFAP, NeuN, and DAPI. The white asterisk indicates examples of positive GFAP signal. The white arrowheads indicate examples of positive NeuN signal. The scale bar represents 100µm in the overview (top) and 50µm in the zoom-in (bottom). **(F)** Quantification of the percentage of GFAP covered surface area in the OT of 3-month-old and 2.5-year-old brain in zebrafish, displaying no significance in the difference between GFAP positive signa. **(G)** Representative sections of the 3-month-old (left) and 2.5-year-old (right) OT of zebrafish stained for GFAP and DAPI. **(H)** Quantification of the percentage of cross-sectional surface area covered with NeuN positive signal in the OT of 3- months old and 2.5-year-old brain of zebrafish, displaying no significant difference in the result. **(I)** Representative sections of the 3-month-old (left) and 2.5-year-old (right) OT of zebrafish stained for NeuN and DAPI. The scale bar represents 100µm in the overview. Each dot on the graph represents a single brain, displaying the average between values acquired from between 1 and 3 brain sections per brain. Mann-Whitney test's P values are indicated above the graphs.

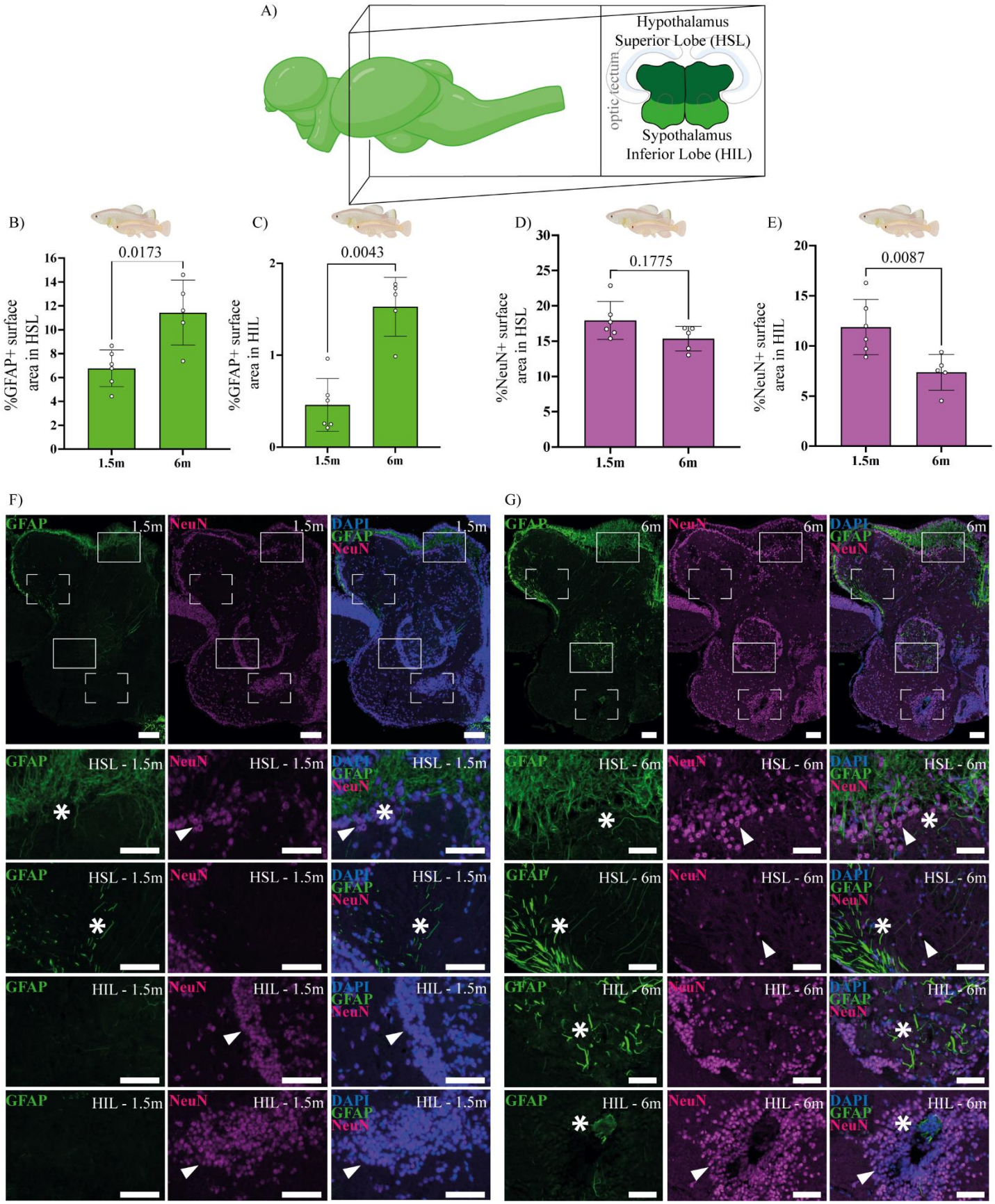
A)
Hypothalamus
Superior Lobe (HSL)
optic tectum
Sypothalamus
Inferior Lobe (HIL)
B)
%GFAP+ surface area in HSL
0.0173
1.5m
6m
C)
%GFAP+ surface area in HIL
0.0043
1.5m
6m
D)
%NeuN+ surface area in HSL
0.1775
1.5m
6m
E)
%NeuN+ surface area in HIL
0.0087
1.5m
6m
F)
G)
GFAP
NeuN
DAPI
HSL - 1.5m
HIL - 1.5m
HSL - 6m
HIL - 6m

Supplementary Figure 4. Age dependent astrogliosis and decreased neuronal density in the hypothalamus of turquoise killifish. (A) Schematic representation of the brain region of interest, divided into Hypothalamus Superior Lobe (HSL) i Hypothalamus Inferior Lobe (HIL. **(B)** Quantification of the percentage of GFAP covered surface area in the HSL and the HIL of 1.5-month-old and 6-month-old brain of turquoise killifish, displaying a significant upregulation of AβpE11-42 with age. Each dot represents a single brain, displaying the average between values acquired from either 2 or 3 brain sections per brain. **(C)** Quantification of the percentage of NeuN covered surface area in the HSL and the HIL of 1.5-month-old and 6-month-old brain of turquoise killifish, displaying no significant upregulation of NeuN with age for the HSL and a significant upregulation of NeuN with age for the HIL. **(D, E)** Representative sections of the 1.5-month-old. (D) and 6-month-old (E) hypothalamus stained for GFAP, NeuN, and DAPI. The white asterisk indicates examples of positive GFAP signal. The white arrowheads indicate examples of positive NeuN signal. The scale bar represents 100μm in the overview (top) and 50μm in the zoom-in (bottom). Mann-Whitney test's P values are indicated above the graphs.

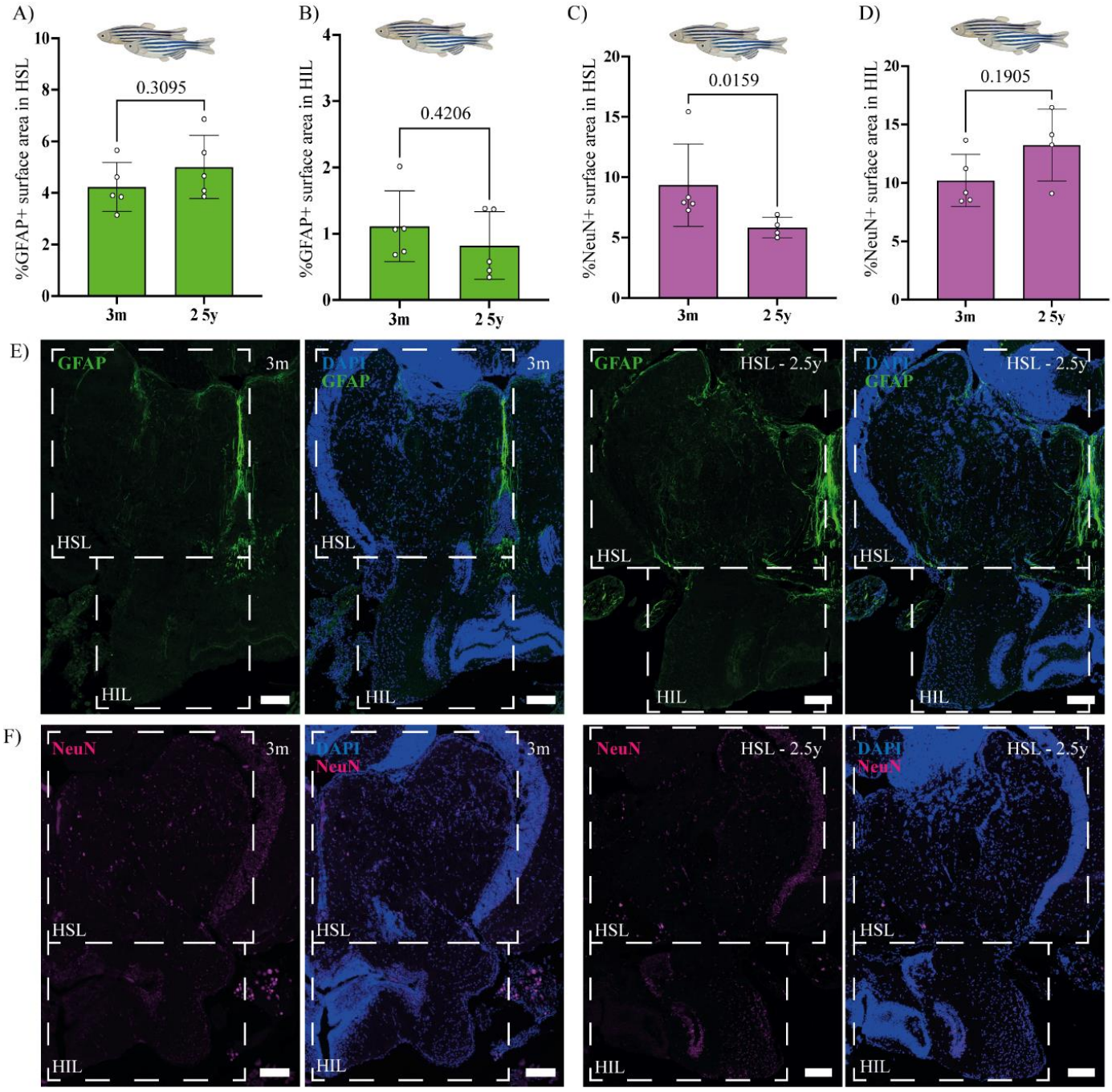

Supplementary Figure 5. No significant change in astrogliosis and partially also in neuronal density in the hypothalamus of zebrafish. (A) Quantification of the percentage of GFAP covered surface area in the Hypothalamus Superior Lobe (HSL) of 3-month-old and 2.5-year-old brain of zebrafish, displaying no significance in the results. **(B)** Quantification of the percentage of GFAP covered surface area in the Hypothalamus Inferior Lobe (HIL) of 3-month-old and 2.5-year-old brain of zebrafish, displaying no significance in the results. **(C)** Quantification of the percentage of NeuN covered surface area in the HSL of 3-month-old and 2.5-year-old brain of zebrafish, supported by the significance in the difference between two time points. **(D)** Quantification of the percentage of NeuN covered surface area in the HIL of 3-month-old and 2.5-year-old brain of zebrafish, displaying no significance in the results. **(E)** Representative sections of the 3-month-old (left) and 2.5-year-old (right) HSL and HIL of zebrafish stained for GFAP and DAPI. **(F)** Representative sections of the 3-month-old (left) and 2.5-year-old (right) HSL and HIL of zebrafish stained for NeuN and DAPI. The scale bar represents 100µm in the overview. Each dot in a graph represents a single brain, displaying the average between values

acquired from between 1 and 3 brain sections per brain. Mann-Whitney test's P values are indicated above the graphs.

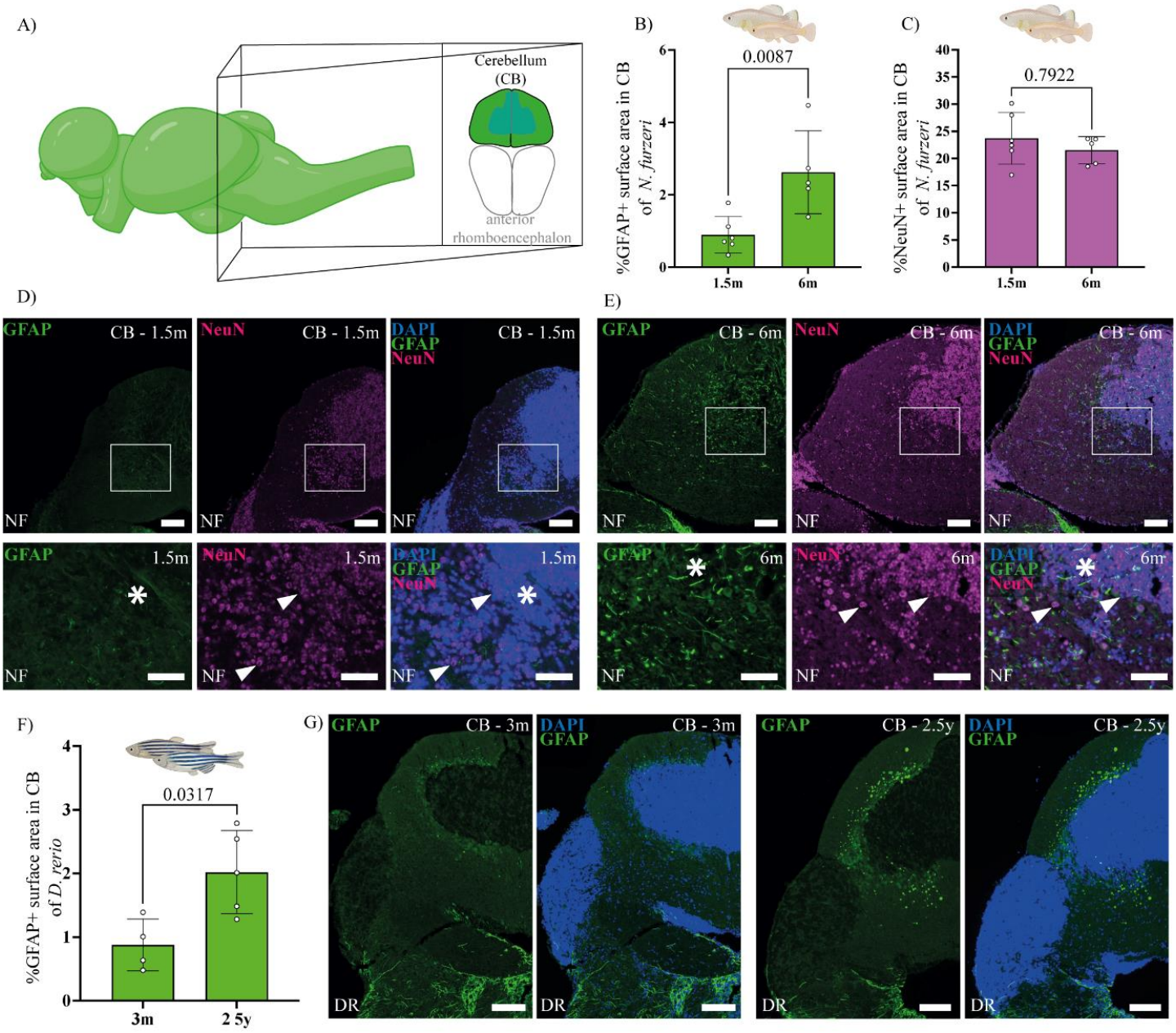

Supplementary Figure 6. Age dependent astrogliosis in the cerebellum of turquoise killifish and zebrafish, accompanied by no change in neuronal density in turquoise killifish A) Schematic representation of the brain region of interest. **(B)** Quantification of the percentage of GFAP covered surface area in the CB of 1.5-month-old and 6-month-old brain of turquoise killifish, displaying a significant upregulation of GFAP with age. **(C)** Quantification of the percentage of NeuN covered surface area in the CB of 1.5-month-old and 6-month-old brain of turquoise killifish, accompanied by no significant upregulation of NeuN with age. **(D, E)** Representative sections of 1.5-month-old. (D) and 6-month-old (E) CB of turquoise killifish stained for GFAP, NeuN, and DAPI. The white asterisk indicate examples of positive GFAP signal. The white arrowheads indicate examples of positive

NeuN signal. The scale bar represents 100µm in the overview (top) and 50µm in the zoom-in (bottom). **(F)** Quantification of the percentage of GFAP covered surface area in the CB of 3-month-old and 2.5-year-old brain of zebrafish, with no significance in the results. **(G)** Representative sections of the 3-month-old (left) and 2.5-year-old (right) CB of zebrafish stained for GFAP and DAPI. The scale bar represents 100µm. Each dot on the graph represents a single brain, displaying the average between values acquired from between 1 and 3 brain sections per brain. Mann-Whitney test's P values are indicated above the graphs.

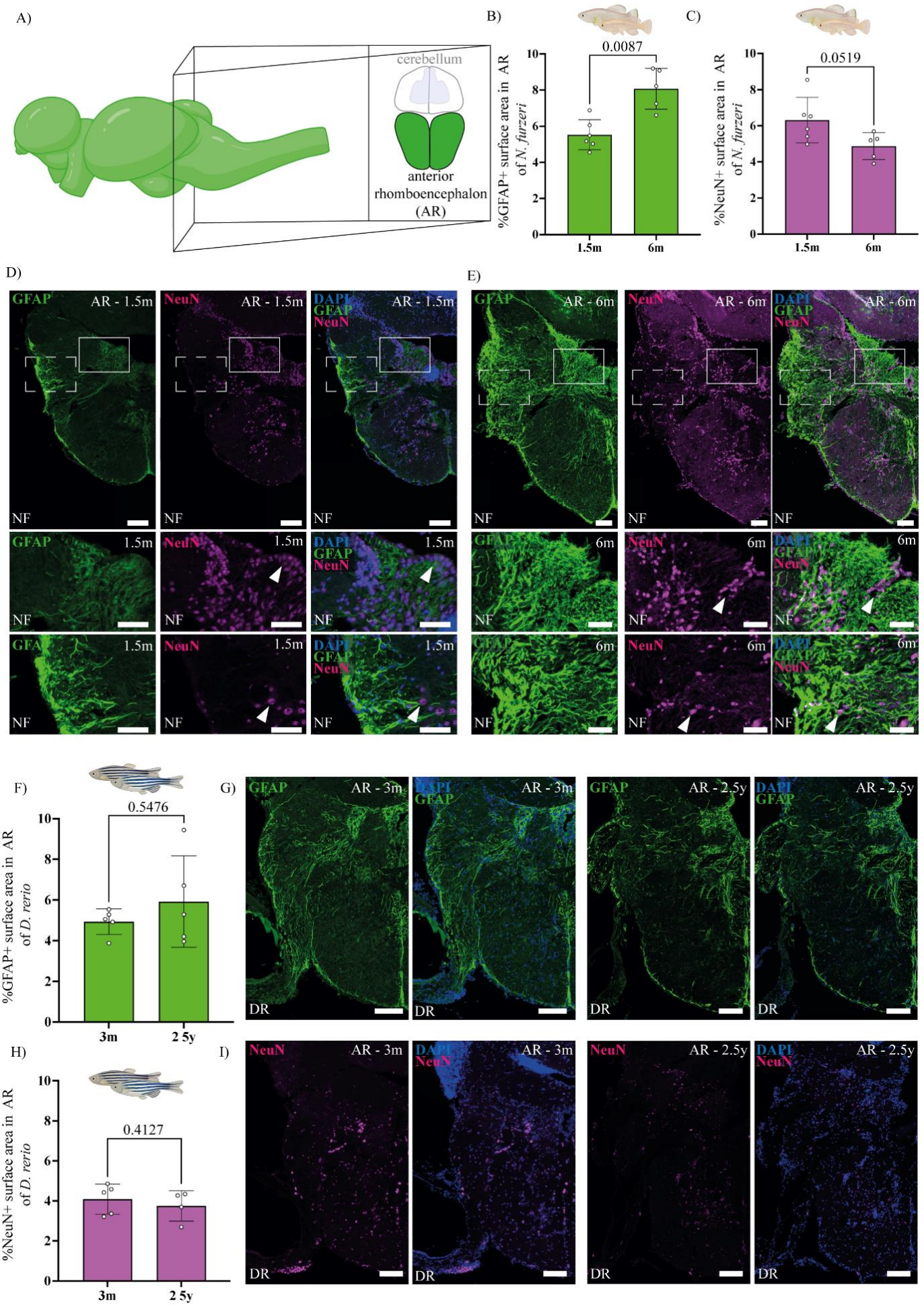
A)
cerebellum
anterior
rhomboencephalon
(AR)
B)
0.0087
%GFAP+ surface area in AR
of N. furzeri
1.5m
6m
C)
0.0519
%NeuN+ surface area in AR
of N. furzeri
1.5m
6m
D)
E)
GFAP
NeuN
DAPI
AR - 1.5m
AR - 6m
1.5m
6m
NF
F)
0.5476
%GFAP+ surface area in AR
of D. rerio
3m
2 5y
G)
AR - 3m
AR - 2.5y
DR
H)
0.4127
%NeuN+ surface area in AR
of D. rerio
3m
2 5y
I)

Supplementary Figure 7. Age dependent astrogliosis in the anterior rhomboencephalon of turquoise killifish but no decrease in neuronal density, followed by no astrogliosis nor decrease in neuronal density in the anterior rhomboencephalon of zebrafish. (A) Schematic representation of the brain region of interest. **(B)** Quantification of the percentage of GFAP covered surface area in AR of 1.5-month-old and 6-months-old brain of turquoise killifish, displaying a significant upregulation of GFAP with age. **(C)** Quantification of the percentage of NeuN covered surface area in the AR of 1.5-month-old and 6-month-old brain of turquoise killifish, displaying no significant downregulation of NeuN with age. **(D, E)** Representative sections of the 1.5-month-old. (D) and 6-month-old (E) AR of turquoise killifish stained for GFAP, NeuN, and DAPI. The white arrowheads indicate examples of positive NeuN signal. The scale bar represents 100µm in the overview (top) and 50µm in the zoom-in (bottom). **(F)** Quantification of the percentage of GFAP covered surface area in the AR of 3-month-old and 2.5-year-old brain of zebrafish, displaying no significant difference between the results. **(G)** Representative sections of the 3-month-old (left) and 2.5-year-old (right) AR of zebrafish stained for GFAP and DAPI. **(H)** Quantification of the percentage of NeuN covered surface area in the AR of 3-month-old and 2.5-year-old brain of zebrafish with no significant difference between the results. **(I)** Representative sections of the 3-month-old (left) and 2.5-year-old (right) AR of zebrafish stained for NeuN and DAPI. The scale bar represents 100µm in the overview. Each dot on the graph represents a single brain, displaying the average between values acquired from between 1 and 3 brain sections per brain. Mann-Whitney test's P values are indicated above the graphs.

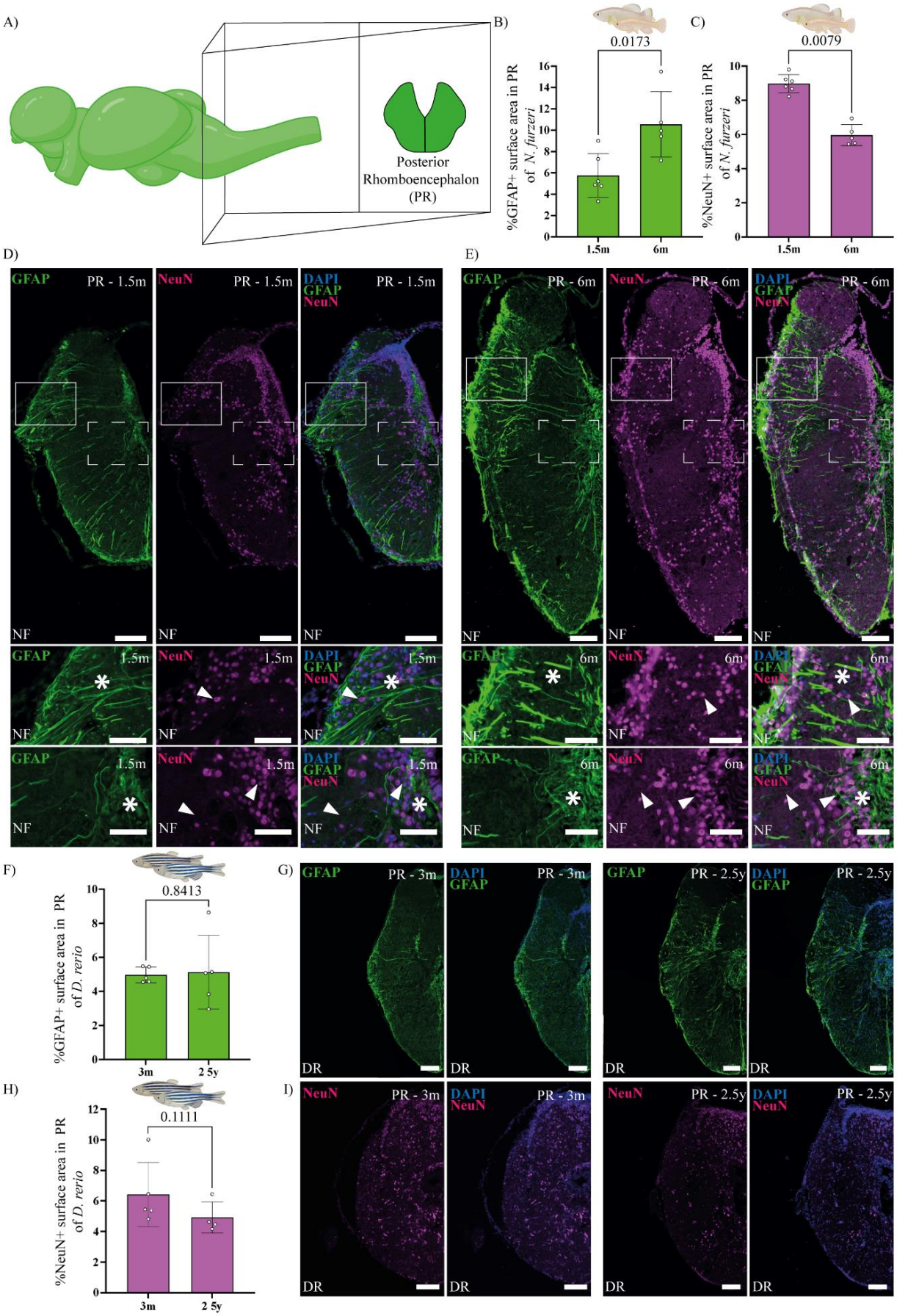
A)
Posterior
Rhomboencephalon
(PR)
B)
0.0173
%GFAP+ surface area in PR
of N. furzeri
1.5m
6m
C)
0.0079
%NeuN+ surface area in PR
of N. furzeri
1.5m
6m
D)
E)
GFAP
NeuN
DAPI
PR - 1.5m
PR - 6m
NF
1.5m
6m
F)
0.8413
%GFAP+ surface area in PR
of D. rerio
3m
2 5y
G)
PR - 3m
PR - 2.5y
DR
H)
0.1111
%NeuN+ surface area in PR
of D. rerio
3m
2 5y
I)
PR - 3m
PR - 2.5y
DR

Supplementary Figure 8. Age dependent astrogliosis and decrease in neuronal density in the posterior rhomboencephalon of turquoise killifish but not D. rerio. (A) Schematic representation of the brain region of interest. **(B)** Quantification of the percentage of GFAP covered surface area in the PR of 1.5-month-old and 6-month-old brain of turquoise killifish, showing significant upregulation of GFAP with age. **(C)** Quantification of the percentage of NeuN covered surface area in the PRof 1.5-month- old and 6-month-old brain of turquoise killifish, showing a significant upregulation of NeuN with age. **(D, E)** Representative sections of the 1.5-month-old (D) and 6-month-old (E) PR of turquoise killifish stained for GFAP, NeuN, and DAPI. The white asterisk indicates examples of positive GFAP signal. The white arrowheads indicate examples of positive NeuN signal. The scale bar represents 100μm in the overview (top) and 50μm in the zoom-in (bottom). **(F)** Quantification of the percentage of GFAP covered surface area in the PR of 3-month-old and 2.5-year-old brain of zebrafish, displaying no significance in the difference of the results. **(G)** Representative sections of the 3-month-old (left) and 2.5-year-old (right) PR of zebrafish stained for GFAP and DAPI. **(H)** Quantification of the percentage of NeuN covered surface area in the PR of 3-month-old and 2.5-year-old brain of zebrafish, displaying no significance in the difference of the results. **(I)** Representative sections of the 3-month-old (left) and 2.5-year-old (right) PR of zebrafish stained for NeuN and DAPI. The scale bar represents 100μm in the overview. Each dot on the graph represents a single brain, displaying the average between values acquired from between 1 and 3 brain sections per brain. Mann-Whitney test's P values are indicated above the graphs.

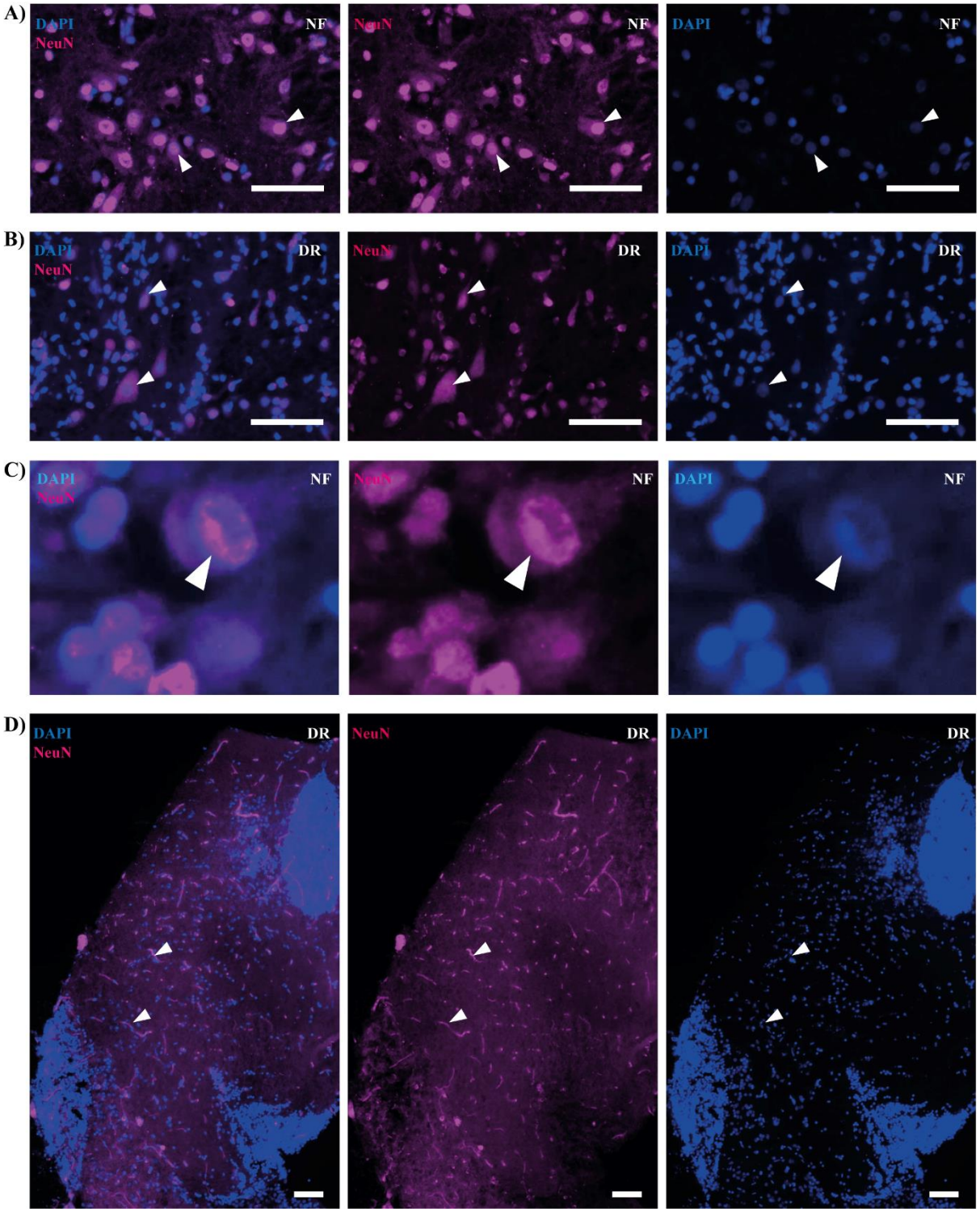

Supplementary Figure 9. Overview of variation in NeuN signal across different conditions. (A) Neuronal cells detected in the brain of turquoise killifish. **(B)** Neuronal cells detected in the brain of zebrafish. Zoom-ins show signal indicating neuronal nuclei (magenta) only partially overlapping with signal showing all nuclei (blue), in both turquoise killifish and zebrafish. Arrows are pointing at neuronal cells that do not completely overlap with DAPI. **(C)** Potentially damaged neuronal cells in the brain of turquoise killifish indicated by arrows, stained for NeuN and DAPI. **(D)** The cerebellum of zebrafish brain hemisphere stained with NeuN. Arrows are pointing at stained blood vessels. Left image in each panel represents overlapping image of neuronal NeuN signal (magenta) and nuclear DAPI signal (blue). An image in the middle of each panel shows only NeuN signal in the tissue, while

right image shows only DAPI signal present in the tissue. The white arrowheads indicate examples of NeuN positive signal that does not overlap with DAPI. The scale bar represents 50μm.